Using in situ Chlorine-36 cosmonuclide to recover past earthquake histories on limestone normal fault scarps: a reappraisal of methodology and interpretations

Aloé Schlagenhauf, Yves Gaudemer, Lucilla Benedetti, Isabelle Manighetti, Luigi Palumbo, Irene Schimmelpfennig, Robert C. Finkel, Khemrak Pou

▶ **To cite this version:**

Aloé Schlagenhauf, Yves Gaudemer, Lucilla Benedetti, Isabelle Manighetti, Luigi Palumbo, et al.. Using in situ Chlorine-36 cosmonuclide to recover past earthquake histories on limestone normal fault scarps: a reappraisal of methodology and interpretations. Geophysical Journal International, 2010, 182 (1), pp.36-72. ⟨10.1111/J.1365-246X.2010.04622.X⟩. ⟨insu-00565033⟩

HAL Id: insu-00565033

https://insu.hal.science/insu-00565033v1

Submitted on 1 Feb 2019

HAL is a multi-disciplinary open access archive for the deposit and dissemination of scientific research documents, whether they are published or not. The documents may come from teaching and research institutions in France or abroad, or from public or private research centers.

L'archive ouverte pluridisciplinaire **HAL**, est destinée au dépôt et à la diffusion de documents scientifiques de niveau recherche, publiés ou non, émanant des établissements d'enseignement et de recherche français ou étrangers, des laboratoires publics ou privés.

HAL Authorization

Geophysical Journal International

Geophys. J. Int. (2010) **182,** 36–72 doi: 10.1111/j.1365-246X.2010.04622.x

Using *in situ* Chlorine-36 cosmonuclide to recover past earthquake histories on limestone normal fault scarps: a reappraisal of methodology and interpretations

Aloé Schlagenhauf,[1,*] Yves Gaudemer,[2] Lucilla Benedetti,[3] Isabelle Manighetti,[1] Luigi Palumbo,[4] Irene Schimmelpfennig,[3] Robert Finkel[3] and Khemrak Pou[3]

[1] *Laboratoire de Géophysique Interne et Tectonophysique (LGIT), CNRS, Observatoire de Grenoble (OSUG), Université J. Fourier, Maison des Géosciences,* BP 53, 38041 *Grenoble cédex* 09, *France. E-mail: Aloe.Schlagenhauf@obs.ujf-grenoble.fr*

[2] *Institut de Physique du Globe de Paris (IPGP), CNRS, 4 place Jussieu, case* 89, 75252 *Paris, France*

[3] *Centre Européen de Recherche et d'Enseignement des Géosciences de l'Environnement (CEREGE), CNRS, Europole Mediterranéen de l'Arbois,* BP 80, 13545 *Aix-en-Provence cédex 04, France*

[4] *Geologisch-Paläontologisches Institut, Westfälische Wilhelms-Universität, Corrensstrasse* 24, D-48149 *Münster, Germany*

Accepted 2010 April 8. Received 2010 March 21; in original form 2009 June 5

SUMMARY

Cosmic-ray exposure dating of preserved, seismically exhumed limestone normal fault scarps has been used to identify the last few major earthquakes on seismogenic faults and recover their ages and displacements through the modelling of the content of *in situ* [^{36}Cl] cosmonuclide of the scarp rocks. However, previous studies neglected some parameters that contribute to ^{36}Cl accumulation and the uncertainties on the inferred earthquake parameters were not discussed. To better constrain earthquake parameters and to explore the limits of this palaeoseismological method, we developed a Matlab® modelling code (provided in Supplementary information) that includes all the factors that may affect [^{36}Cl] observed in seismically exhumed limestone fault scarp rocks. Through a series of synthetic profiles, we examine the effects of each factor on the resulting [^{36}Cl], and quantify the uncertainties related to the variability of those factors. Those most affecting the concentrations are rock composition, site location, shielding resulting from the geometry of the fault scarp and associated colluvium, and scarp denudation. In addition, ^{36}Cl production mechanisms and rates are still being refined, but the importance of these epistemic uncertainties is difficult to assess. We then examine how pre-exposure and exposure histories of fault-zone materials are expressed in [^{36}Cl] profiles. We show that the ^{36}Cl approach allows unambiguous discrimination of sporadic slip versus continuous creep on these faults. It allows identification of the large slip events that have contributed to the scarp exhumation, and provides their displacement with an uncertainty of $\pm$ ~25 cm and their age with an uncertainty of $\pm$0.5–1.0 kyr. By contrast, the modelling cannot discriminate whether a slip event is a single event or is composed of multiple events made of temporally clustered smaller size events. As a result, the number of earthquakes identified is always a minimum, while the estimated displacements are maximum bounds and the ages the approximate times when a large earthquake or a cluster of smaller earthquakes have occurred. We applied our approach to a data set available on the Magnola normal fault, Central Italy, including new samples from the buried part of the scarp. Reprocessing of the data helps to refine the seismic history of the fault and quantify the uncertainties in the number of earthquakes, their ages and displacements. We find that the Magnola fault has ruptured during at least five large earthquakes or earthquake clusters in the last 7 ka, and may presently be in a phase of intense activity.

Key words: Geomorphology; Palaeoseismology; Continental tectonics: extensional; Neotectonics; Europe.

1 INTRODUCTION

The magnitude of past earthquakes, their timing, and the regularity of their recurrence inform seismic hazard assessment.

*Now at: Active Fault and Earthquake Research Center (AFERC), AIST Tsukuba Central 7, 1–1-1 Higashi, Tsukuba, Ibaraki 305–8567 Japan.

© 2010 The Authors
Journal compilation © 2010 RAS

Downloaded from https://academic.oup.com/gji/article-abstract/182/1/36/562733 by guest on 01 February 2019

Figure 1. Northward view of the Magnola normal fault near the Forme village (Central Apennines, Italy). (a) White arrows outline the Holocene fault scarplet, at the base of the cumulative escarpment (black double-arrow) which forms the relief. Below is the colluvial wedge with vegetation. White box locates b. (b) Close-up view of the basal Holocene scarplet, showing the ∼10 m high vertical groove sampled by Palumbo *et al.* (2004). Scale applies to fault scarplet only.

Unfortunately, recurrence times between large earthquakes ($M \geq 6$) are generally longer than instrumental and historical earthquake catalogues, and palaeoseismic methods must be used to infer the timing and magnitude of earthquakes in the geologic record. However, there are only a few techniques that allow such past earthquake recovery. The first consists of digging one or a few 1–4-m-deep trenches across an active fault to identify offsets of the shallow subsurface strata (e.g. Sieh *et al.* 1989, 1992; Weldon *et al.* 2004; Daëron *et al.* 2007; Liu-Zheng *et al.* 2007; Galli *et al.* 2008) that may have resulted from past major earthquakes. This method often can identify a few past major earthquakes that have ruptured the ground surface at a particular site. It has been applied to normal, reverse and strike-slip faults. However, interpretation of offset strata and fault-rupture related features is sometimes debatable, while the earthquakes cannot be dated directly (only soil markers can be used to bracket the event times) leaving large uncertainties (e.g. Hilley & Young, 2008a,b). The second approach is based upon the cosmic-ray exposure dating of preserved, seismically exhumed normal fault scarps or *nastri* (Zreda & Noller, 1998; Mitchell *et al.* 2001; Benedetti *et al.* 2002, 2003; Palumbo *et al.* 2004). Developed in the last 10 yr, the approach can recover both the age and slip of the last few major earthquakes on normal faults that have a well-preserved escarpment at the surface (Fig. 1). The method is based on the fact that the interaction of cosmic rays with the rocks exposed at the Earth's surface produces specific cosmogenic isotopes within these rocks (e.g. Gosse & Phillips 2001). This production inventory increases with time, and production rate (neglecting effects of Earth's magnetic field variations) is constant but decreasing with the rock burial depth (maximum production in first ∼2 m, depending primarily on rock density). Thus, the accumulation of these exotic isotopes over time may be used to infer the time since faulting exposed the scarp face to cosmogenic radiation. This is particularly advantageous for dating slip events along normal faults, as strong earthquakes on such faults lead to exhumation of a new section of the fault plane (Fig. 1). Limestone rocks typically preserve exhumed fault planes from denudation over times long enough to encompass several large earthquake events (∼10–20 kyr, e.g. Armijo *et al.* 1992; Piccardi *et al.* 1999). The target atoms in those rocks produce cosmogenic ^{36}Cl, hence chlorine is an ideal isotopic system to date such slip events.

More specifically, normal fault rock-scarps are generally partly covered by colluvial wedges (colluvium) that result from disaggregation and transport along the scarp. The ^{36}Cl concentration depth-curve for a limestone scarp section still buried under the colluvium has an exponential shape—just before an earthquake exhumes the scarp face (Fig. 2a). Once the earthquake has occurred, the newly exposed scarp section starts accumulating ^{36}Cl at an accelerated rate due to its enhanced exposure to cosmic radiation. The ^{36}Cl concentration along the exposed scarp section is thus the sum of the ^{36}Cl produced below the ground surface prior to its earthquake exhumation and of the ^{36}Cl that is being accumulated above the ground surface after the earthquake (Fig. 2b). Thus, as large earthquakes repeat on a normal fault and exhume deeper portions of its scarp,

© 2010 The Authors, *GJI*, **182,** 36–72
Journal compilation © 2010 RAS

Downloaded from https://academic.oup.com/gji/article-abstract/182/1/36/562733 by guest on 01 February 2019

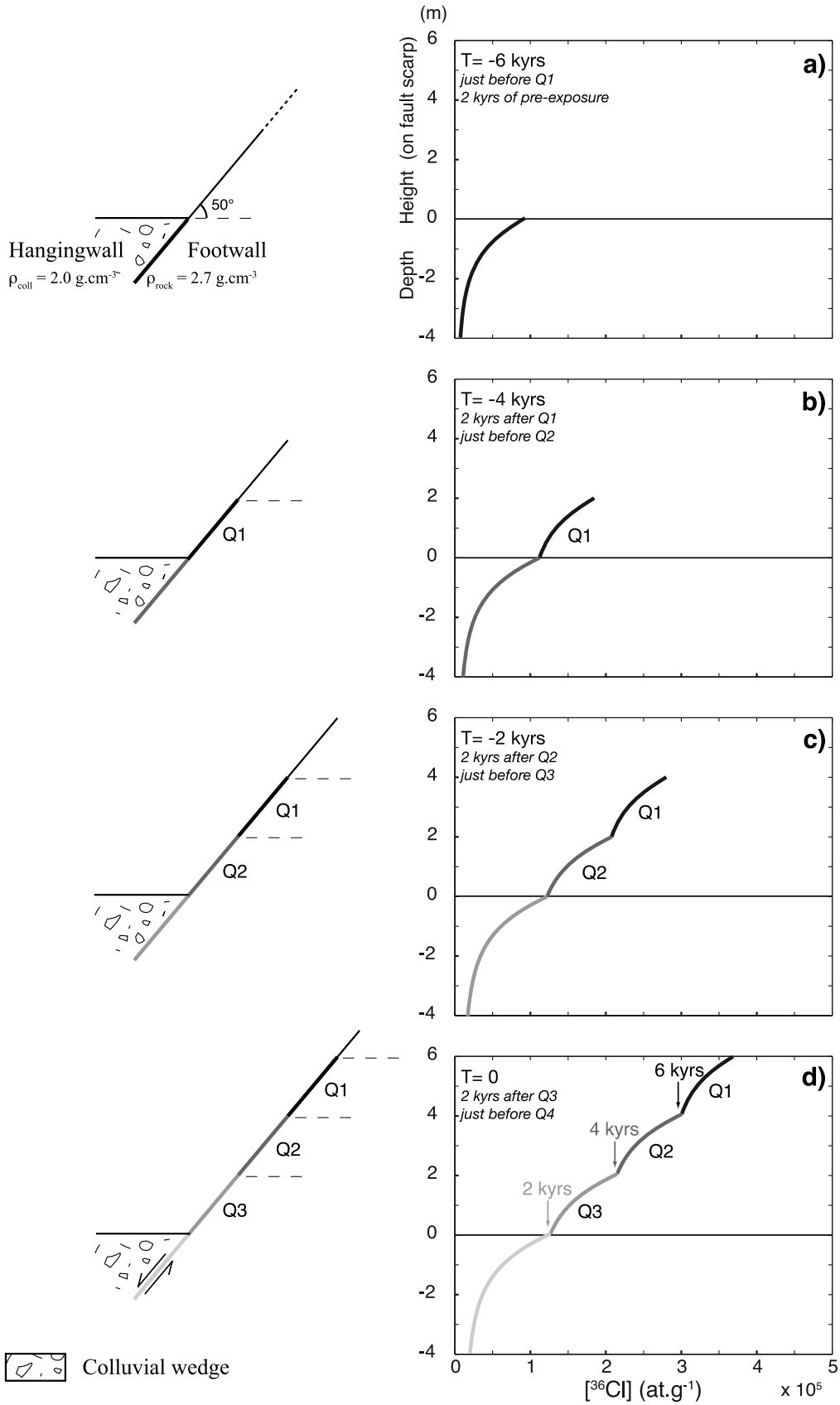

Figure 2. Theoretical profile of [^{36}Cl] versus fault scarp height expected to result from a sequence of three similar, regular earthquakes (labelled Qi; modified after Palumbo *et al.* 2004). Recurrence time is 2 kyr, vertical on-fault slip 2 m, and pre-exposure duration 2 kyr. Calculations assume a constant geomagnetic field. Left-hand panel shows fault and colluvial wedge geometry, together with earthquake exhumation history. Colluvium and scarp rock densities are indicated. Right-hand panel shows the evolution of the [^{36}Cl]-scarp height profile as the earthquakes repeat.

Downloaded from https://academic.oup.com/gji/article-abstract/182/1/36/562733 by guest on 01 February 2019

the ^{36}Cl concentration profile along the entire exposed scarp should take a shape made of a series of exponential sections separated by sharp discontinuities (Figs 2c and d). Those discontinuities reflect boundaries between each major earthquake rupture, while the vertical separation between two successive discontinuities provides a measure of the displacements produced by the earthquakes. The few pioneer studies performed with the ^{36}Cl method have demonstrated the validity of this theoretical framework showing that the ^{36}Cl dating approach is a powerful way to find the number, age and displacement of the last few major earthquakes (Mitchell *et al.* 2001; Benedetti *et al.* 2002, 2003; Palumbo *et al.* 2004).

Although the ^{36}Cl dating approach seems able to infer earthquake information, it is unclear how much uncertainty surrounds this information. In this contribution, we assess the resolution of this method by examining the effects of all scaling factors that modulate the ^{36}Cl production, hence the ^{36}Cl concentrations in the seismically exposed rocks. We develop a revised modelling code that includes all factors that may affect the ^{36}Cl concentrations (colluvium dip, density and chemical composition; scarp dip; upper eroded scarp dip; variable content of the samples in target elements; possible denudation of the scarp; geomagnetic field temporal variations; possible snow cover). The code also integrates the present knowledge of the ^{36}Cl production mechanisms and rates (from Schimmelpfennig *et al.* 2009). In so doing, we show that most of these 'scaling factors' have important effects on the final ^{36}Cl concentrations. We then examine the sensitivity of the new modelling to the complexity of the earthquake history such as pre-exposure duration and slip history, small versus large events, and temporally clustered earthquakes. This allows us to discuss the range of uncertainties that affect the modelling of a measured ^{36}Cl concentration profile and its impact on the accuracy of an inferred seismic history. We then apply our code to a data set acquired on the Magnola normal fault, Central Italy (Palumbo *et al.* 2004). We show that our code refines the seismic history of the fault, and helps quantify the uncertainties in the number, ages, and displacements of the past earthquakes.

2 OVERVIEW OF THE ^{36}CL DATING APPROACH

The interaction of cosmic rays with rocks exposed at the Earth's surface produces cosmogenic isotopes within these rocks (e.g. Gosse & Phillips 2001). For most common crustal rocks, the isotopes produced are ^{3}He, ^{10}Be, ^{26}Al, ^{36}Cl, and ^{21}Ne. The isotopes ^{10}Be ($t_{1/2} = 1.5 \times 10^6$ yr, with $t_{1/2}$ the isotope half-life), ^{26}Al ($t_{1/2} = 7.5 \times 10^5$ yr) and ^{36}Cl ($t_{1/2} = 3 \times 10^5$ yr) have thus far received the greatest attention. In the absence of denudation, the concentration of a particular isotope in a rock varies as a function of rock exposure time (t) and burial depth (z), as

$$\mathrm{d}N(z,t)/\mathrm{d}t = P(z,t) - \lambda \times N(z,t), \quad (1)$$

where for the isotope considered, N is the number of atoms, P is the isotope production rate, λ is the decay constant and $\mathrm{d}N/\mathrm{d}t$ is the rate of change. The abundance of cosmogenic isotopes increases with exposure time until a steady state is reached in which production and decay of the cosmogenic isotope are balanced; this usually occurs over 4–5 half-lives of the isotope. Production rates decrease exponentially with depth such that cosmogenic nuclides are only significantly produced in the first ~ 2 m of the surface (e.g. Gosse & Phillips 2001). Cosmogenic exposure dating thus provides a means of inferring how long a sample has resided near the Earth's surface.

As large earthquakes repeat on a normal fault, deeper sections of the fault plane are progressively exhumed (Fig. 2). The earthquake succession progressively forms a steep, topographic escarpment at the surface. Provided that the escarpment is preserved from denudation, its surface represents the entire record of fault movement that has affected the ground surface (Fig. 2). In carbonate environments, the exhumed escarpments generally preserve the record of past earthquakes over long time spans (commonly 10–15 kyr). Beyond such a time span, as for other rock types, the escarpment suffers significant denudation. This is why only limestone fault scarps can be analysed for past earthquake recovery using the cosmogenic dating techniques. Over a 10–15-kyr-long time period, only a few large earthquakes generally occur on a normal fault, each one exhuming the scarp by tens of cm to a few metres at most (e.g. Manighetti *et al.* 2007). The maximum height of the limestone scarps that can be studied with cosmonuclides is thus 10–15 m at most (e.g. Armijo *et al.* 1992; Piccardi *et al.* 1999; Galli *et al.* 2008).

Limestones contain ^{40}Ca,^{39}K and ^{35}Cl that, when exposed to cosmic rays, act as target elements producing *in situ* ^{36}Cl. Most of the ^{36}Cl found in rocks results from these cosmogenic reactions. The production rate of *in situ* ^{36}Cl is primarily related to the flux of cosmic rays that interacts with Earth's surface as well as the energy of the incident cosmic particles reaching the ground surface. Depending on their energy, three main cosmogenic processes reactions may produce *in situ* ^{36}Cl: (1) spallation of the rock target elements Ca, K, Ti and Fe occurs when high-energy secondary cosmic-ray neutrons impact the target nuclides breaking them into nuclides with smaller atomic masses. This process is most efficient at the ground surface and decreases with depth; (2) slow negative muons may be captured by ^{40}Ca and ^{39}K atoms resulting in the production of ^{36}Cl cosmogenic nuclide. Because muon interactions with atoms are limited, they can penetrate to greater depths than strongly interacting particles, so that the relative contribution of the muon-capture component to the *in situ* ^{36}Cl production increases with depth; (3) low-energy thermal and epithermal neutrons are formed when fast neutrons collide repeatedly with atoms in the atmosphere and rock, and consequently loose energy. These thermal neutrons can then be captured by the nuclei of the ^{35}Cl target elements to form cosmogenic ^{36}Cl. These absorption reactions are most important in the top few metres of the ground. In addition to the cosmogenic reactions described here, in rocks with high U and Th concentrations,^{36}Cl can also be radiogenically produced when ^{35}Cl captures some of the low-energy neutrons generated by radiogenic decay of U and Th or by fission of ^{238}U.

The reactions described above are well understood and each quantitatively formalized (e.g. Gosse & Phillips 2001; Schimmelpfennig *et al.* 2009). However some uncertainties remain regarding their relative contribution to the total ^{36}Cl production because it is difficult to separately measure the ^{36}Cl production rate associated with each of the above reactions.

In particular, the spallation production rate from the ^{40}Ca target element has been evaluated between 48.8 $\pm$ 3.5 and 66.8 $\pm$ 4.4 atoms of ^{36}Cl per g of Ca per yr (e.g. Schimmelpfennig *et al.* 2009). Ongoing research is presently conducted to refine that production rate. Schimmelpfennig *et al.* (2009) suggest that 'elementary' production rates are better estimated when measured from isolated, pure chemical elements. The spallation production rate of 48.8 $\pm$ 3.5 at. of ^{36}Cl g^{-1} Ca yr^{-1}, which was estimated from pure calcite samples (Stone *et al.* 1996), is thus the one we adopt in this paper (Table 1).

In addition to spallation reactions, the slow negative muon stopping rate at the land surface is debated, but measurements are too few at present to provide a well constrained range of uncertainties;

Downloaded from https://academic.oup.com/gji/article-abstract/182/1/36/562733 by guest on 01 February 2019

Table 1. Parameters used in the calculations. 'Reference parameters' are taken to be similar to those of the Magnola site (Palumbo *et al.* 2004) analysed in Section 5.3. 'Elementary' production rates used in the modelling are listed (more details in Supplement 1). Spallation rates on K, Ti and Fe are indicated in italic because our samples do not contain those elements (see MA3c-mean scarp rock composition, Table 2). Those spallation rates are however included in the Matlab® code to allow calculations on samples that would contain those elements.

Reference parameters
Latitude = N42°07.107; Longitude = E13°26.543
Elevation = 1255 ± 5 m a.s.l.
For a constant geomagnetic field (Stone 2000): $S_{el,f} = 2.750$ and $S_{el,\mu} = 1.703$
For a variable geomagnetic field: see Supplement 4
Chemical composition of rock and colluvium: see Table 2
Magnola site MA3 complementary parameters
Colluvium dip $\alpha = 30° \pm 3$; scarp dip $\beta = 45° \pm 2$; upper scarp dip $\gamma = 30° \pm 5$
$so_{f,e} = 0.926$ and $\Lambda_{f,e} = 116.6$ g cm^{-2} (in the direction perpendicular to fault scarp surface)
$so_{f,d} = 0.926$ and $\Lambda_{f,d} = 145.7$ g cm^{-2} (in the direction perpendicular to colluvium surface)
$so_{\mu} = so_f$ and $\Lambda_{\mu} = 1500$ g cm^{-2}
H = 20 m
Mean scarp density $\rho_{rock} = 2.70 \pm 0.01$ g cm^{-3}
Mean colluvium density $\rho_{coll} = 1.5 \pm 0.1$ g cm^{-3}
Most important reference 'elementary' production rates for limestone (more details in the Matlab® codes *clrock.m* and *clcoll.m*, see Supporting Information, Supplement 1)
Spallation on Ca: $\Psi_{36Cl\_Ca0} = 48.8 \pm 3.5$ at. of ^{36}Cl. g of Ca . yr^{-1} (Stone *et al.* 1996)
Spallation on K: 162 ± 24 at. of ^{36}Cl. g of K . yr^{-1} (Evans *et al.* 1997)
Spallation on Ti: 13 ± 3 at. of ^{36}Cl. g of Ti . yr^{-1} (Fink *et al.* 2000)
Spallation on Fe: 1.9 ± 0.2 at. of ^{36}Cl. g of Ti . yr^{-1} (Stone 2005)
Slow negative muons stopping rate at land surface: $\Psi_{\mu,0} = 190$ muon.g^{-1} yr^{-1} (Heisinger *et al.* 2002)
Neutron attenuation length: 208 g cm^{-2} (e.g. Gosse and Phillips, 2001)
Neutron apparent attenuation length for a horizontal unshielded surface: 160 g cm^{-2}
Muon apparent attenuation length for a horizontal unshielded surface: 1500 g cm^{-2}

currently, a single value of 190 muons g^{-1} yr^{-1} is generally adopted (Heisinger *et al.* 2002).

Finally, neutrons and muon density exponentially decreases with the apparent attenuation length Λ (decrease follows $e^{-z/\Lambda}$, where Λ is the distance at which half of the flux has been attenuated). For neutrons, Λ is estimated between 160 (e.g. Gosse & Phillips 2001) and 177 g cm^{-2} (Farber *et al.* 2008) for a horizontal unshielded surface, while it is estimated around 1500 g cm^{-2} (Gosse & Phillips 2001; Heisinger *et al.* 2002) for muons. Here we use the values of 160 and 1500 g cm^{-2} as reference for neutrons and muons, respectively (on a horizontal surface), as adopted in reference papers (e.g. Gosse & Phillips 2001; Schimmelpfennig *et al.* 2009).

Given our present knowledge of the production rates for each contribution, if one knows the instantaneous flux of cosmic rays arriving at a given rock on Earth's surface whose chemical composition is known, one can calculate the total ^{36}Cl production rate as a function of depth. Yet, when dealing with geological timescales (here 10–15 kyr) and evolving features (such as repeatedly slipping faults), secular variations in cosmic ray flux due to (i) variations in the intensity of the primary cosmic radiation; (ii) changes in the interplanetary magnetic field and solar modulation of the galactic cosmic radiation; (iii) changes in the geomagnetic field; (iv) variations in atmospheric shielding; and (v) variations in the character and topography of the studied landform surface over time must be considered (Gosse & Phillips 2001). The spatial variability of the production rate is generally accounted for by a number of 'scaling factors' that integrate the specific site properties (latitude, longitude, elevation and specific shielding effects) into the production rate calculations. By contrast, the time variability of the production rate is rarely integrated because the factors that govern it are insufficiently known.

Taking into account these processes, the total sample-specific *in situ* ^{36}Cl production rate [$P_{total}(z)$ in atoms of ^{36}Cl g^{-1} yr^{-1}] for a preserved rock sample (i.e. sustaining no denudation) of finite thickness standing at mass depth z (in g cm^{-2}) close to the ground surface, can be calculated (Gosse & Phillips 2001; Schimmelpfennig *et al.* 2009):

$$P_{total}(z) = S_{el,s} F_s Q_s P_s(z) + S_{el,\mu} F_\mu Q_\mu P_\mu(z) + S_{el,s} F_n [Q_{eth} P_{eth}(z) + Q_{th} P_{th}(z)] + P_{rad}. \quad (2)$$

Subscripts refer to the type of reaction, with *s* for spallation, *n* for capture of all types of low-energy neutrons, *eth* for capture of specific epithermal neutron, *th* for capture of specific thermal neutron, μ^- for capture of slow negative muons and *rad* for radiogenic production. P_i is the sample-specific ^{36}Cl production rate resulting from reaction *i*, as a function of sample chemical composition. Q_i is the sample thickness integration factor for the reaction *i*, required from the production rate being calculated at mass depth z in g cm^{-2}. Finally, S and F are scaling factors. $S_{el,s}$ and $S_{el,\mu-}$ taken to include the summed effects of elevation and latitude (*el*), for spallation (*s*) and muons capture respectively (μ^-). $S_{el,s}$ and $S_{el,\mu-}$ may vary with time if temporal variations of the geomagnetic field are included. F_i is a scaling factor made to sum up all the corrections (for reaction *i*) related to shielding effects (topographic, geometric and cover shielding, $0 < F_i \leq 1$; $F_i = 1$, no shielding). All reference production rates are reported in Table 1, while their uncertainties are further discussed in Section 6.

Downloaded from https://academic.oup.com/gji/article-abstract/182/1/36/562733 by guest on 01 February 2019

When applied to a sample on an uneroded, unshielded horizontal surface having the same composition as the limestone rocks of the Magnola site that we analyse in Section 5.3 (Table 2), with no change in the geomagnetic field, the production rates due to different pathways of ^{36}Cl production are calculated using eq. (2) (Fig. 3). The total ^{36}Cl production rate approximately decreases exponentially with depth. Spallation is the most important reaction in the first 2 m of the surface; at greater depth, slow negative muon capture becomes the dominant source of ^{36}Cl production. Thermal and epithermal neutron absorption contribute little to the total ^{36}Cl production in limestone, as [Cl_{nat}] is only $\sim$10 ppm in our reference rocks (Table 2). Since the ^{36}Cl decay constant (λ) and the attenuation lengths (Λ) are well established, the combination of eqs (1) and (2) allows derivation of the exposure time (t) of a sample residing at a depth z, from the measurement of its ^{36}Cl concentration.

Each earthquake rupturing a normal fault exposes new materials on the scarp (Fig. 2). The samples highest on the scarp have been exposed the longest and hence should have the highest concentrations of cosmogenic nuclides (Fig. 2). Previous studies (Mitchell *et al.* 2001; Benedetti *et al.* 2002, 2003; Palumbo *et al.* 2004) have inferred past earthquake histories of a few normal faults having a preserved limestone scarp using this approach but in most studies the modelling of the [^{36}Cl] profiles was conducted based on a simplified geometry of the sampling sites, and without integrating the time variations in the geomagnetic field nor the possible denudation of the fault scarp. Here, we develop a novel modelling code made to include all the factors that may affect the ^{36}Cl concentrations eventually measured in seismically exhumed limestone fault scarp rocks (code available in Supplement 1).

3 ROCK SAMPLING AND ^{36}CL CONCENTRATION MEASUREMENT METHODOLOGY

3.1 Field sampling

Analysed fault scarps must be exposed to cosmic rays by seismotectonic exhumation, rather than by denudation processes such as river scouring or gravitational collapse of the colluvial wedge. To avoid any ambiguity, fault scarp sections close to incising river channels should not be targeted. The selected fault surface also needs to be uneroded by physical or chemical processes. The observation of fresh striations on the scarp surface may indicate this is the case, whereas the existence of numerous pits and gullies on the scarp surface is an indication of significant denudation.

Once a target scarp has been identified, samples should be collected from the uppermost 2–4 cm of the scarp surface. Because the amount of produced ^{36}Cl is variable from surface to depth, the exact sample thickness must be used to model the exposure age. Sampling should ideally be performed along a single, continuous top-to-base profile, along the fault slip direction (example in Fig. 1b). We have used a diamond cutter attached to an edge grinder capable of cutting into the rock to $\sim$3 cm to excavate two vertical slots on the fault scarp, separated laterally by 15 cm at most. The vertical scarp section enclosed between the two lines is then cut continuously from top to base into successive, horizontal, 5 cm-high rock slabs. Then, samples can be collected with a hammer and a cold chisel. We typically sample every 10 cm, so that each sample is made of two successive 3 cm thick slabs. This should guarantee a sample weight of 0.5–1 kg enough to yield accurate ^{36}Cl measurements at any site. Sample position may be measured from a zero reference taken to coincide with the ground surface (surface of the colluvium). Site elevation, latitude, and longitude must be measured. Finally, detailed mapping of the site includes measurements of the dip of the sampled fault plane and of the colluvium surface, the geometry and dip of the older sections of the fault escarpment above the sampled scarp, and possible large-scale shielding due to neighbouring relief.

3.2 Sample preparation for chemical Cl extraction

Crystallized veins should first be removed from the sample, for their formation may be different from that of the fault scarp. A small piece of each sample ($\sim$30 g) must be kept for subsequent rock density measurement (ρ_{rock}; see Supplement 2). Next, sample should be crushed, and the 250–500 μm fraction should be isolated by sieving.

The 250–500 μm fraction of each sample is then leached and dissolved following the chemistry protocol of Stone *et al.* (1996). After complete dissolution of the crushed and leached samples (deionized water and HNO_3 successive leaching), and the addition of a chlorine carrier, Cl is precipitated as AgCl. Note that the ^{36}Cl's isobaric element ^{36}S is concurrently removed through the precipitation of $BaSO_4$ to avoid any interference in the ^{36}Cl counting during the subsequent Accelerator Mass Spectrometer (AMS) measurements. More details on chemistry protocol can be found in Supplement 2. To allow simultaneous Cl and ^{36}Cl determination by isotope dilution AMS (ID-AMS), samples are spiked with a known amount of isotopically enriched stable chloride carrier (Desilets *et al.* 2006a and references therein).

To track any Cl contamination in the chemistry process, a chemistry blank is coupled with each series of 10–15 samples and measured by AMS with its respective series.

3.3 AMS measurements and ^{36}Cl concentration determination

Both [^{36}Cl] and [Cl_{nat}] are determined simultaneously from the AMS measurements. Total Cl concentration is calculated from the ^{35}Cl/^{37}Cl ratio, which is measured on Faraday cups in the AMS ion injector before acceleration (e.g. Finkel & Suter 1993; Elmore *et al.* 1997). The measured ^{35}Cl/^{37}Cl ratio is the result of a simple mixing between carrier Cl of known ^{35}Cl/^{37}Cl ratio and concentration, and sample Cl_{nat} of unknown concentration but known ^{35}Cl/^{37}Cl natural ratio of 3.127 (Desilets *et al.* 2006a) (see Supplement 3 for more details).

Commonly, the analysed rock samples contain 10^6–10^7 atoms of ^{36}Cl, and 10^{18}–10^{19} atoms of Cl_{nat}. Blanks generally have 1–5 10^5 atoms of ^{36}Cl, and 1–5 10^{17} atoms of Cl_{nat}, which represent about 5 per cent of the samples concentrations. Blank corrections are calculated by removing the number of atoms of ^{36}Cl and Cl_{nat} yielded for the blank ($n_{36Cl,blank}$ and $n_{Clnat,blank}$) from the corresponding number of atoms in the sample ($n_{36Cl,sample}$ and $n_{Clnat,sample}$) (see Supplement 3).

3.4 Complementary chemical analyses

Analysis of host rock composition

To determine the ^{36}Cl concentration produced by spallation, target elements concentrations ([Ca], [K], [Ti] and [Fe]) must be

Downloaded from https://academic.oup.com/gji/article-abstract/182/1/36/562733 by guest on 01 February 2019

Table 2. Mean chemical composition of the samples from the Magnola site (Palumbo *et al.* 2004). Mean composition of the buried scarp rocks: *MA3c-mean scarp rock*. Mean composition of five pebbles from the colluvial wedge: *MA3c-pebbles mean*. Mean soil composition derived from five samples taken in the colluvial wedge: *MA3c-soil mean* (see Supplement 6 for details). Measurements of elements in columns 1–60 were done at the SARM-CRPG facility (Nancy, France). Corresponding uncertainties on the measured concentrations are given at: http://helium.crpg.cnrs-nancy.fr/SARM/analyses/roches.html. Compositions given in per cent are converted into ppm in the Matlab® routine. Columns 59 and 60 have null values. They are however also converted into ppm in the Matlab® routine: O, rock coming from the different oxides (columns 44–53), and O, water from H_2O_{tot} (56). Column 49, the mean value of Ca coming from CaO (per cent), is not used as we use instead the precise value of [Ca] determined by ICP-OES for each sample (column 62, 360 000 ppm is the mean value used in the synthetic profile calculations). Mean CaO (per cent) is only used to calculate O, rock. Column 51, K_2O should also be measured at ICP-OES for each sample, as is CaO. However as our samples lack potassium, no supplementary column has been created. Column 61, the [Cl_{nat}] concentration determined at the AMS for each sample is used in the Matlab® routine to calculate the [^{35}Cl] concentration (here, the value of 10 ppm is the mean value used in the synthetic profile calculations).

	1 As (ppm)	2 Ba (ppm)	3 Be (ppm)	4 Bi (ppm)	5 Cd (ppm)	6 Ce (ppm)	7 Co (ppm)	8 Cr (ppm)	9 Cs (ppm)
MA3c – mean scarp rock	0.00	3.081	0.00	0.00	0.268	0.525	2.115	0.00	0.00
MA3c – Pebbles mean	0.00	7.465	0.00	0.00	0.387	1.599	1.366	0.00	0.19
MA3c – Soil mean	4.423	133.4	1.599	0.188	0.944	38.03	6.266	27.62	4.2
	10 Cu (ppm)	11 Dy (ppm)	12 Er (ppm)	13 Eu (ppm)	14 Ga (ppm)	15 Gd (ppm)	16 Ge (ppm)	17 Hf (ppm)	18 Ho (ppm)
MA3c – mean scarp rock	0	0.123	0.085	0.023	0	0.111	0	0	0.028
MA3c – Pebbles mean	0	0.208	0.121	0.06	0.176	0.234	0	0.071	0.042
MA3c – Soil mean	12.44	1.96	1.059	0.595	5.777	2.395	0.486	1.71	0.376
	19 In (ppm)	20 La (ppm)	21 Lu (ppm)	22 Mo (ppm)	23 Nb (ppm)	24 Nd (ppm)	25 Ni (ppm)	26 Pb (ppm)	27 Pr (ppm)
MA3c – mean scarp rock	0	0.648	0.013	0	0	0.474	21.52	5.346	0.114
MA3c – Pebbles mean	0	2.112	0.018	0	0.241	1.607	10.41	0.61	0.432
MA3c – Soil mean	0	20.35	0.159	0.13	7.304	15.81	21.61	12.54	4.335
	28 Rb (ppm)	29 Sb (ppm)	30 Sm (ppm)	31 Sn (ppm)	32 Sr (ppm)	33 Ta (ppm)	34 Tb (ppm)	35 Th (ppm)	36 Tm (ppm)
MA3c – mean scarp rock	0.387	0	0.097	0	116.1	0	0.018	0.038	0.013
MA3c – Pebbles mean	1.809	0	0.291	0	137.5	0.015	0.034	0.334	0.017
MA3c – Soil mean	35.31	0.312	2.912	1.2	126.8	0.511	0.346	7.454	0.152
	37 U (ppm)	38 V (ppm)	39 W (ppm)	40 Y (ppm)	41 Yb (ppm)	42 Zn (ppm)	43 Zr (ppm)	44 SiO_2(Si) %	45 Al_2O_3(Al) %
MA3c – mean scarp rock	0.311	0	0	1.372	0.081	0	0	0	0.031
MA3c – Pebbles mean	0.325	1.585	0	1.807	0.112	5.212	3.247	0.309	0.151
MA3c – Soil mean	1.142	35.01	0.668	12.76	1.027	43.11	74.8	10.79	4.745
	46 Fe_2O_3(Fe) %	47 MnO(Mn) %	48 MgO(Mg) %	49 CaO(Ca) %	50 Na_2O(Na) %	51 K_2O(K) %	52 TiO_2(Ti) %	53 P_2O_5(P) %	54 B (ppm)
MA3c – mean scarp rock	0	0.004	0.39	55.37	0	0	0	0.034	2
MA3c – Pebbles mean	0.066	0.005	0.499	54.85	0	0.017	0.008	0.083	2
MA3c – Soil mean	1.837	0.038	0.791	43.04	0.065	0.438	0.223	0.241	13.6
	55 Li (ppm)	56 H_2O_{tot} %	57 S_{tot} %	58 CO_{2tot} %	59 O, rock	60 O, water	**61** $Cl_{nat,AMS}$ (ppm)	**62** Ca_{ICP} (ppm)	
MA3c – mean scarp rock	0.919	0.288	0.015	43.85	0	0	10	360 000	
MA3c – Pebbles mean	1.3	0.326	0.014	43.818	0	0	10	360 000	
MA3c – Soil mean	15.1	3.722	0.036	36.81	0	0	10	360 000	

Notes: Columns 1–60: Mean composition per sampling site. Columns 61, 62: Concentration per sample (Cl_{nat} and Ca).

© 2010 The Authors, *GJI*, **182**, 36–72
Journal compilation © 2010 RAS

Downloaded from https://academic.oup.com/gji/article-abstract/182/1/36/562733 by guest on 01 February 2019

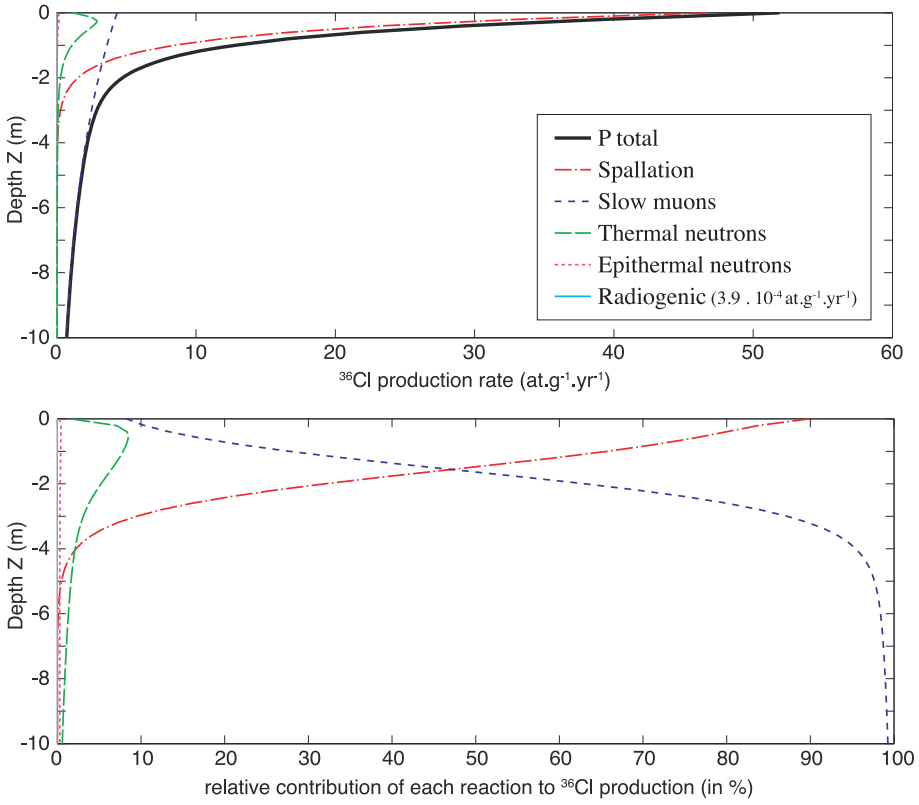

Figure 3. Contribution of the various cosmogenic and radiogenic sources to the production of *in situ* ^{36}Cl in the first 10 m below the ground surface. Calculations are done with our Matlab® code (Supplement 1), for a horizontal surface and a pure limestone chemical composition (reference parameters in Table 1, $\rho_{rock} = 2.7$ g cm^{-3}). (a) Production rates in atoms g^{-1} yr^{-1}. (b) Relative contribution (reported in per cent) of each production source. Radiogenic production is extremely low resulting in a non-visible curve.

measured in each sample. Ca and K concentrations are also required to model properly the slow muon capture production source. Concentrations, especially those of Ca and K, need to be determined with great accuracy as a ±2 per cent uncertainty in [Ca] for instance turns into a ±2 per cent uncertainty in the modelled ^{36}Cl concentrations. We thus recommend that the Ca and K content of the samples be determined by ICP-AES on aliquots of the sample solution (Supplement 2). Less abundant target elements in limestone (Ti and Fe) can be measured by spectrometry analysis (TiO_2, Fe_2O_3) of the crushed-leached samples (Supplement 2). The other sources of ^{36}Cl production depend on the bulk rock composition. Thus, it is also necessary to measure the concentrations of major (spectrometry) and trace elements (ICP-MS) in the crushed-leached samples (Carignan *et al.* 2001, Table 2 for site reference parameters). Since the bulk rock composition typically doesn't vary significantly over the scarp, one analysis per metre is usually enough to determine a mean bulk rock composition that can be used in the modelling.

Analysis of colluvial wedge composition

Fault scarp rocks start accumulating ^{36}Cl while they are buried under tens of centimetres of colluvium (Fig. 2). The neutron absorption and muon capture reactions that produce most of the ^{36}Cl depend on the composition of the rock material above the sample, and so it is necessary to determine the chemical composition of the colluvial wedge. This requires sampling the colluvium, ideally in several metre-deep trenches excavated at the fault scarp base. The colluvium is generally composed of a mixture of limestone pebbles originating from the fault scarp mechanical disruption, and of soil that consists of organic material, partly dissolved carbonates, clays, water and other minor constituents (Govindaraju 1994). The chemical composition of the colluvial wedge thus ranges between that of the scarp limestone rocks and that of a soil. As a result, this material can be enriched in elements such as Al, B, Gd, Fe, Li, Si, Sm (e.g. Schimmelpfennig *et al.* 2009). The presence of such elements tends to decrease the total production rate in the buried scarp rocks.

3.5 Determination of the density of the fault scarp rocks and colluvium

The density of the fault scarp rocks is measured from the portions of samples removed prior to crushing. The density is determined by dividing the subsample dry weight by the weight that the subsample has when immersed in pure water (note that the method applies to non-porous samples only, see details in Balco & Stone 2003). Our experience with limestone rocks suggests that scarp rock density does not vary by more than ±0.5 per cent ($\rho_{rock} = 2.7 \pm 0.01$ at our reference site). Therefore, density values acquired each metre along the scarp height are representative of the average density value used in the modelling.

Downloaded from https://academic.oup.com/gji/article-abstract/182/1/36/562733 by guest on 01 February 2019

As colluvial wedge material is porous and poorly consolidated, its density may be estimated by weighting colluvium samples in boxes of known volume (Balco & Stone 2003). In the field, boxes should be filled and packed attempting to recreate the natural compaction of the material. By experience, as the method is less precise than for non-porous samples, the uncertainty on estimated densities is estimated to be ±5 per cent ($\rho_{\rm coll} = 1.5 \pm 0.1$ at our reference site).

4 DERIVING EXPOSURE TIMES FROM *IN SITU* ^{36}Cl CONCENTRATIONS: A MODEL REAPPRAISAL

To determine the exposure age of a sample, the history of the production rate of ^{36}Cl in that sample must be known. We developed analytical formulas that describe the scaling factors most important to normal fault analysis. We then introduce each analytical expression into eq. (2) (with the terms 'F' and 'S') to build a model that properly integrates all scaling factors, and allows accurate calculation of the ^{36}Cl concentrations accumulated over any period of time in any normal fault limestone scarp rock. The model is called **clxxxx.m** (**clrock.m** and **clcoll.m**) and corresponds to a modified and extended Matlab® version of the Excel® spreadsheet of Schimmelpfennig *et al.* (2009). Note that the thickness factors in our Matlab® code are modified compared to those reported in Gosse & Phillips (2001), to be used at depth. More details on the code can be found in Appendices A and B and Supplement 1 from where it can be downloaded.

In this section, we use the *clrock.m* and *clcoll.m* subroutines to build a series of synthetic ^{36}Cl concentration profiles that quantify the effects of each scaling factor on the ^{36}Cl production rate. All calculations fix the values of elevation, latitude, longitude, chemical composition and colluvium density (Tables 1 and 2), to values representative of the Magnola fault study detailed in Section 5.3. ^{36}Cl production rate is calculated either as a function of the scarp rock burial depth (Sections 4.1–4.4 in which all calculations are done for a constant geomagnetic field), or as a function of the rock position on the exposed scarp surface (Section 4.5 in which the calculations are done for a time-variable geomagnetic field). Together these graphs highlight that most scaling factors play a substantive role in palaeoseismic inferences, and as such cannot be ignored. Because normal fault earthquakes commonly produce surface displacements of a few metres at most (e.g. Manighetti *et al.* 2007), we consider ^{36}Cl production rate variations in the first ∼3–5 m of the ground.

4.1 Latitude and air pressure (elevation) scaling factors for a constant geomagnetic field

In most models, a single scaling factor (S_{el}) subsumes the effects of both latitude and elevation for neutrons and muons ($S_{el,s}$ and $S_{el,\mu-}$) (Stone 2000). We do the same here. At sea level and high latitude (SLHL), $S_{el,s}$ and $S_{el,\mu-} = 1$. The Earth's magnetic field deflects cosmic radiation such that the cosmic ray flux is minimum at the equator, and increases with higher latitudes up to a roughly constant value for latitudes greater than 60° (e.g. McElhinny & McFadden 1997). The ^{36}Cl production rate in a sample thus depends on the geomagnetic latitude of the site. This latitude dependency is accounted for by the $S_{el,s}$ and $S_{el,\mu-}$ scaling factors. As an example, a ±0.1° uncertainty on latitude leads to ±0.1 per cent uncertainty on both neutrons and muons scaling factors at the reference site.

On the other hand, cosmic rays loose energy as they interact with atoms into the atmosphere. The total flux that eventually arrives at Earth's surface thus depends on the thickness of the atmosphere that the radiation has traversed. In accordance, the ^{36}Cl production rate in a sample also depends on its elevation (assuming atmospheric pressure is constant over time). This altitude dependency is also taken into account in the $S_{el,s}$ and $S_{el,\mu-}$ scaling factors (see Supplement 4 for calculations). For example, a ±5 m uncertainty on elevation leads to a ±0.5 per cent variation of both scaling factors at the reference site. When estimating the latitude and elevation of a site with the handheld GPS instruments, the ∼5 m lateral and vertical uncertainties that commonly result on the measurements convert into a ∼1 per cent uncertainty on the calculated ^{36}Cl concentrations.

4.2 Shielding resulting from the specific geometry of active normal faults

The reference model for calculating the ^{36}Cl production assumes that cosmic radiation at the sample site is not shielded by surrounding high topography. In such an ideal condition, all the incident cosmic radiation that arrives from the atmosphere interacts with the exposed rocks. Yet, when dealing with normal fault escarpments, the scarp is a sloping surface that may be part of, and close to, topographic relief that may shield a significant portion of the incident radiation. This requires the production rate to be corrected for those effects.

As active normal faults rupture in successive large earthquakes, the footwall is progressively uplifted (Fig. 2). Over long time spans (commonly, several 10^4–10^6 yr), the fault motion forms a high, steep, cumulative escarpment (commonly, several hundred metres high, see black double arrow on Fig. 1a). Because the escarpment degradation increases overall with its exposure time, the cumulative escarpment generally exhibits an overall convex-up shape, with its youngest lower section being steeper than higher parts. It has been suggested that, over the short lifetimes of those scarplets, the colluvium that lies at the base of the escarpments acts as a stable geomorphic feature that can be used to measure the relative offset along the fault (Fig. 2, Armijo *et al.* 1992; Benedetti *et al.* 2002; 2003). Radiocarbon ages for samples from the colluvium seem to confirm this hypothesis (see Section 5.3).

The geometry of a normal fault scarp can be idealized by three parameters: the dip β of the scarplet plane, the dip γ of the older fault section further above the scarplet, and the dip α of the colluvium surface (Fig. 4b). If β is infinite ($\beta = \gamma$, Fig. 4a), the fault scarp rocks sustain two shielding effects over their exposure history: (1) any scarp rock is first buried below the colluvial wedge before its seismic exhumation. The scarp rocks thus sustain a 'coverage shielding', (2) any scarp rock, either buried or exposed, stands in the shadow of the fault footwall that blocks part of the incoming cosmic radiation. The scarp rocks thus also sustain a 'topographic shielding'. When the horizon in front of the fault plane is shielded by additional topography, a correction must be introduced accordingly (shielding calculations detailed in Appendix A).

For exposed samples, the attenuation length depends on the scarp dip. For samples still buried under the colluvium surface, it also depends on the dip and density of the colluvium. To calculate the corresponding attenuation length, we follow the method developed by Dunne *et al.* (1999). Calculations are provided in Appendix A.

Figs 5(a)–(c) (and Fig. A2) illustrate the effect of the changing of β (scarp), α (colluvial wedge), and $\rho_{\rm coll}$ (colluvium density) on the production rate at depth. In Fig. 5(a), β varies while $\alpha = 0°$ and $\rho_{\rm coll} = 2.0$ g cm^{-3}. The production rate is twice as high for shallow-dipping fault planes ($\beta < 45°$) than for steep ones

Downloaded from https://academic.oup.com/gji/article-abstract/182/1/36/562733 by guest on 01 February 2019

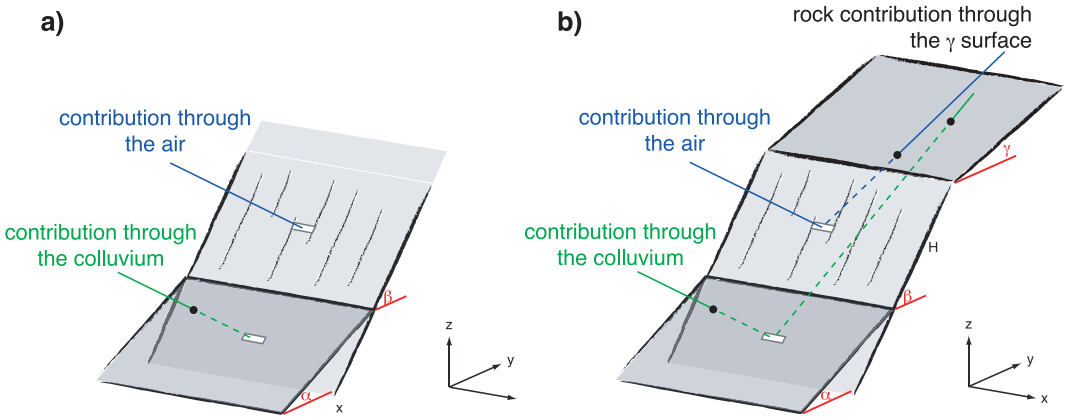

Figure 4. Schematic representation of the geometry of a normal fault scarp, associated colluvial wedge, and resulting shielding. α is colluvial wedge dip, β the basal scarplet dip and γ the dip of the upper part of the fault escarpment. H is the present height of the basal scarplet. (a) Simple case of $\beta = \gamma$. (b) When γ and β are different, buried samples (in green) receive cosmic rays passing through the colluvium ('colluvium contribution' of the flux), and cosmic rays passing through the scarp rock ('rock contribution' of the flux); the exhumed samples (in blue) receive both cosmic rays travelling through the air and cosmic rays passing through the rock.

($\beta > 75°$) — increasing depth augments this effect. This results in production-depth profiles along buried scarp sections having sharper exponential shapes for steeper faults.

Conversely, in Fig. 5(b), $\beta = 50°$, $\rho_{coll} = 2.0$ g cm^{-3} and α varies. The production rate varies with the colluvium dip—the scarp rocks accumulate ~7 times more ^{36}Cl when they are covered with a steep colluvium (minimum cover shielding). At 3 m below the ground surface, the fault scarp may accumulate about three times more ^{36}Cl if it is overlain by a 30°-dipping rather than an horizontal colluvial wedge.

Fig. 5(c) shows the impact of varying ρ_{coll} when $\alpha = 15°$ and $\beta = 50°$ on the production rate. At a given depth, the production rate increases as the colluvium density decreases. The variations are modest with a maximum increase by a factor of 2 in the first 3 m of burial when comparing the cases of $\rho_{coll} = 1.5$ and 2.7 g cm^{-3}. At 2 m-depth, a ±0.1 uncertainty on the colluvium density translates to a ±5 per cent uncertainty on the production rate.

Fig. 5(d) further highlights the combined effects of the scarp and colluvium dips on the production rate. A reference curve (grey) is calculated for $\beta = 45°$ and $\alpha = 30°$, with $\rho_{coll} = 1.5$ g cm^{-3}. The reference curve is assigned an error bar of ±5 per cent (2σ ~10 per cent), which represents the maximum analytical error typical of real [^{36}Cl] measurements (the error includes both chemical preparation and AMS measurements; see Supplement 5 for comparison with real data). The figure shows that a 5° deviation in either the scarp or the colluvium dip modifies the production rate by up to 25 per cent in the first 3 m of the buried scarp. In the case of a 5 per cent error on both α and β, the error on the modelled production rates can be as high as 55 per cent.

When the dip γ of the older fault section above the scarplet and the dip β of the scarplet differ by more than 10°, the calculations of the production rates are more complex (Fig. 4b and Fig. A1). In this case, sample shielding can be idealized as resulting from a fault scarp that is simplified as a finite plane of height H (along the fault plane of dip β, Fig. 4b). For this geometry, part of the shielded radiation passes through the top surface of the footwall, and may eventually interact with fault scarp rocks, whether they are exposed or buried. The rays passing through the γ-dipping top surface may thus contribute to increase the production, at least in the samples in the vicinity of the $\beta-\gamma$ break in slope. In a homogeneous rock, the importance of such a contribution depends on the sample position on the scarp, on the angle γ, and on the height H of the scarplet. The calculation of the resulting production rate, expressed as a scaling factor, is given in Appendix A. Figs 6(a) and (b) show the case of a 45°-dipping fault scarplet that abruptly give place to shallower fault surface of dip γ. Here, $\alpha = 30°$ and $\rho_{coll} = 1.5$ g cm^{-3}. Fig. 6(a) shows that the production rate in shallow buried samples (first metre) is increased by up to 10 per cent when H is small (<1 m). On the other hand, the production rate is increased by 5–10 per cent in the exposed samples less than 2 m from the γ-dipping surface (Fig. 6b). Thus, the samples near the $\beta-\gamma$ transition are influenced by the two effects described above (small H over their first stages of exhumation, and persistent proximity of the top surface) so that their ^{36}Cl concentration is augmented.

4.3 Effects of the chemical composition of the colluvial wedge

Part of the ^{36}Cl produced prior to scarp exhumation results from cosmic rays interacting with materials of the colluvial wedge before reacting with the footwall rock. Thus, the chemical composition of the colluvium will, in part, control production of ^{36}Cl below the colluvium. The chemical composition of colluvium cannot be predicted, thus we collected five samples of colluvium at various depths at Magnola fault site (see Fig. 15). It provides an example of the effect of colluvium composition on ^{36}Cl production in buried footwall rocks. We found that the chemical composition of colluvium clasts was similar to that of the fault scarp rocks (Table 2 and Supplement 6); however, the soil is depleted in calcium and enriched in rare earth elements and silicates. Fig. 7 shows the three concentration profiles computed at depth, which assume that the colluvium has a chemical composition identical to that of the scarp rocks, similar to that of its clasts, and similar to that of its soil (average composition; see Table 2). The differences in the ^{36}Cl concentrations resulting from composition differences are less than 3 per cent. Thus, in the absence of colluvium sampling, it seems reasonable to approximate the colluvial wedge composition with the average scarp rock composition.

4.4 Effects of denudation of the scarp surface

Denudation rates in limestone environments have been estimated to be between 0.005 and 0.03 mm yr^{-1} over time periods of

© 2010 The Authors, *GJI*, **182,** 36–72
Journal compilation © 2010 RAS

Downloaded from https://academic.oup.com/gji/article-abstract/182/1/36/562733 by guest on 01 February 2019

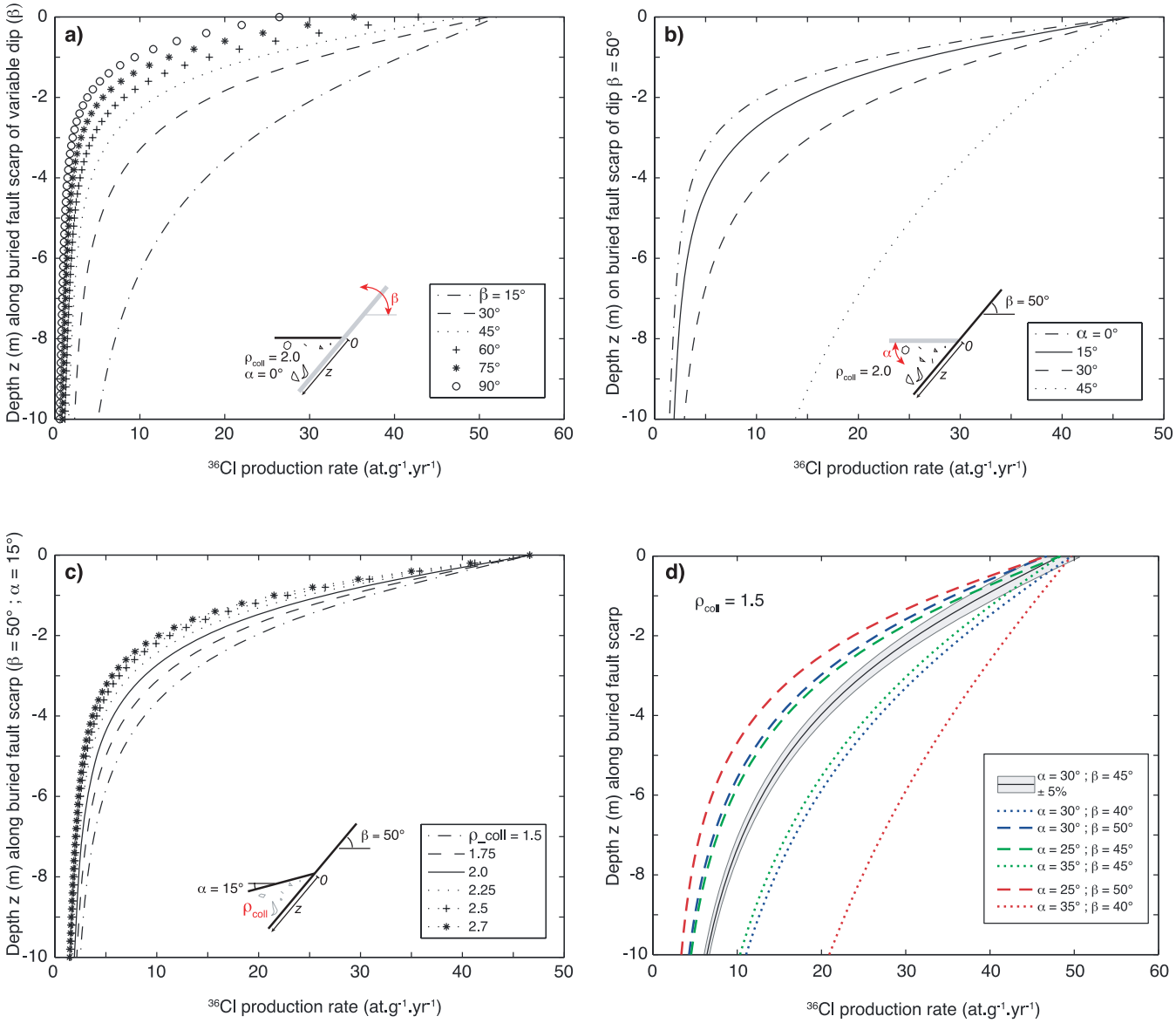

Figure 5. Effect of the fault scarp and colluvium geometry (dip) on the ^{36}Cl production rate (at.g^{-1} yr^{-1}) resulting in the buried fault scarp rocks (for a constant geomagnetic field). (a) Effects of the variations in the fault scarp dip (β). The colluvium is horizontal and of constant density ($\rho_{coll} = 2.0$ g cm^{-3}). (b) Effects of the variations in the colluvium dip (α). The fault scarp has a constant dip $\beta = 50°$ and the colluvium a density of 2.0 g cm^{-3}. (c) Effects of the variations in colluvium density. The fault scarp and colluvium have a constant dip $\beta = 50°$ and $\alpha = 15°$, respectively. (d) Combined effects of $\pm 5°$ uncertainty of the fault scarp and colluvium dips. A reference profile (continuous curve) is defined for common scarp and colluvium dip values ($\alpha = 30°$ and $\beta = 45°$). The grey band represents the ± 5 per cent uncertainty that would affect the reference profile, due to analytical measurement uncertainties. See discussion in text.

10–20 yr (e.g. Cucchi *et al.* 1995; Smith *et al.* 1995; Furlani *et al.* 2009), while those rates are generally not constrained for longer time spans. In the absence of well-documented denudation rates, we present in Fig. 8 the effect of denudation rates between 0 and 0.02 mm yr^{-1} on the predicted [^{36}Cl] along a periodically rupturing normal fault. The scenario is built for a sequence of three similar earthquakes (2 m each; Recurrence time Tr: 2 kyr) that rupture a 50°-dipping scarp covered by a horizontal, 2.0 g cm^{-3} density colluvium. Denudation is modelled as the progressive removal of the scarp surface perpendicular to that surface (details on Matlab® code in Appendix A). The effect of denudation is observed to be maximum on the highest, hence oldest, section of the scarp, with [^{36}Cl] decreasing around 15 per cent for the case denudation occurs at 0.02 mm yr^{-1}. This difference is significant and would convert into a minimum age difference of +1 kyr for the oldest event. This demonstrates that neglecting the scarp denudation may lead to an overestimate of the earthquake ages, with an error that increases with the earthquake age.

4.5 Effects of time fluctuations in the geomagnetic field

Assuming that Earth's magnetic field is constant appears reasonable when integrating production over long time spans. However when the timescales are short, as in this study, the geomagnetic field varies in both intensity and geometry (polar wander, non-dipole terms) over timescales of 1–10 ka (Merrill & McElhinny 1983; Guyodo & Valet 1999; Ohno and Hamano, 1993; Yang *et al.* 2000; Korte & Constable 2005a,b).

Downloaded from https://academic.oup.com/gji/article-abstract/182/1/36/562733 by guest on 01 February 2019

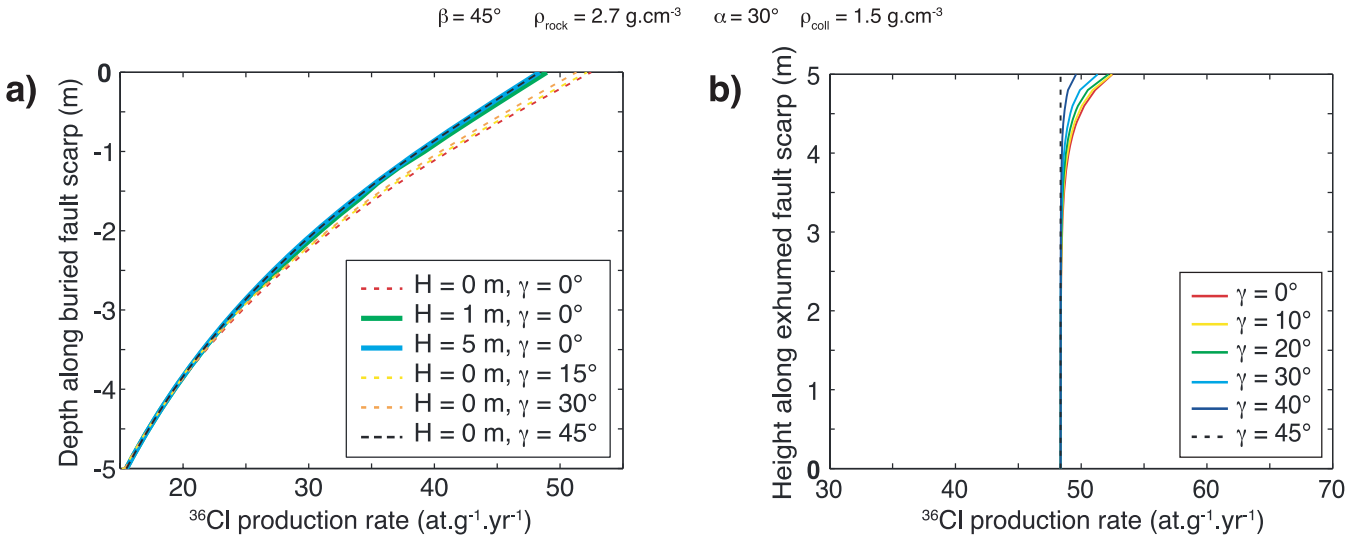

Figure 6. Effect of the upward shallowing of the fault scarp dip on the ^{36}Cl production rate (at g^{-1} yr^{-1}) resulting in the buried and exposed scarp rocks (for a constant geomagnetic field; other parameters indicated on figure). The scarplet of dip $\beta = 45^\circ$ shallows upward to a variable dip γ. H is height of the scarplet. (a) Effect of H and γ on buried samples. (b) Effect of proximity of $\beta - \gamma$ slope break on exposed samples.

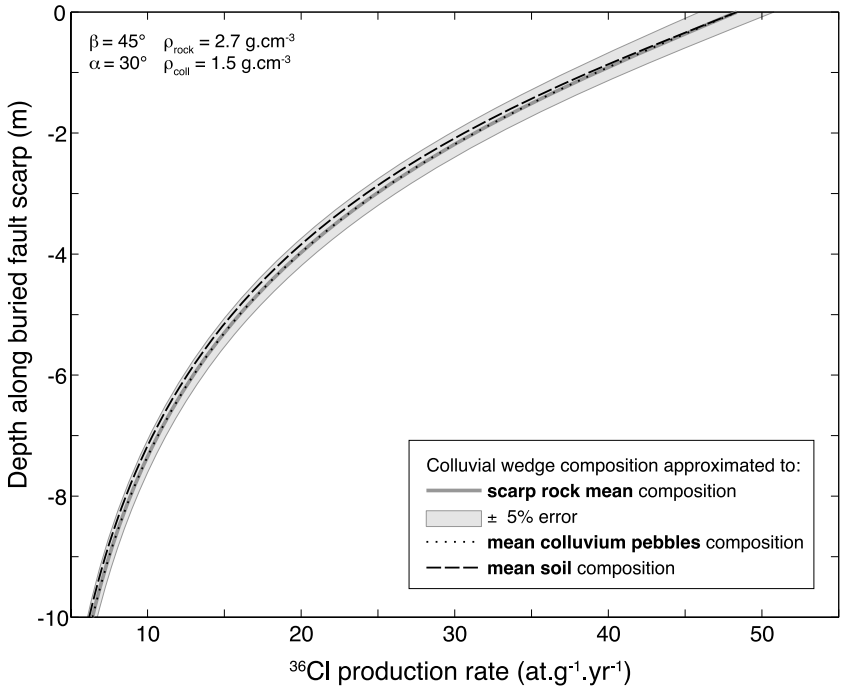

Figure 7. Effect of colluvium chemical composition on the ^{36}Cl production rate resulting in buried scarp rocks (for a constant geomagnetic field; other parameters indicated on figure). Colluvial wedge composition is approximated as fault scarp rock mean composition (continuous line), as mean colluvium pebbles composition (dotted line), and as mean soil composition (dashed line). See Table 2 for corresponding chemical compositions, and Fig. 15 for location of the colluvial wedge samples.

Four models have been proposed recently to account for the effects of the time variability of the geomagnetic field on cosmogenic nuclide production rates. All these models quantify the effective vertical cut-off rigidity R_c, that is the energy required for primary cosmic rays to penetrate the geomagnetic field and interact with the atmosphere at a given location. Details on the equations of each model can be found in Supplement 4.

Based on the description of the polar wander and on the local records of inclination provided by Ohno and Hamano (1993), Dunai (2001) developed a model appropriate for the 0–10 ka period. In that model, R_c is scaled to the geomagnetic latitude and field intensity, and allows the flux of cosmic rays that penetrates the Earth's magnetic field at a site to be calculated. This flux is used to derive the time variation (calculated using a 100 yr time steps) of the two scaling factors $S_{el,s}$ and $S_{el,\mu-}$ for neutrons and muons respectively. For older periods (>10 ka), Dunai (2001) approximates the geomagnetic field by a dipole, and R_c is calculated both using the equation of Elsasser *et al.* (1956; site longitude not taken into

© 2010 The Authors, *GJI*, **182,** 36–72
Journal compilation © 2010 RAS

Downloaded from https://academic.oup.com/gji/article-abstract/182/1/36/562733 by guest on 01 February 2019

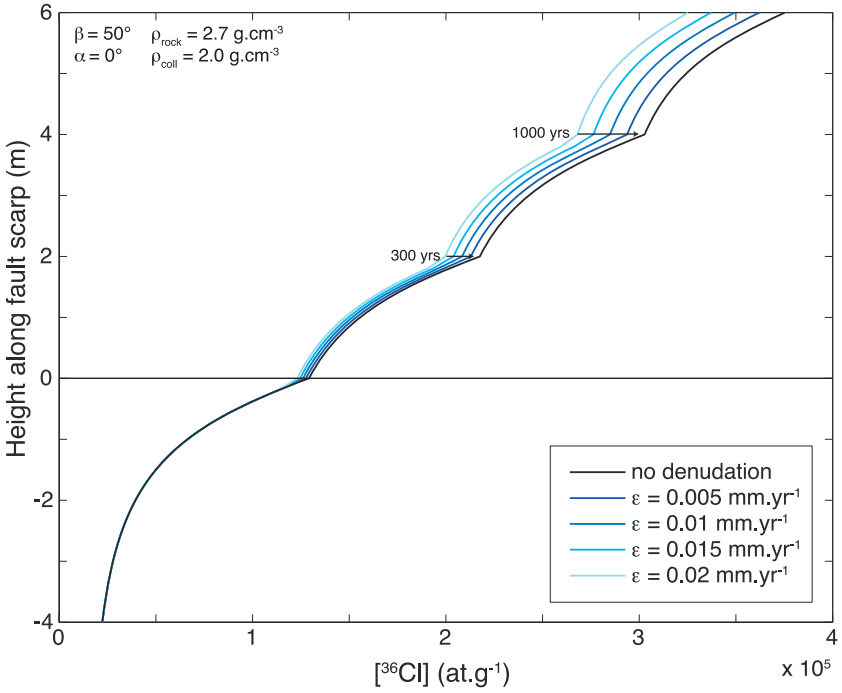

Figure 8. Effect of denudation on the [^{36}Cl] profile resulting in exposed scarp rocks. A reference curve is calculated for no denudation and 3 similar (2 m of on-fault slip), regular (every 2 kyr) earthquake exhumations. Ages are maximum age differences that are derived between the most extreme curves.

account), and the time variable dipole moment record by Yang *et al.* (2000) and Guyodo & Valet (1999).

Pigati & Lifton (2004) developed another model based on the description of the field palaeo-intensity provided by Yang *et al.* (2000; for 0–11 ka) and Guyodo & Valet (1999; >11 ka), and of the polar wander (Champion, 1980; Merrill and McElhinny, 1983; Ohno & Hamano 1993). R_c is calculated following the equation of Desilets & Zreda (2003). Note that replacing this later equation by the most recent of Desilets *et al.* (2006b; new fitting parameters for spallation) would improve the Pigati & Lifton (2004) model, as we do in the following.

Lifton *et al.* (2005) modified the Pigati & Lifton (2004) model by including a new relation between R_c, the geomagnetic latitude and the palaeointensity of the dipole. In addition, this model considers a solar modulation of the cosmic ray flux appropriate for the last 11.3 kyr (Solanki *et al.* 2004), since the solar magnetic field is strong enough to shield the galactic cosmic flux to various degrees over time.

More recently, Lifton *et al.* (2008) developed another model that includes geomagnetic field variations over the last 7 ka reported by Korte & Constable (2005a, b). In this model, R_c values are directly derived from Korte and Constable (2005a,b) model. The grid cell size is 5° latitude –15° longitude, while R_c is calculated in 500 yr time steps.

Fig. 9(a) presents the time variability of the scaling factors $S_{el,s}$ and $S_{el,\mu-}$ at our reference site that results from the use of the different models described above. The muon scaling factor $S_{el,\mu-}$ is fairly constant over time for all models considered, while it varies from one model to another (up to a factor of 1.5). The neutron scaling factor $S_{el,s}$ also varies from one model to the other (up to a factor of 1.5), but markedly varies in time for all models. The smoothness of the $S_{el,s}$ and $S_{el,\mu-}$ time curves for times older than 10 kyr results from the decreasing precision in the description of the geomagnetic field for those older time periods.

Fig. 9(b) presents synthetic [^{36}Cl] profiles calculated for a sequence of three similar earthquakes (Slip: 2m; Tr: 2 ka) for the case of a time varying geomagnetic field. The profiles are compared with that expected for the constant magnetic field model from Stone (2000). Note that the elementary production rate of ^{36}Cl from Ca-spallation at SLHL has been recalculated for each description of the geomagnetic field based on Stone *et al.* (1996) initial measurements (see figure caption for more details). The calculated ^{36}Cl concentrations are similar for all models, except the Dunai (2001) model. This may be explained by the differences in this model during the 0–11 kyr period and the constant scaling this model uses after 11 kyr relative to the other models. As an example, the largest difference between the Pigati and Lifton (2004) and the Stone (2000) concentrations is about 0.08×10^5 at g^{-1}, which would convert into a ∼200 yr difference in the age of the oldest earthquake. By contrast, the largest difference between the Dunai (2001) and the Stone (2000) concentrations is about 0.27×10^5 at g^{-1}, which would cause a >500 yr difference in the age of the three earthquakes. Thus, at our reference site, all models but that of Dunai (2001), produce similar [^{36}Cl] profiles, and so we conclude that the time variability of the geomagnetic field has a limited impact on the ^{36}Cl production rate. For simplicity, we use the constant field model of Stone (2000) in the following (Section 5).

4.6 Snow cover

Deep snow may shield the penetration of cosmic rays into the otherwise exposed rocks, and as such, modify the nuclide production rate in those rocks (e.g. Gosse & Phillips 2001). No information exists at present that would describe the past evolution of the snow depth over the Earth's surface. In the absence of such information, we are forced to estimate the potential impact of snow cover using the snow shielding formula provided by Gosse & Phillips (2001,

Downloaded from https://academic.oup.com/gji/article-abstract/182/1/36/562733 by guest on 01 February 2019

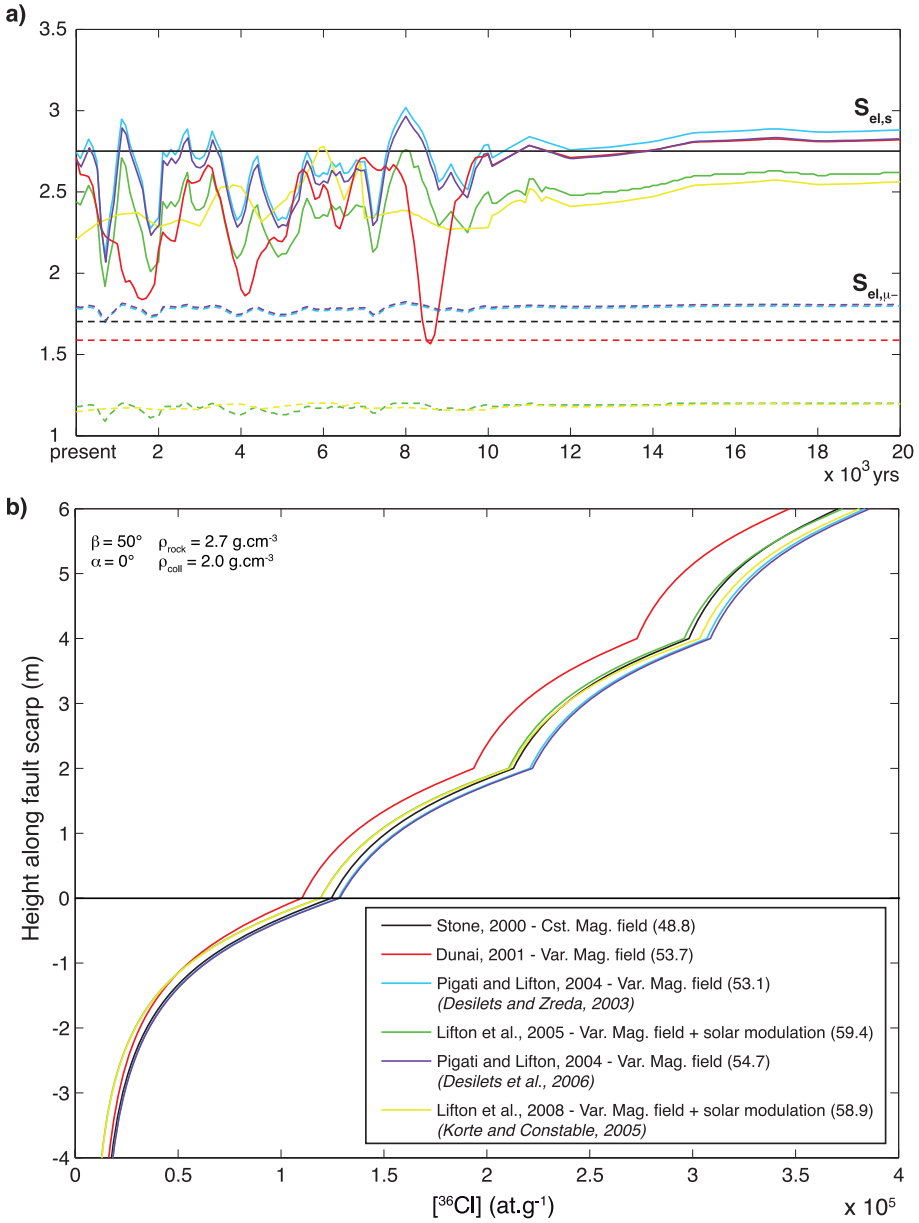

Figure 9. Effects of Earth's magnetic field time variability on ^{36}Cl production resulting in buried and exposed scarp rocks. The six geomagnetic field models listed at (b) bottom are considered. Values in brackets are Sea Level and High Latitude production rates of ^{36}Cl from Ca (atoms of ^{36}Cl per g of Ca per yr) derived from the Stone *et al.* (1996) value of 152 at. ^{36}Cl gr^{-1} Ca yr^{-1} (determined at Tabernacle Hill site over last 17.3 ka). New scaled values are 53.7 for Dunai (2001), 53.1 for Pigati & Lifton (2004; using Desilets & Zreda 2003), 59.4 for Lifton *et al.* (2005), 54.7 for Pigati & Lifton (2004; using Desilets *et al.* 2006) and 58.9 for Lifton *et al.* (2008). Elementary spallation production rates for K, Fe and Ti have not been re-calculated as our reference samples do not contain those elements. Concerning the Lifton *et al.* (2008) model, we have interpolated the provided R_c values in space and time, so that to obtain the R_c coefficients at our reference site for every 100 yr time-step over the 0–7 ka time interval. The resulting set of R_c values is then used as an input in the Lifton *et al.* (2005) Excel® spreadsheet. For older time periods, we have calculated R_c using the eq. (4) of Lifton *et al.* (2008). (a) Effects of geomagnetic field time variability on neutron ($S_{el,s}$) and muons ($S_{el,\mu-}$) scaling factors (from present to –20 kyr). (b) Effects of geomagnetic field time variability on [^{36}Cl] profiles in buried and exposed scarp rocks. A reference curve (constant field, Stone 2000) is calculated for three similar (2 m of on-fault slip), regular (every 2 kyr) earthquake exhumations.

see also Benson *et al.* 2004; Schildgen *et al.* 2005):

$$S_{\text{snow}} = \frac{1}{12}\sum_{i}^{12} e^{-[(Z_{\text{snow},i}-Z_{\text{sample}})\rho_{\text{snow},i}/\Lambda_{f,e}]}. \quad (3)$$

The shielding (S_{snow}) applies only when the sample is either below the colluvium or in the lowermost metres of the exhumed fault scarp. As an example, an average snow density of 0.3 g cm^{-3} (upper bound) and a snow thickness of 1 m covering the rocks during one, two, or six months of the year, produce shielding corrections of 0.9858, 0.9715 and 0.9145, respectively (Fig. 10). Compared with calculations performed without integrating any snow cover, the snow shielding appears to have significant effects when it lasts over long periods of time, at least 6 months per year. In such a case, the eventual ^{36}Cl concentrations may be slightly lowered

Downloaded from https://academic.oup.com/gji/article-abstract/182/1/36/562733 by guest on 01 February 2019

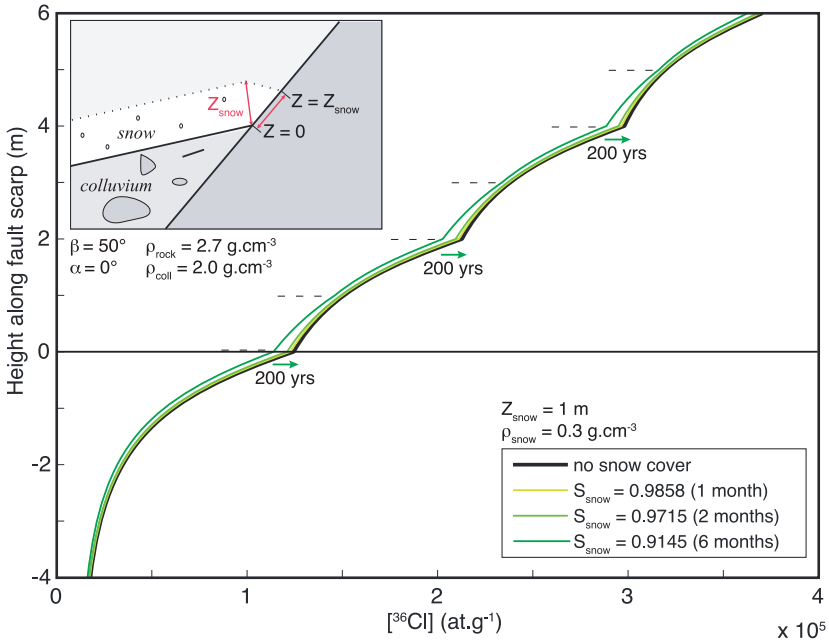

Figure 10. Effect of snow cover on the [^{36}Cl] profile resulting in buried and exposed scarp rocks. A reference curve (constant geomagnetic field) is calculated in the absence of snow cover for three similar (2 m of on-fault slip), regular (every 2 kyr) earthquake exhumations. An upper bound of snow density is taken to maximize the effect of snow shielding ($\rho_{\text{snow}} = 0.3$). Snow height (Z_{snow}) is 1 m. S_{snow} is the scaling factor related to snow cover. Ages are maximum age differences that result from the most extreme curves.

(-1×10^4 compared to the reference curve at 1×10^5 atoms of ^{36}Cl), resulting in an underestimation of earthquake ages by a minimum of 200 yr (Fig. 10).

5 RECOVERING SEISMIC HISTORIES FROM *IN SITU* ^{36}CL CONCENTRATION PROFILES: A SECOND STEP IN THE MODELLING

Modelling seismic exhumation histories requires consideration of the time-varying exposure history of the samples that results from episodic fault motion. Iterative calculations of the production rate are therefore required for each sample. We have built a numerical Matlab® code, named *modelscarp.m*, to automate these calculations. This code integrates the scaled production rates described in Sections 2 and 4 and quantifies model uncertainties. The model is fully described in Appendix B, and available as Supplement 1, where it can be downloaded.

The code presented here calculates the theoretical [^{36}Cl] profile that would result on the scarp given a slip exhumation scenario. Each scenario is parametrized by the number, the age and displacement of past earthquakes (or other slip events), and by the sample pre-exposure history. This theoretical profile is then compared to the measured profile to assess the likelihood of the tested earthquake scenario. The most likely earthquake scenario is identified by the minimum difference between the modelled and the measured concentration profiles associated with a positive Akaike test (see Section 5.2).

The model includes six subroutines. The firsts two are the *clrock.m* and *clcoll.m* codes described in Section 4, which compute the ^{36}Cl concentration in a sample over any period of exposure, for a given sample chemical composition and site characteristics. The main routine uses these first two to calculate the scarp's [^{36}Cl] profile as samples are progressively exhumed, cosmic ray flux changes over time and the surface is being eroded. To achieve this scenario, the main program uses four other subroutines: *scdepth.m,* which calculates the scaling at depth due to the colluvial wedge shielding of the fault plane (S_{depth}); *scsurf.m,* which calculates the scaling due to the shielding of the γ-dipping upper part of the scarp (S_{surf}); *scrock.m,* which calculates the cosmic ray flux attenuation in the rocks belonging to a β-dipping scarp, in the direction e perpendicular to the scarp surface (S_e); and *fitexp.m,* which calculates the fit of S, the scaling (S_{depth}, S_{surf}, S_e), by an exponential function of the form $S = s_o . \exp(-z/\Lambda)$ to calculate the attenuation length Λ (in the z direction considered: Z or e, see Figs A1 and A2).

Investigated samples resided below the colluvial wedge before the first recorded event moved them towards the surface. Initial abundance of ^{36}Cl in each sample is thus set by its pre-exposure history and setting (sample chemical composition, thickness and position on the scarp; site elevation, latitude, longitude, fault and colluvium geometry and density, denudation rate, Earth's magnetic field). Then, using the characteristics of each sample and the overall site conditions, the code calculates iteratively the amount of ^{36}Cl produced following the earthquake scenario that episodically exhumes the scarp. Time is divided into t year time steps over which production rate is assumed constant (usually 100 yr time steps). Supplementary details are provided in Appendix B.

Below we explore the sensitivity of the model results to the pre-exposure and exposure histories of the samples. In particular, we vary the initial [^{36}Cl] and the number, age, and displacement of the slip events.

In the following, all theoretical profiles are calculated using the elevation, latitude, longitude, chemical composition and colluvium density (Tables 1 and 2) of the Magnola fault site. Scarp and colluvial wedge dips were set to different values from those of the Magnola fault site to make the synthetic [^{36}Cl] profiles have sharper sections appearing more clearly on the figures. A synthetic reference profile is shown that results from an exhumation scenario consisting of three large earthquakes that occurred 6, 4 and 2 kyr ago, and each of which produced 2 m of along-fault displacement. This reference

Downloaded from https://academic.oup.com/gji/article-abstract/182/1/36/562733 by guest on 01 February 2019

profile is assigned a ±5 per cent uncertainty that represents the maximum analytical errors on the [^{36}Cl] measurements.

5.1 Dependence of the theoretical concentration profile on the exposure history

Effects of [^{36}Cl] prior to faulting (pre-exposure history)

The initial abundance of ^{36}Cl in each sample is set by the pre-exposure history of the highest samples analysed on the scarp. Two aspects of their pre-exposure history are especially important—the duration of prior exposure and their position at depth during that period. Because denudation becomes important on the upper section of the scarp (above the sampled profile), only theoretical [^{36}Cl] profiles can be used to assess the effect of this prior exposure.

The simplest case arises when the position of the samples does not change during their pre-exposure phase (i.e. the fault does not slip). In this case, [^{36}Cl] decreases exponentially with depth, and increases with the duration of prior exposure. As shown in Fig. 11(a), prior exposure has a strong influence on the [^{36}Cl] depth profile. For instance, a 2 kyr difference in prior exposure duration yields a doubling of the [^{36}Cl] in the uppermost samples. Furthermore, as slip events repeat on the fault and expose the previously buried samples, the initial difference leads to a persisting pronounced divergence between the resulting concentration profiles. In the example given in Fig. 11, the 2 kyr difference in the pre-exposure duration leads, after 6 ka of scarp exhumation, to [^{36}Cl] differing by 5–25 per cent as for the lowest and the highest exposed samples, respectively. Differences in ^{36}Cl concentrations of the lowest samples may be on the order of analytical uncertainties, but may become more important at higher scarp locations. On the other hand, it is likely that earthquakes have occurred prior to the exposure of the samples under analysis. This causes buried samples to move towards the surface progressively during their pre-exposure phase. Fig. 12 compares the effect of a simple (no earthquake) versus a complex (several earthquakes) pre-exposure history on the [^{36}Cl] profile that would eventually result from three similar, regular earthquake events. It shows that a pre-exposure history including three 2-m slip earthquakes having occurred at 8.5, 11 and 13.5 ka, reproduces the observed [^{36}Cl] profile as well as would a simple, shorter pre-exposure history including no earthquakes. Thus, it is impossible from the observation of a [^{36}Cl] profile alone to determine the details of pre-exposure history of the samples. Though only marginally resolvable, we found that a systematic younging of modelled earthquake ages results when using a complex pre-exposure history relative to ages inferred using a simple pre-exposure history.

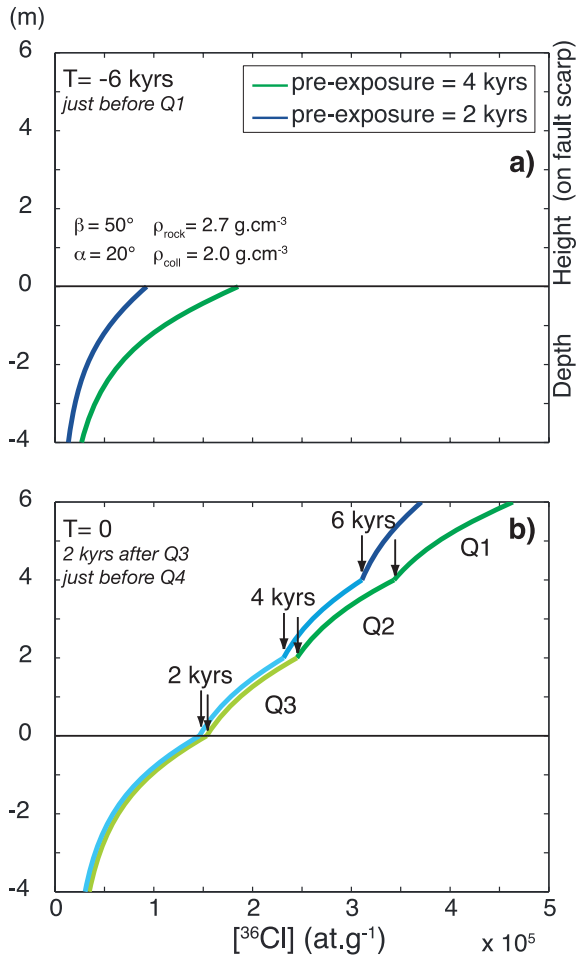

Figure 11. Effect of the pre-exposure duration on the [^{36}Cl] profile resulting in buried and exposed scarp rocks. The curves are calculated for three similar (2 m of on-fault slip), regular (every 2 kyr) earthquake exhumations (constant geomagnetic field). Other parameters are indicated on the figure. Pre-exposure duration affects the entire ^{36}Cl concentration profile, hence the recovered ages.

Effects of the exhumation process(es)

A normal fault scarp may be exhumed by the action of discrete earthquakes, aseismic creep, or of a combination thereof. Creep leads to the progressive exhumation of the scarp, which translates, as shown in Fig. 13(a), into a roughly linear concentration profile. Such a linear profile differs markedly from the piecewise arcuate shape that results from successive earthquake exhumations (grey line in Fig. 13a). This difference should allow an assessment of dominant slip processes that created a [^{36}Cl] profile. Yet, if scarp has been exhumed through the combination of earthquakes and creep, the creep part of the signal, unless clearly dominant, will not be recoverable. This implies that any recovered earthquake displacement represents a maximum bound.

Effects of the earthquake number variability

Since any large earthquake is expected to exhume a new section of the scarp, the number of earthquakes that contributed to the exhumation of the entire scarp controls the shape of the resulting [^{36}Cl] profile. Fig. 13(b) compares two different single rupture scenarios with our reference profile, one fitting the top and bottom part of the reference profile, the other fitting the entire profile. Scarps produced by single versus multiple events are clearly revealed in the ^{36}Cl profile. Both single-event profiles fail to fit the reference profile adequately.

Recovering the number of earthquakes recorded by the scarp relies on identifying distinct segments within the entire [^{36}Cl] profile. Our reference example shows that large earthquakes separated by long recurrence times should be easy to identify as each produces a marked exponential segment separated by clear discontinuities within the entire profile (Figs 2 and 11). As recurrence times decrease, individual earthquakes would become more difficult to discern in the resulting [^{36}Cl] profiles and would ultimately approach the case of continuous creep. In addition, clustered earthquakes such as two smaller size earthquakes (1 m of displacement each)

Downloaded from https://academic.oup.com/gji/article-abstract/182/1/36/562733 by guest on 01 February 2019

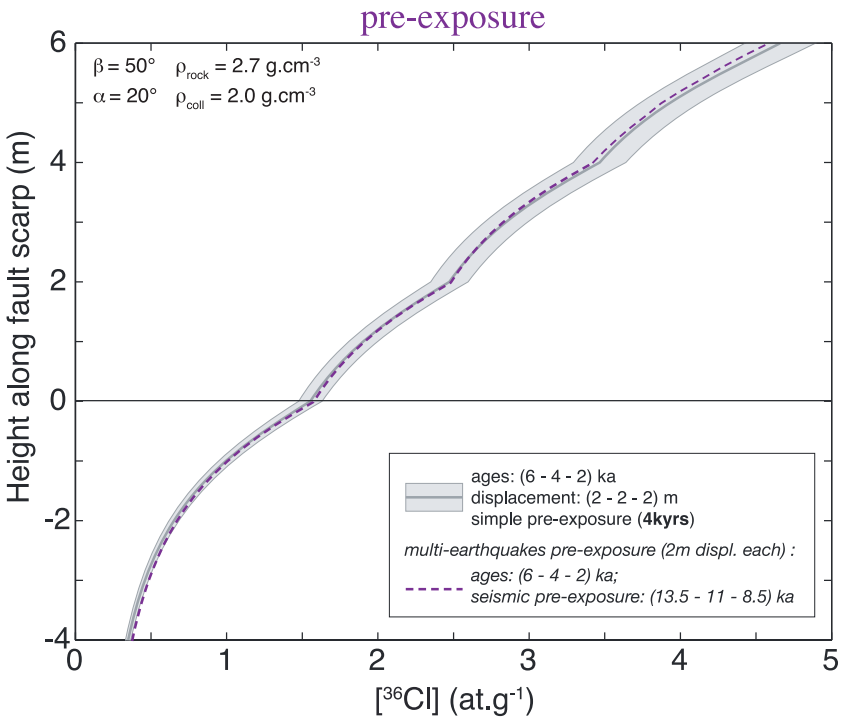

Figure 12. Effect of pre-exposure history on the [^{36}Cl] profile resulting in buried and exposed scarp rocks. The curves are calculated for three similar (2 m of on-fault slip), regular (every 2 kyr) earthquake exhumations (constant geomagnetic field) as green curve on Fig. 11(b). The grey band represents the ±5 per cent analytical uncertainty. The pre-exposure phase is made to include zero ('simple' pre-exposure) to several slip events.

having occurred in succession over a 2 kyr time span, combine to produce a [^{36}Cl] pattern indistinguishable from that resulting from a single larger earthquake (2 m of displacement; Fig. 14a). Thus, the number of earthquakes recovered through a [^{36}Cl] study is always a minimum value, while the associated displacements provide maximum bounds. In the rest of the section, we continue to use the term 'earthquake' when interpreting a major segment in a [^{36}Cl] profile, although we acknowledge that those events could represent a series of temporally clustered earthquake ruptures.

Effects of earthquake age variability

Because samples still buried under the colluvium accumulate ^{36}Cl before the earthquake that exhumes them, the composite earthquake history controls the overall shape of the concentration profile, including each of the segments that constitute the profile. However, because of uncertainties associated with the concentration measurements and modelling, only large age differences can be discriminated. As an example, Fig. 14(b) shows that, for the reference parameters chosen, a difference of ±0.5 kyr in a single earthquake age yields a variation in the resulting [^{36}Cl] profile on the order of the 5 per cent uncertainty on the AMS measurements. Thus, such a ±0.5 kyr age difference is generally not detectable.

Effects of earthquake displacement variability

Displacement values attributed to each of the earthquakes recorded in a scarp also control the overall shape of the concentration profile. As an example, a difference of at least ±20 cm in a single earthquake displacement is required to produce a significant variation in the resulting [^{36}Cl] profile, beyond the 5 per cent uncertainty on the AMS measurements (Fig. 14c).

5.2 Searching for the most realistic exhumation history

Because the ^{36}Cl calculations depend on a large number of parameters, several scenarios can be found that roughly fit the data. To search which of those models are more robust we combine different statistical methods.

The first indicator that we use is the weighted root mean square (RMSw), which allows quantifying the fit between modelled and measured concentrations while taking into account the uncertainties on the measurements. The RMSw is calculated as follows:

$$RMSw = \sqrt{\sum_{i=1}^{n}\left[\left(\frac{{}_i{}^{36}\mathrm{Cl}_{\mathrm{measured}} - {}_i{}^{36}\mathrm{Cl}_{\mathrm{model}}}{{}_i\sigma\,{}^{36}\mathrm{Cl}_{\mathrm{measured}}}\right)^2\right]/n}, \quad (3)$$

here $^{36}\mathrm{Cl}_{\mathrm{measured}}$ is the measured AMS concentration in ^{36}Cl, $^{36}\mathrm{Cl}_{\mathrm{model}}$ is the modelled concentration in ^{36}Cl, $\sigma\,^{36}\mathrm{Cl}_{\mathrm{measured}}$ is the uncertainty on the AMS measured ^{36}Cl concentration, and n is the number of measurements.

The second indicator that we may use is the reduced Chi-square (χ^2_{red}) given by:

$$\chi^2_{\mathrm{red}} = \frac{1}{n-k-1}\sum\left[\left(\frac{{}^{36}\mathrm{Cl}_{\mathrm{measured}} - {}^{36}\mathrm{Cl}_{\mathrm{model}}}{\sigma\,{}^{36}\mathrm{Cl}_{\mathrm{measured}}}\right)^2\right], \quad (4)$$

where n is the number of measurements and k the number of parameters included in the model. The parameters generally included in the model are: the number N of earthquakes (N parameters), the N displacement values associated to the N earthquakes (N parameters), the pre-exposure duration (1 parameter), the denudation rate (1 parameter), and the data variance (1 parameter): $k = 2N + 3$. The χ^2_{red} allows the balance between the model improvement and the number of free parameters that contribute to that improvement (increasing the number of free parameters always improves the fit) to be determined for the χ^2_{red} value the closest to 1.

Downloaded from https://academic.oup.com/gji/article-abstract/182/1/36/562733 by guest on 01 February 2019

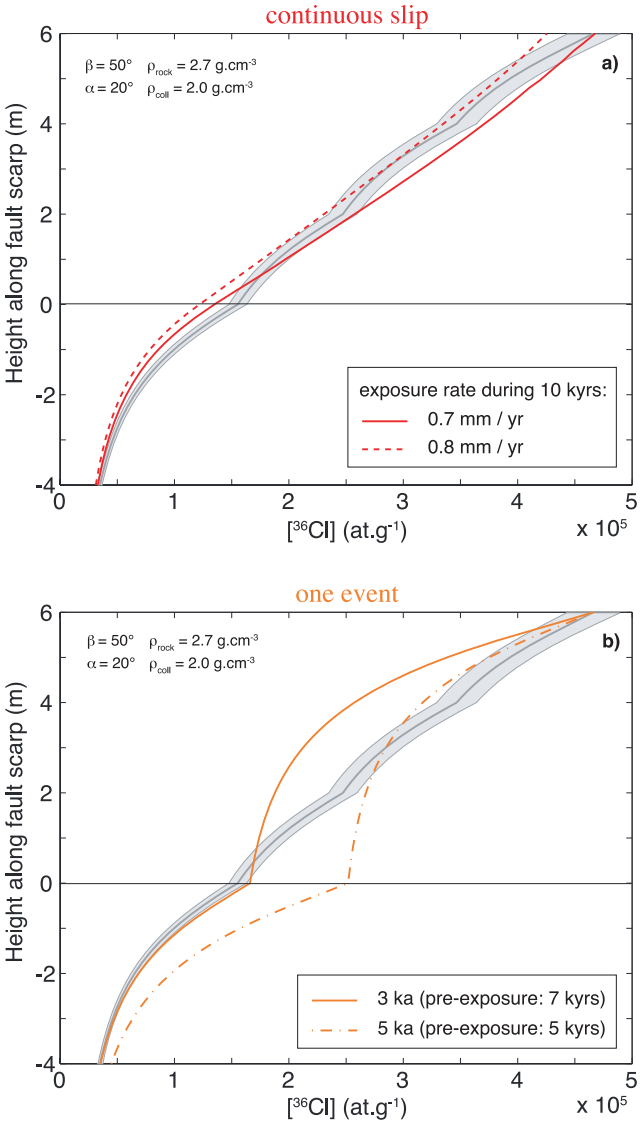

Figure 13. Effect of the exhumation process on the [^{36}Cl] profile resulting in buried and exposed scarp rocks. Same reference curve as Fig. 12. (a) Continuous exhumation (creep) at variable rate. (b) Exhumation by a single large event at various times, as is the case for gravitational collapse.

Finally, we also use the Akaike Information Criterion (Akaike 1974):

$$AIC = n \log \left[\sum_n \left(\left({}^{36}\mathrm{Cl}_{\mathrm{measured}} - {}^{36}\mathrm{Cl}_{\mathrm{model}} \right)^2 \right) / n \right] + 2k, \qquad (5)$$

where the parameters are defined as before.

When the ratio of the data number n to the number of free parameters k is small ($\leq$40, Burnham & Anderson 2002), a more sophisticated version of the AIC criterion, named AICc, must be used:

$$AICc = AIC + \frac{2k(k+1)}{n-k-1}; AICc = n \log \left[\sum_n \left(\left({}^{36}\mathrm{Cl}_{\mathrm{measured}} - {}^{36}\mathrm{Cl}_{\mathrm{model}} \right)^2 \right) / n \right] + \frac{2kn}{n-k-1} \qquad (6)$$

In a population of models, the most robust is the one having the lowest AICc value. Any other model is then ranked according to

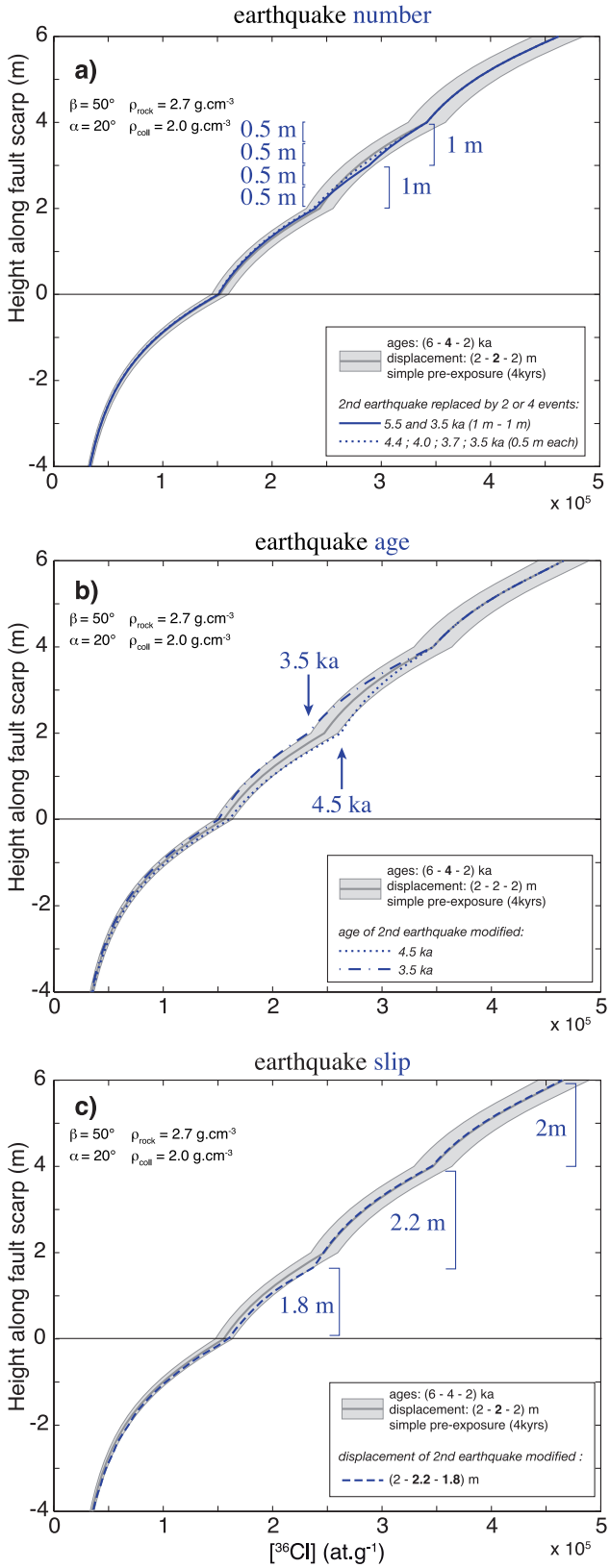

Figure 14. Effect of the variability in the earthquake number, age and slip on the ^{36}Cl production rates resulting in buried and exposed scarp rocks. Same reference curve as Fig. 12. (a) Each single large slip event may be a multiple event including several smaller events; small earthquakes cannot be discriminated. (b) Age differences lower than ~0.5 kyr cannot be discriminated. (c) Slip differences lower than ~0.2 m cannot be discriminated.

Downloaded from https://academic.oup.com/gji/article-abstract/182/1/36/562733 by guest on 01 February 2019

the difference Δ between its own AICc value and this minimum. Models with $0 \leq \Delta \leq 2$ are reasonably well supported by the data, models with $4 \leq \Delta \leq 7$ are less supported by the data yet still plausible, while models with $10 \leq \Delta$ are not supported by the data and should be discarded (Burnham & Anderson 2002).

5.3 Applying the new model to [^{36}Cl] measurements: revisiting the seismic history of the Magnola fault, Central Italy

Data and site characteristics

We tested our code on a data set from the Magnola Holocene normal fault scarp (Palumbo *et al.* 2004, Central Apennines, Italy, Fig. 1). This fault is part of a larger active normal fault system that ruptured in several large earthquakes over the last few thousands of years (e.g. Galli *et al.* 2008 and references therein). The last major event on this system was the 1915 $M_w \sim$7.0 Avezzano earthquake, 10 km away from the Magnola fault. Palumbo *et al.* (2004; referred to as P04 in the following) collected 65 samples along a vertical transect on the Magnola Holocene scarp, and analyzed their ^{36}Cl content. Modelling of the ^{36}Cl data revealed that the Magnola fault had ruptured in 4–6 earthquakes over the Holocene. The preferred model of five earthquakes yielded ages of 12.0, 10.5, 7.4, 6.7 and 4.8 ka, each producing along-fault displacements between 1.5 and 2.7 m.

^{36}Cl and Cl_{nat} AMS measurements from P04 were reprocessed following the protocol described in Section 3.3 for chemistry-blank corrections. The concentrations we obtain are ∼2.5 per cent lower overall than the values initially proposed by P04 (Table 3, samples named 'MAG'). It is worth noting that P04 crushed the samples together with the crystallized calcite veins, which may explain part of the scatter observed in the data (Table 4).

We performed additional sampling at this site, to determine the ^{36}Cl content of the scarp rocks buried below the colluvial wedge. We excavated a 4-m-along fault deep trench at the base of the fault scarp and continuously sampled the scarp rocks exposed in the trench (Fig. 15a, samples 'MA3c' in Table 3). The chemical preparation of these 42 samples was carried out at CEREGE, France, following the procedure described in Section 3.2. Half of the chemically prepared samples (one sample every 20 cm; Table 3) were measured at the AMS facility of the Lawrence Livermore National Laboratory, California. The whole rock chemical analyses of the samples were performed at the SARM facility of Nancy, France.

Fig. 16(a) shows [^{36}Cl] as a function of the scarp height; [^{36}Cl], [Cl_{nat}] and chemical analyses results are reported in Tables 2 and 3. Concentrations of the only two significant target elements in the Magnola rocks, Ca and ^{35}Cl, are defined with a ±2 and ±5 per cent accuracy, respectively. The mean rock density is 2.7 ± 0.01 (Table 1).

The trench excavation also allowed us to study the geometry of the colluvial wedge and sample it (Fig. 15b). The wedge surface dips by 30 ± 3° (α, Table 1) and exhibits a layered structure that contains pebbles of limestone whose number decreases with depth. We collected two charcoal samples in the wedge (C1 and C2 in Fig. 15b), whose ^{14}C dating (Poznan Radiocarbon laboratory, Poland) yielded ages of 31.6 ± 0.5 and 38.8 ± 1.2 ka BP, respectively. These ages suggest that the upper part of the Magnola colluvial wedge has been deposited during the Pleistocene, as had been suggested before (Armijo *et al.* 1992; Benedetti *et al.* 2002). This shows that the colluvium surface may be taken as a reference from which to measure the coseismic displacements. However, this does not preclude that the Magnola colluvial wedge also includes more recent material (likely less than 50 cm thick).

We also analysed the density and composition of the colluvial wedge as described in Sections 3.4 and 3.5. The density is 1.5 ± 0.1. The mean chemical composition is given in Table 2.

The fault scarp dips by 45 ± 2° (β) over ∼20 m height (H); the scarp then shallows in its upper section where $\gamma = 30 \pm 5°$ (Piccardi *et al.* 1999). No significant topography around the horizon shields the scarp. The elevation of the site is 1255 ± 5 m a.s.l. (Table 1).

The well-preserved surface of the Magnola Holocene scarp suggests that denudation has been slow. The same conclusion was reached by Carcaillet *et al.* (2008) who showed that the Magnola scarp rocks are overlain by a surface coating of aluminum-rich silicates and iron-sulphides that likely prevents significant weathering. We thus expect no, or very low denudation at our site.

Presently, the basal part of the scarp is covered by snow for no more than 1 month yr^{-1}. If we assume that the snowfall has not significantly changed over the last 10 kyr, we expect snow shielding to have a negligible effect on the modelled ^{36}Cl concentrations (Section 4.6 and Fig. 10).

Defining the range of the most likely seismic scenarios

^{36}Cl concentrations are plotted as a function of scarp height in Fig. 16(a). The overall shape is convex upward, but subsections show distinct discontinuities consistent with repeated fault slip. Based on our sensitivity analysis, it is likely that different exhumation scenarios can be found that could reasonably reproduce the measured profile. To limit the number of scenarios considered, we estimate the minimum number of major slip events recorded in the data. These estimates are then further refined to determine most likely scenarios.

First, we identify four major discontinuities in the profile by visual inspection of Fig. 16(a), noted by the green arrows. This initial interpretation is supported by the stacking of individual probability density functions (Pdf, assumed to be Gaussian) of sample concentration (Lowell 1995; Culler *et al.* 2000, Fig. 16b). This process reveals zones of the profile that have the highest density of similar concentration values. As the samples were taken at roughly constant intervals, these zones of higher density are expected to coincide with the major discontinuities in the [^{36}Cl] profile. When applied to our dataset, four major discontinuities are revealed (green circles), at about 1.8–2.1, 2.6, 4.0 and 4.5 .10^5 atoms of ^{36}Cl per gram of rock (Fig. 16b). It is noteworthy that those four peaks roughly coincide with those visually identified. Two more subtle peaks (bumps) are suggested at 2.3 and 3.2–3.4 × 10^5 at g^{-1} of ^{36}Cl. This suggests that four to six large slip events contribute to the shaping of the measured [^{36}Cl] profile. That range of earthquake number and the position of the major discontinuities is similar to those suggested previously by P04.

Searching for the most realistic exhumation scenario

Having determined the most likely range of the number of large earthquakes to have contributed to the scarp exhumation, a second step uses these constraints to estimate the seismic history that best matches the observed [^{36}Cl] profile. In the following, we model the data using the mean value of each input Magnola parameter (Tables 1–3) that is, by ignoring their associated uncertainties. Uncertainties are included in a following step (next section), once the preferred scenario has been defined.

Downloaded from https://academic.oup.com/gji/article-abstract/182/1/36/562733 by guest on 01 February 2019

Table 3. Concentrations in ^{36}Cl, thickness and position on the scarp of the Magnola samples. Samples 'MA3c' are from the buried part of the scarp, while 'MAG' are exposed samples (Palumbo *et al.* 2004), whose [^{36}Cl] and [Cl] concentrations were reprocessed according to the protocol described in Section 3.3 and Supplement 3 for blank corrections. MA3c-XXmean indicates average of two replicates (see Supplement 5). Calcium concentrations were determined at ICP on all MA3c samples, while only on five MAG samples. We use the average $[Ca]_{MAG} = 3.896E + 05$ for all the MAG samples. Note that sample heights given by Palumbo *et al.* (2004) coincide with the bottom parts of the samples, while sample heights used here correspond to the middle part of the samples. This explains the 5 cm difference between the two datasets. Mean uncertainties on $[Cl_{nat}]$ concentrations are 2 per cent, and maximum uncertainties are 5 per cent. Mean uncertainties on $[Ca]_{ICP}$ are 2 per cent.

	61	62	63	64	65	66
Sample Name	$[Cl]nat_{AMS}$ (ppm)	$[Ca]_{ICP}$ (ppm)	Height on fault scarp (cm)	Sample thickness (cm)	$[^{36}Cl]_{AMS}$ (at.g^{-1} of rock)	$[^{36}Cl]_{AMS}$ uncertainty
MAG 01	12	3.896E + 05	1015	1.6	4.60E + 05	1.70E + 04
MAG 02	11.9	3.896E + 05	1005	2.1	4.59E + 05	1.69E + 04
MAG 04	14.9	3.896E + 05	986	2.2	4.51E + 05	1.12E + 04
MAG 05	12.2	3.896E + 05	975	2.4	4.38E + 05	1.33E + 04
MAG 06	13.7	3.896E + 05	965	2.3	4.49E + 05	1.38E + 04
MAG 07	14.6	3.896E + 05	955	1.7	4.49E + 05	1.64E + 04
MAG 10	19.1	3.896E + 05	925	2.6	4.51E + 05	1.64E + 04
MAG 11	16.7	3.896E + 05	915	2.2	4.40E + 05	1.56E + 04
MAG 13	19.2	3.896E + 05	890	2.5	4.45E + 05	1.19E + 04
MAG 14	17.3	3.896E + 05	880	2.6	4.27E + 05	1.55E + 04
MAG 24	18.7	3.896E + 05	850	2.2	4.24E + 05	8.89E + 03
MAG 25	17.2	3.896E + 05	840	2.5	4.05E + 05	1.33E + 04
MAG 26	16.3	3.896E + 05	830	2.2	4.11E + 05	1.53E + 04
MAG 27	20	3.896E + 05	820	2.1	3.98E + 05	1.53E + 04
MAG 28	20.8	3.896E + 05	809	1.9	3.95E + 05	7.96E + 03
MAG 29	20.3	3.896E + 05	799	2.5	3.96E + 05	1.46E + 04
MAG 31	16.6	3.896E + 05	779	2.5	4.08E + 05	1.73E + 04
MAG 33	19.5	3.896E + 05	760	2.3	3.94E + 05	1.92E + 04
MAG 35	22.3	3.896E + 05	739	3	4.05E + 05	1.48E + 04
MAG 37	22.6	3.896E + 05	719	3.3	3.89E + 05	1.42E + 04
MAG 39	17.5	3.896E + 05	700	3.3	3.62E + 05	7.37E + 03
MAG 41	7.4	3.896E + 05	680	1.8	3.42E + 05	1.04E + 04
MAG 43	6.6	3.896E + 05	660	2.3	3.43E + 05	1.46E + 04
MAG 45	6.6	3.896E + 05	641	2	3.55E + 05	1.72E + 04
MAG 66	7.4	3.896E + 05	620	3.8	3.20E + 05	1.38E + 04
MAG 67	7.1	3.896E + 05	610	3.5	3.38E + 05	1.25E + 04
MAG 69	8.8	3.896E + 05	590	2.2	3.18E + 05	1.18E + 04
MAG 70	8.7	3.896E + 05	579	2.7	3.32E + 05	1.21E + 04
MAG 72	9.4	3.896E + 05	559	2.5	3.07E + 05	1.59E + 04
MAG 73	10	3.896E + 05	550	2.2	3.16E + 05	5.90E + 03
MAG 75	10.5	3.896E + 05	530	2.3	2.89E + 05	1.29E + 04
MAG 76	10.9	3.896E + 05	520	1.9	2.93E + 05	8.82E + 03
MAG 77	8.8	3.896E + 05	509	2.1	2.97E + 05	1.08E + 04
MAG 78	5.6	3.896E + 05	499	1.6	2.81E + 05	1.04E + 04
MAG 80	3	3.896E + 05	479	2.6	2.83E + 05	6.19E + 03
MAG 82	3.5	3.896E + 05	460	2.7	2.74E + 05	1.00E + 04
MAG 83	6.4	3.896E + 05	450	2.3	2.93E + 05	9.72E + 03
MAG 84	9.9	3.896E + 05	440	2.2	2.59E + 05	1.00E + 04
MAG 85	8.4	3.896E + 05	430	2.3	2.64E + 05	5.02E + 03
MAG 86	8.6	3.896E + 05	419	2.3	2.65E + 05	1.39E + 04
MAG 88	14	3.896E + 05	399	1.5	2.71E + 05	5.57E + 03
MAG 89	14.2	3.896E + 05	392	1.3	2.66E + 05	9.70E + 03
MAG 90	10.6	3.896E + 05	388	2.2	2.75E + 05	1.02E + 04
MAG 91	11.7	3.896E + 05	378	2.2	2.63E + 05	9.63E + 03
MAG 92	12.7	3.896E + 05	368	1.7	2.69E + 05	9.92E + 03
MAG 93	13.3	3.896E + 05	358	1.7	2.72E + 05	6.38E + 03
MAG 15	7.9	3.896E + 05	289	2	2.61E + 05	1.22E + 04
MAG 16	8.3	3.896E + 05	280	2.2	2.41E + 05	3.86E + 03
MAG 17	9	3.896E + 05	270	2	2.57E + 05	8.33E + 03
MAG 18	12	3.896E + 05	260	2.1	2.68E + 05	9.74E + 03
MAG 19	9.9	3.896E + 05	250	2.6	2.54E + 05	9.29E + 03
MAG 20	14.7	3.896E + 05	239	3.2	2.65E + 05	9.15E + 03
MAG 21	10.5	3.896E + 05	230	2.2	2.52E + 05	9.27E + 03
MAG 47	11.1	3.896E + 05	219	1.7	2.48E + 05	1.15E + 04
MAG 49	10.7	3.896E + 05	200	1.7	2.42E + 05	1.05E + 04
MAG 50	11.3	3.896E + 05	192	1.5	2.32E + 05	8.43E + 03
MAG 52	11.2	3.896E + 05	171	1.6	2.29E + 05	3.43E + 03
MAG 53	9.3	3.896E + 05	161	1.7	2.46E + 05	7.43E + 03

Downloaded from https://academic.oup.com/gji/article-abstract/182/1/36/562733 by guest on 01 February 2019

Table 3. (*Continued.*)

Sample Name	61 $[Cl]nat_{AMS}$ (ppm)	62 $[Ca]_{ICP}$ (ppm)	63 Height on fault scarp (cm)	64 Sample thickness (cm)	65 $[^{36}Cl]_{AMS}$ (at.g^{-1} of rock)	66 $[^{36}Cl]_{AMS}$ uncertainty
MAG 55	7.8	3.896E + 05	136	1.7	2.28E + 05	8.32E + 03
MAG 57	6.6	3.896E + 05	116	1.3	2.11E + 05	1.26E + 04
MAG 58	6.6	3.896E + 05	106	2.2	2.08E + 05	1.16E + 04
MAG 60	7.9	3.896E + 05	86	2.5	2.05E + 05	1.19E + 04
MAG 62	8.5	3.896E + 05	66	2.7	2.01E + 05	6.97E + 03
MAG 63	7	3.896E + 05	56	2.7	2.08E + 05	8.00E + 03
MAG 65A	9.7	3.896E + 05	33	3	2.21E + 05	7.11E + 03
MA3c 01	11.2	3.931E + 05	15	3	1.79E + 05	4.28E + 03
MA3c 02	12.1	3.946E + 05	5	3	1.70E + 05	9.33E + 03
MA3c 03	11.6	4.077E + 05	-5	3	1.77E + 05	4.36E + 03
MA3c 04	11.3	3.943E + 05	-15	3	2.13E + 05	5.05E + 03
MA3c 05	10.9	3.959E + 05	-25	3	1.65E + 05	4.07E + 03
MA3c 06	12.3	4.034E + 05	-35	3	1.67E + 05	3.96E + 03
MA3c 08	11.2	3.979E + 05	-55	3	1.55E + 05	3.68E + 03
MA3c 10	10.3	3.933E + 05	-75	3	1.60E + 05	3.96E + 03
MA3c 12	10.8	3.867E + 05	-95	3	1.48E + 05	4.03E + 03
MA3c 13	12.4	3.947E + 05	-105	3	1.48E + 05	3.65E + 03
MA3c 14	11.7	3.865E + 05	-115	3	1.95E + 05	6.33E + 03
MA3c 15	12.8	4.065E + 05	-125	3	1.46E + 05	3.61E + 03
MA3c 16	11.3	3.856E + 05	-135	3	1.80E + 05	4.91E + 03
MA3c 17	11.9	3.874E + 05	-145	3	1.37E + 05	3.41E + 03
MA3c 18 mean	11.2	4.005E + 05	-155	3	1.43E + 05	2.79E + 03
MA3c 20	8.9	3.977E + 05	-175	3	1.32E + 05	5.59E + 03
MA3c 22	7	4.021E + 05	-195	3	1.26E + 05	2.98E + 03
MA3c 24	11.5	3.929E + 05	-215	3	1.30E + 05	3.09E + 03
MA3c 26	13.7	3.955E + 05	-235	3	1.25E + 05	5.06E + 03
MA3c 28 mean	13	4.082E + 05	-255	3	1.26E + 05	1.02E + 03
MA3c 30	8.1	3.953E + 05	-275	3	1.16E + 05	2.26E + 03
MA3c 32	11.2	3.883E + 05	-295	3	1.13E + 05	2.81E + 03
MA3c 34	9.8	3.923E + 05	-315	3	1.13E + 05	2.74E + 03
MA3c 36	9.9	4.022E + 05	-335	3	1.16E + 05	2.75E + 03
MA3c 38	8.6	3.990E + 05	-355	3	1.06E + 05	3.69E + 03
MA3c 40	8.3	3.953E + 05	-375	3	1.06E + 05	2.62E + 03
MA3c 42 mean	10.9	3.977E + 05	-395	3	1.05E + 05	3.64E + 03

Table 4. Comparison of *in situ* $[^{36}Cl]$ concentrations in calcite veins and in vein-free rocks. Per cent *v* stands for per cent in volume. Two Magnola samples (A and B) have been analysed, at different positions on the scarp. *R* stands for the number of replicates. All samples but A-a were chemically prepared and measured twice. Reported concentrations are mean values of replicates, with resulting uncertainties. In both studied cases, the calcite veins have lower $[^{36}Cl]$ concentrations than the vein-free rocks. This confirms that crystallized veins should be removed from the samples before crushing, since their 'history' may be different from that of the scarp rocks.

			R	$[^{36}Cl]$ (at.g^{-1} of rock)	$[^{36}Cl]$ uncertainty (at.g^{-1} of rock)	per cent	
Sample A	a	Veins only	*1*	1.18E + 05	3.92E + 03	3.3	A-a is 63 per cent lower than A-b
	b	Rock without veins	*2*	3.18E + 05	1.20E + 04	3.8	
Sample B	c	Whole rock : 3–5 per cent. *v* veins	*2*	2.79E + 05	1.15E + 04	4.1	B-c is 5 per cent lower than B-b
	b	Rock without veins	*2*	2.92E + 05	1.70E + 04	5.8	

The first parameter we explored was the prior exposure (*preexp* in the Matlab® code). Fig. 17 shows the ^{36}Cl production rate as a function of depth over 40 m along the buried fault scarp at the Magnola site. This confirms that significant amounts of ^{36}Cl may have been produced at depth prior to fault-related exhumation. The highest data points in the $[^{36}Cl]$ profile are those that potentially inherit the largest component from prior exposure. As shown in Fig. 16, the highest discontinuity in the profile (corresponding to a concentration of 4.5×10^5 atom of ^{36}Cl per g of rock) gives a rough idea of the age of the oldest event, while the shape of the profile above this discontinuity depends largely on the inherited component. Thus we first determined the pre-exposure histories that may have produced the observed $[^{36}Cl]$ profile in the upper section. The quality of the fit is estimated from the RMSw value (Section 5.2). The age and slip for the oldest event are also jointly estimated. Satisfying fits can be found for very different pre-exposure scenarios (Fig. 18), involving either simple (no earthquake) or complex (multievents) slip histories.

To ensure an appropriate fit of the upper data section, a pre-exposure duration ranging between 1.9 (+1.6/–1.1) (simple pre-exposure) and 5 kyr (complex pre-exposure) is required. These two extreme values yield an age for the oldest earthquake recorded on the scarp ranging between 6.2 and 8.0 kyr. Thus, while the modelling of the profile upper section does not constrain the pre-exposure history, it constrains the likely age range of the oldest recorded earthquake. Accordingly, for simplicity we model the rest of the

Downloaded from https://academic.oup.com/gji/article-abstract/182/1/36/562733 by guest on 01 February 2019

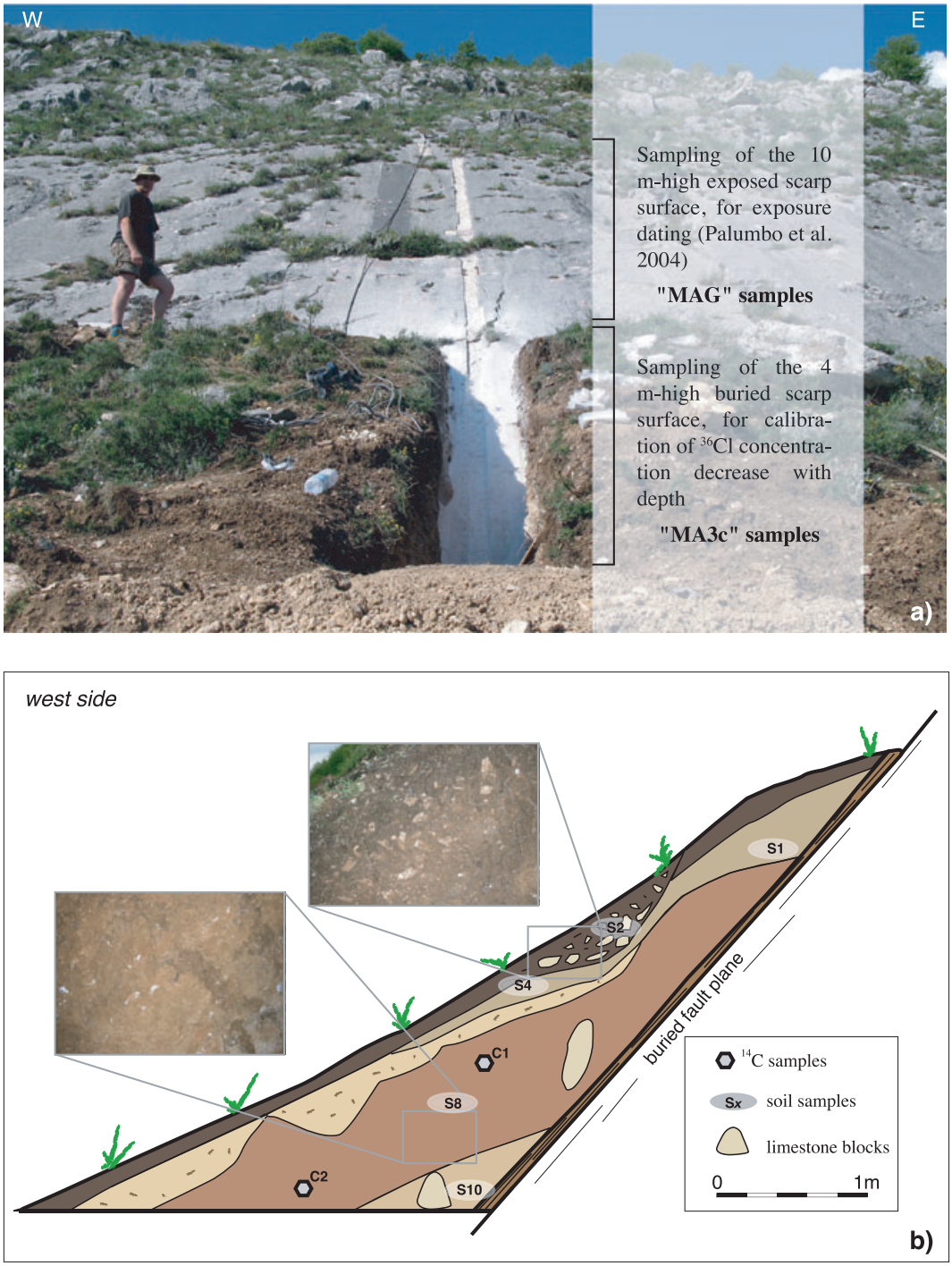

Figure 15. Magnola fault sampling site (Central Apennines, Italy). (a) The exposed scarp surface has been sampled by Palumbo *et al.* (2004; white vertical groove). We additionally sampled the buried part of the scarp, over 4 m of height. (b) Schematic representation of the colluvial wedge (west profile) and position of two ^{14}C samples (*Cx*) and five colluvium samples (*Sx*, see Supplement 6). The colluvial wedge is formed by layers of different colours, containing pebbles whose number decreases with depth. The upper dark brown part is a well-developed soil. The ^{14}C ages are: C1 = 31.6 ± 0.5 kyr BP and C2 = 38.8 ± 1.2 kyr BP.

data using the simple pre-exposure scenario (Fig. 18a; age of oldest earthquake: 7.2 ka). Using this best fit of the upper segment of the [^{36}Cl] profile, we model the next profile section down the scarp by adding an earthquake (Figs 19a and b). This process is repeated for each adjacent lower section until the entire profile is fit (Figs 19c and d). We have applied this approach to successively fit the entire dataset by 1–10 earthquakes.

Whatever the number of earthquakes chosen to model the data, the simple pre-exposure history precludes from finding a very good fit for the colluvium samples. As said above, with a simple pre-exposure scenario, the samples are at shallower depth than with a complex pre-exposure history. Applying a complex pre-exposure history to the modelling would allow a better fit of the colluvium samples since the vertical gradient in [^{36}Cl] would be weaker, thus

© 2010 The Authors, *GJI*, **182,** 36–72
Journal compilation © 2010 RAS

Downloaded from https://academic.oup.com/gji/article-abstract/182/1/36/562733 by guest on 01 February 2019

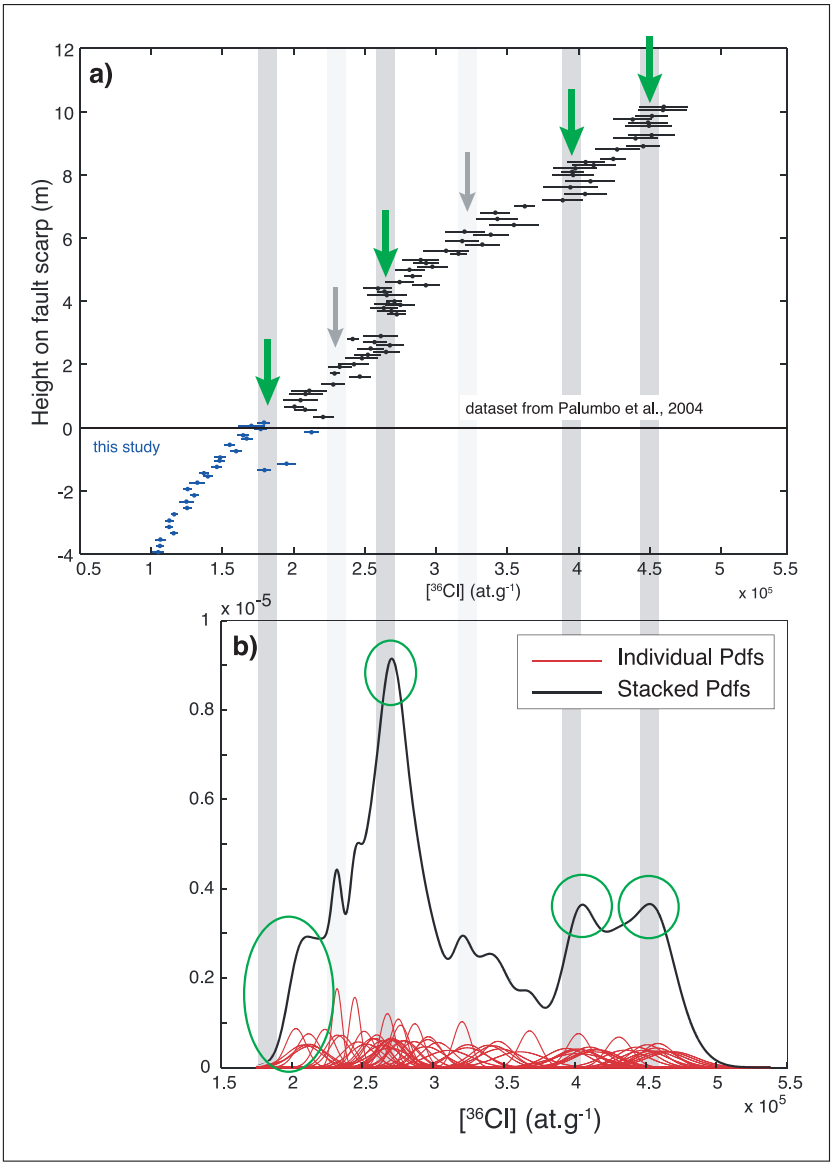

Figure 16. Analysis of the Magnola [^{36}Cl] versus scarp height. (a) [^{36}Cl] as a function of scarp height (positive where exposed, negative where buried). Data in black are from Palumbo *et al.* (2004). Note that we re-processed them for blank corrections (see text for details). Horizontal lines are 2σ AMS uncertainties. Data in blue are from present study, acquired in the buried part of the scarp. Green arrows indicate the major discontinuities that can be visually distinguished in the profile. Grey arrows suggest other, more subtle discontinuities. (b) Individual (red) and summed (black) Probability Density Functions (Pdfs). Four well-defined peaks appear in summed Pdfs (green circles), as two more subtle, that all coincide with the discontinuities defined in figure a (grey vertical bars, darker for clearer discontinuities).

giving a steeper slope in the [^{36}Cl] profile. This is indeed what we observe for the buried samples (e.g. Fig. 19d). However, as pre-exposure history is unknown, we prefer to model the dataset with a simple pre-exposure that in return includes less parameters; thus less sources of uncertainties.

Fig. 20 shows the corresponding RMSw, $\chi^2_{\rm red}$ and AICc parameters as a function of the imposed number of earthquakes (values in Table 5). These metrics require two to six large slip events to fit the entire profile. The AICc criterion shows that the three earthquakes model best fits the data (minimum AICc and $\Delta_{\rm AICC} = 0$), though the four earthquake model is still statistically acceptable (second minimum AICc and $\Delta_{\rm AICC} = 6$). Both the 3 and the 4 earthquake scenario leave a large $\sim$5 m central section of the profile devoided of a clear discontinuity. The height of this section is much larger than that of the other sections, and is far greater than most normal earthquake displacements on such short 10-km-long faults. As such, it is likely that this section represents at least two, if not more, events. Interestingly, a minor peak at about 3.2–3.4 atom of ^{36}Cl per g of rock in Fig. 16(b) is consistent with an additional slip event in the central section of the profile. Thus, though our model does not resolve it, a scenario that includes five slip events may be equally reasonable. The five earthquake scenario also meets the conclusions previously reached by Palumbo *et al.* (2004).

The five earthquake ages we obtain are 7.2, 4.9, 4.0, 3.4 and 1.5 ka, respectively. Associated vertical displacements along scarp are 1.90, 2.05, 1.60, 3.60 and 2.00 m, respectively.

The displacement estimated for the oldest earthquake is a minimum value since the corresponding exposed section has not been sampled entirely. It could be as little as 1.25 m, assuming that the

Downloaded from https://academic.oup.com/gji/article-abstract/182/1/36/562733 by guest on 01 February 2019

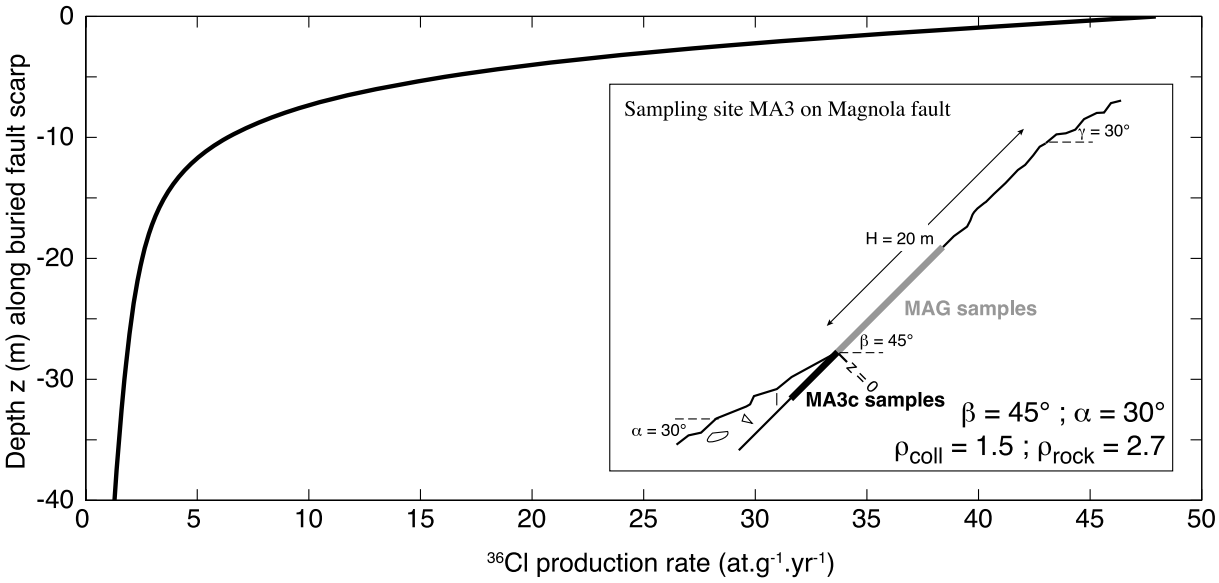

Figure 17. Production rate of ^{36}Cl (at g^{-1} yr^{-1}) along the Magnola buried fault plane as derived from the Magnola site parameters (neutrons and muons correction factors calculated for a constant geomagnetic field). As the colluvial wedge is thin, the depth (on fault scarp) of complete attenuation is deep, around 10–15 m.

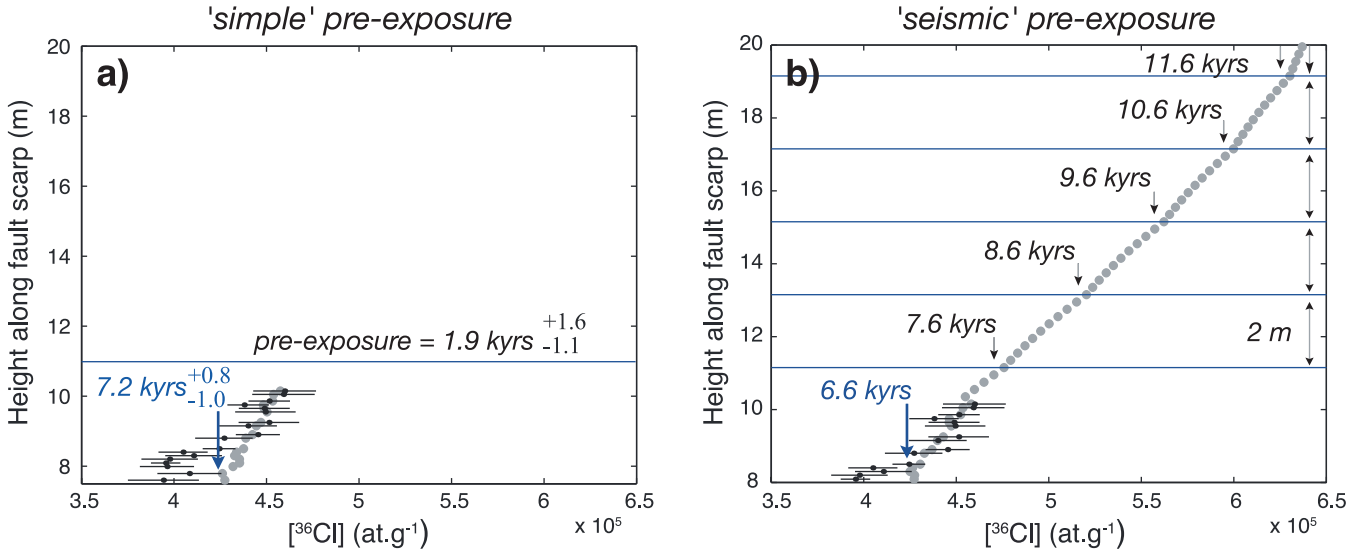

Figure 18. Modelling the uppermost Magnola data subset (from 8.9 to 10.15 m height along fault scarp). Black dots are data, with error bars indicating (2σ). Grey dots are modelled concentrations. (a) The simplest pre-exposure history is considered (no slip event). Dataset is well fitted for a pre-exposure duration of 1.9 kyr (+1.6/–1.1) and an age for the oldest recoverable earthquake of 7.2 ka (+0.8/–1.0). (b) A complex, multi-earthquake pre-exposure history is considered (five earthquakes, occurring every 1 kyr and each producing 2 m for example). Data are also well fitted for a pre-exposure duration of 5 kyr and an age for the oldest recoverable earthquake of 6.6 kyr. See details in text. Note that, below 9 m, the data are not properly fitted in either case. This shows that a second earthquake must be introduced to properly model the data.

displacement is entirely represented by the data. However, the effects of prior exposure favour a larger displacement that could be up to 2.35 m.

Quantifying uncertainties in the ages of the five earthquake scenarios

One can divide the factors contributing to the [^{36}Cl] in samples into two categories: those controlling the production rates and those controlling the duration of exposure. Uncertainties in both categories will translate into uncertainties in the final [^{36}Cl] in samples. A thorough examination of the influence of each factor on the final [^{36}Cl] would require a tremendous amount of computation time, even with the use of Monte Carlo methods. We have chosen to deal first with the factors controlling the duration of exposure, that is, the ages of the earthquakes and the pre-exposure, by keeping constant all other factors at the values given in Table 1. We have then tried to find the ages of earthquakes that fit best the fictitious data points obtained by subtracting/adding one standard deviation from the central [^{36}Cl] value (grey curves on Fig. 21). Combining these values with the preferred ages gives the following values: 7.2 (+0.8/–1.0), 4.9 (+0.2/–0.6), 4.0 (+0.3/–0.4), 3.4 (±0.3) and 1.5 (+0.3/–0.2) ka, respectively from the oldest to the youngest earthquake (Fig. 21).

Downloaded from https://academic.oup.com/gji/article-abstract/182/1/36/562733 by guest on 01 February 2019

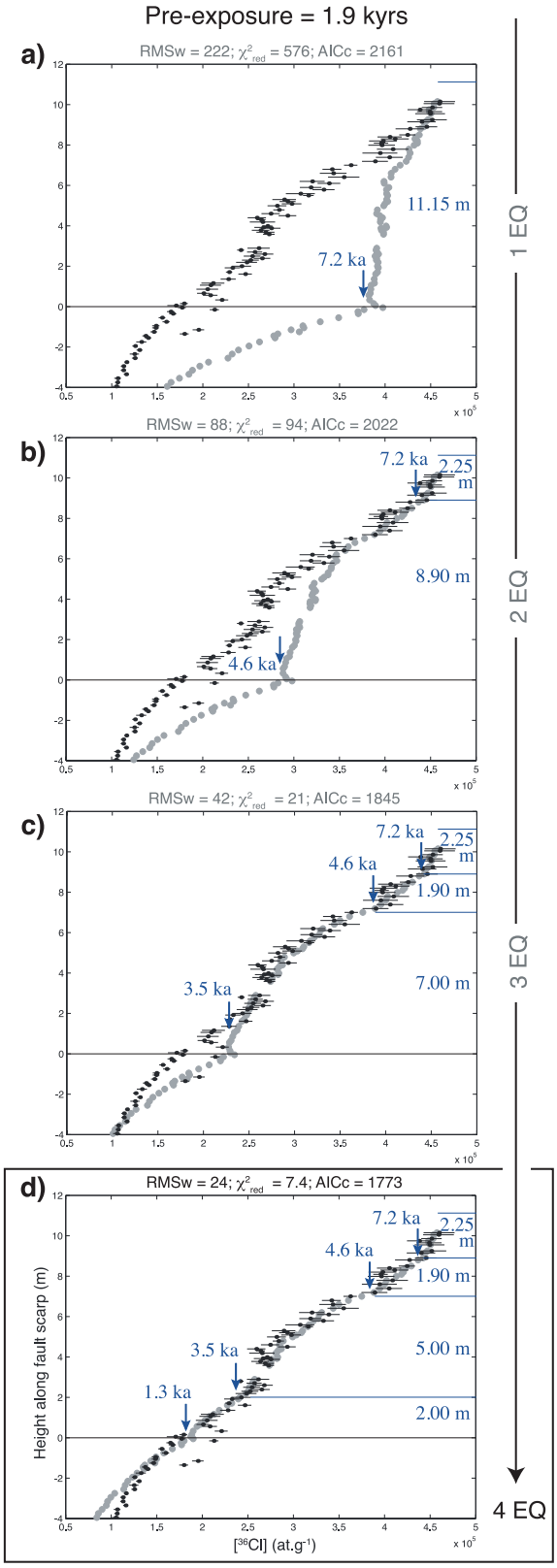

Figure 19. Fitting the entire Magnola data set by a four earthquake scenario. The simplest pre-exposure history has been arbitrarily chosen. A constant geomagnetic field is assumed (see text). The fit is performed in steps, each adding a new earthquake until the earthquake number derived from the discontinuity analysis is reached (Fig.16, and details in text). Fit indicators are provided, together with the age and displacement of each earthquake.

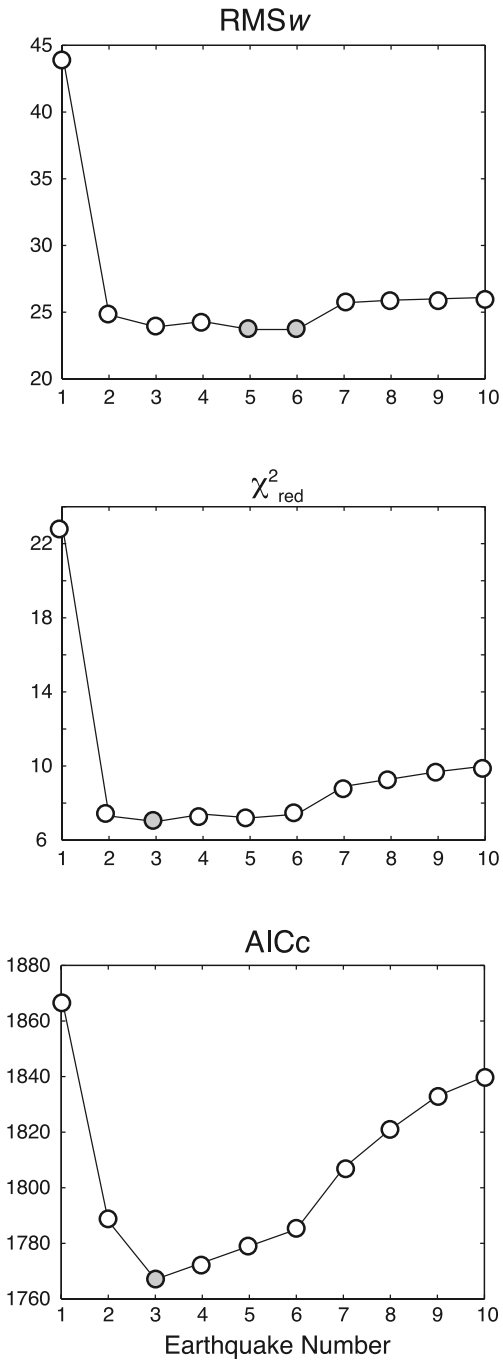

Figure 20. RMSw (weighted root mean square), χ^2_{red} (Chi-square), AICc (Akaike Information Criterion with a second order correction) values obtained from fitting the Magnola data with 1–10 earthquakes (see text for details on fit indicators). Best values are obtained for 3–6 earthquakes. See Fig. 21 and Electronic Supplement 8 for the corresponding models.

Then, we try to fit the central [^{36}Cl] values allowing factors controlling the production rates to vary around the value chosen in the first step. For [Ca] and [^{35}Cl], the intervals of variation are those of analytical measurements on ICP/MS and AMS, ±2 and ±5 per cent, respectively. For the factors describing the site position and geometry ($S_{el,s}$, $S_{el,\mu}$, α, β, ρ_{coll} and ρ_{rock}), the intervals of variation are given by uncertainties measured in the field (Table 1 and Fig. 22a). Finally, for spallation production rates at SLHL ($\Psi_{36CL\_Ca\_0}$) and attenuation lengths, intervals of variation

Downloaded from https://academic.oup.com/gji/article-abstract/182/1/36/562733 by guest on 01 February 2019

Table 5. AICc, ΔAICc, RMSw and χ^2_{red} values resulting from fitting the Magnola data with 1–10 earthquakes. In bold, the best-fitting values. Analysis of those fitting parameters is in Fig. 20.

Earthquake number	1	2	3	4	5	6	7	8	9	10
AICc	1869	1788	**1767**	1773	1779	1785	1807	1821	1833	1840
Δ*AICc*	102	21	0	6	12	18	40	54	66	73
RMSw	44.5	24.8	23.9	24.3	**23.7**	**23.7**	25.7	25.9	26	26.1
χ^2_{red}	23.1	7.3	**7**	7.4	7.2	7.4	8.9	9.3	9.7	10

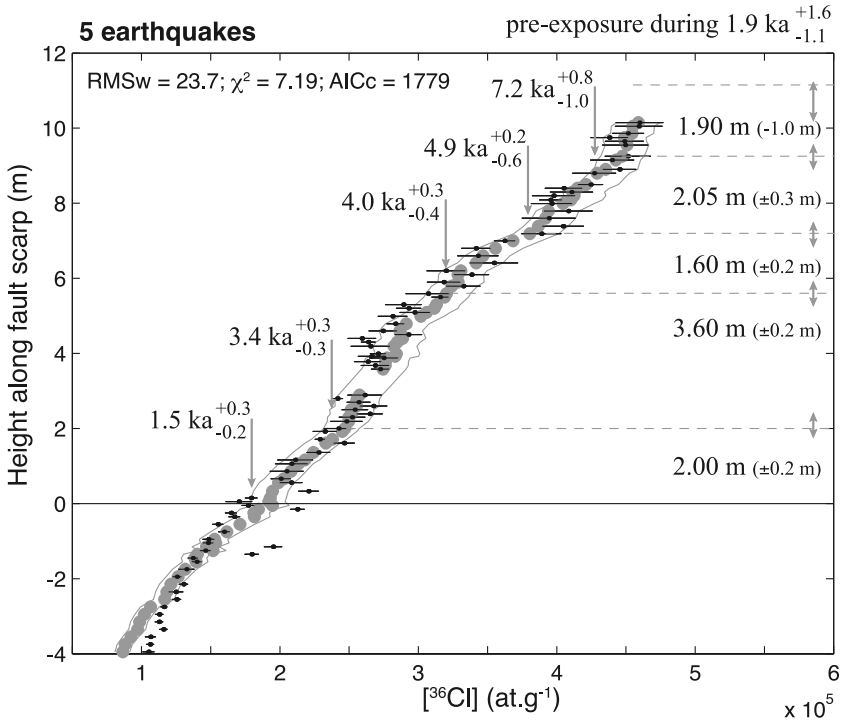

Figure 21. Best fit of the Magnola data set with five large slip exhumations. Model has been calculated with no denudation and for a constant geomagnetic field (see text for details). The data best fit is indicated by the grey dots, while fitting the data uncertainties produce the grey curves. Double arrows indicate uncertainties on the displacements. Earthquakes ages are indicated, together with their uncertainties.

are taken from the literature (Fig. 22a). In a first step, we have picked the [Ca] and [^{35}Cl] values that give the lowest/highest production rate, keeping all other factors constant at their best value. Fitting the central [^{36}Cl] value gives higher/lower bounds for the ages of the earthquakes (light green frame on Fig. 22b). In a second step, we allow site position and geometric factors to vary also, still keeping spallation production rates at SLHL and attenuation lengths constant. Again, picking the values that yield the lowest/highest production rates, the fit of [^{36}Cl] central values gives higher/lower bounds for the ages of the earthquakes (yellow frame on Fig. 22b). The same procedure is followed to add first spallation production rate uncertainty (orange frame on Fig. 22b) then attenuation length uncertainty (red frame on Fig. 22b). As uncertainties in the slow negative muon ($\Psi_{\mu,0}$) stopping rate are not clearly defined at present, we cannot include them, but introducing an arbitrary uncertainty of 5 per cent in this rate does not produce any significant age change.

When including possible uncertainties on all these factors, the ages of the five earthquakes become 7.2 (+1.1/–1.0), 4.9 (+1.4/–1.6), 4.0 (+1.2/–1.7), 3.4 (+1.0/–1.3) and 1.5 (+ 0.9/–1.0) ka, respectively (Fig. 22c).

As we have already shown that it has little effect on the total production rate at our site, we have not included the variability of the geomagnetic field over the time period analysed. Similarly, we have not included any denudation of the scarp, as we have already suggested that denudation is low at the Magnola site. Yet, including a denudation rate of 0.02 mm yr^{-1} (maximum bound) would lead to a further decrease in the final ^{36}Cl concentrations, in effect increasing the modelled earthquake ages as reported in Fig. 22(b) (on the right). In the extreme case in which the total production rate is the lowest due to the combination of all possible uncertainties and of denudation at 0.02 mm yr^{-1}, the earthquake ages would have uncertainties between ±0.8 and ±1.8 ka compared to the reference values (Fig. 22b).

The above analysis indicates that the ages and slips of the five large events identified from the Magnola scarp ^{36}Cl data are defined with a maximum uncertainty of ±1.8 kyr and ±0.5 m, respectively. Those two uncertainty values are maximum bounds. However, it is likely that actual uncertainties are lower, because denudation is negligible at the Magnola site and especially because the uncertainties estimated here result from adding the maximum uncertainties on all input parameters, which is probably an unlikely scenario. It is likely that the errors associated with the site geometry are the most significant. When only these errors are considered for all the earthquakes, the maximum uncertainties for the recovered ages and slips reduce to ±1.0 kyr and ±0.25 m, respectively. The ages obtained are 7.2 (+0.5/–0.5), 4.9 (+0.7/–0.9),

Downloaded from https://academic.oup.com/gji/article-abstract/182/1/36/562733 by guest on 01 February 2019

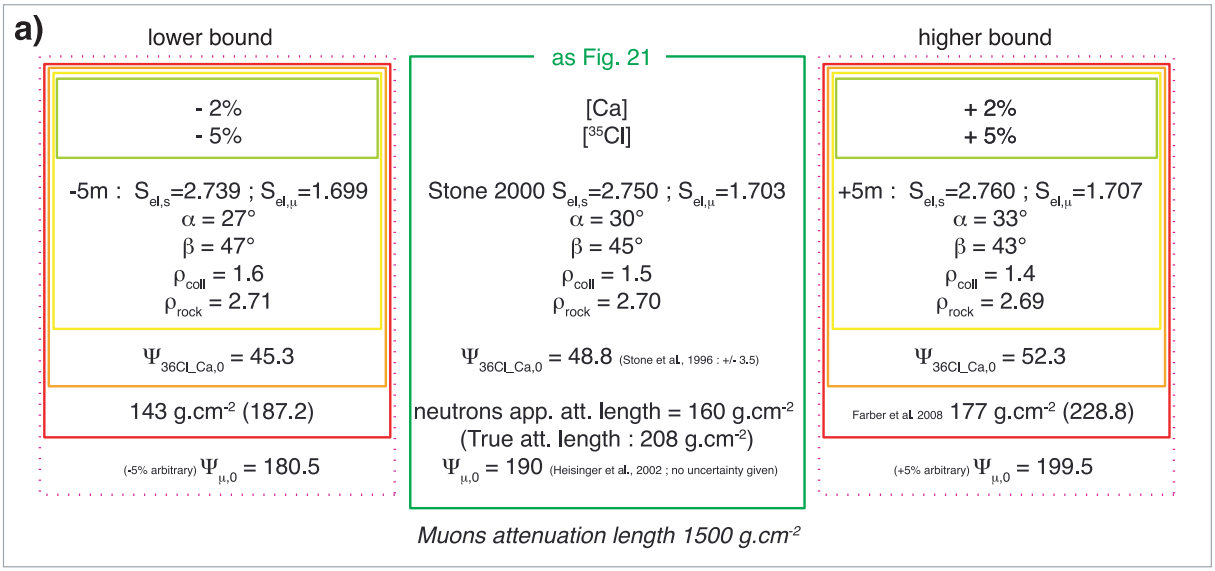

Earthquakes ages: **REF 5 EQ: 7.2 - 4.9 - 4.0 - 3.4 - 1.5 (ka)**

b)

	no denudation	denudation ε = 0.02 mm.yr^{-1}
higher bound	7.0 - 4.8 - 3.9 - 3.3 - 1.4 (ka)	
lower bound	7.4 - 5.0 - 4.1 - 3.5 - 1.6	8.4 - 5.4 - 4.3 - 3.5 - 1.5 ; pre-exp. 2.5 (ka)
higher bound	6.7 - 4.0 - 2.9 - 2.5 - 0.6	
lower bound	7.7 - 5.6 - 4.8 - 3.9 - 2.0	9.0 - 6.1 - 5.0 - 4.2 - 1.9 ; pre-exp. 2.5 (ka)
higher bound	6.2 - 3.8 - 2.7 - 2.3 - 0.5	
lower bound	8.3 - 5.9 - 4.9 - 4.2 - 2.2	9.7 - 6.3 - 5.3 - 4.3 - 2.1 ; pre-exp. 2.7 (ka)
higher bound	6.2 - 3.3 - 2.3 - 2.1 - 0.5	
lower bound	8.3 - 6.3 - 5.2 - 4.4 - 2.4 (*pre-exp. 1.9 ka*)	9.8 - 6.7 - 5.5 - 4.5 - 2.2 ; pre-exp. 3.3 (ka)

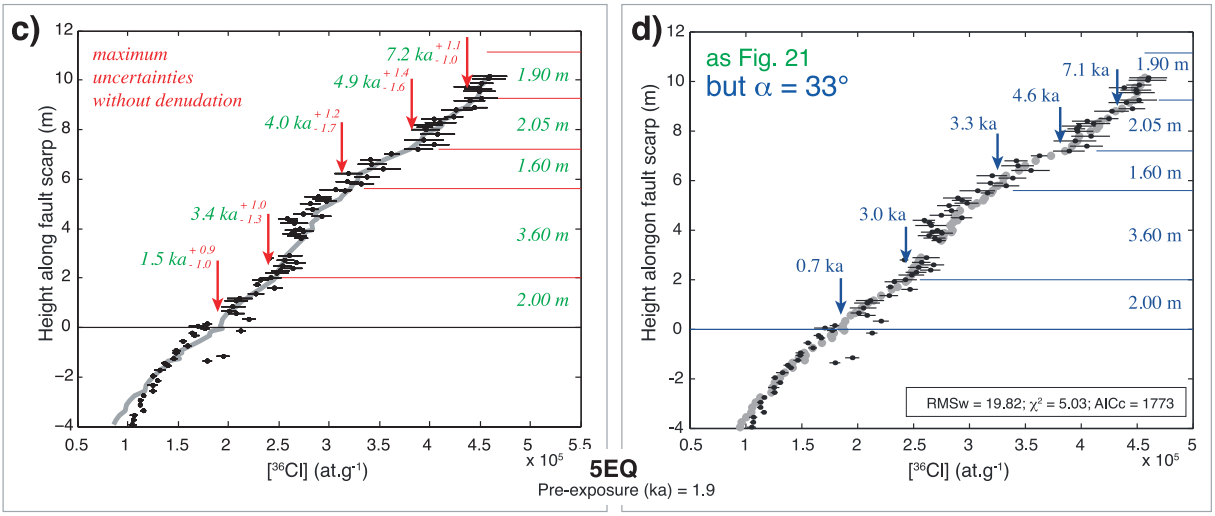

Figure 22. Quantifying the total uncertainties in the ages of the five major slip events. (a) The dark green box includes the mean values of all model input parameters. Those values serve to calculate the reference ages reported in dark green (b) (five earthquakes scenario, also Fig. 21). The pale green box takes into account the uncertainties in the parameters aligned with the indicated numbers and included into the box. The yellow box takes into account the uncertainties in the parameters aligned with the indicated numbers and included in the box. Same for orange and red boxes. This allows the number of parameters to be progressively increased and uncertainties included in the concentration calculations. (b) Lower and higher age values obtained for the five slip events, when the various sets of uncertainties are included in the calculations (same colours as in a). Ages are calculated both for no denudation and for denudation occurring at 0.02 mm yr^{-1}. (c) Data fit and ages obtained when integrating all parameters uncertainties (red box in a, and vertical line in b; no denudation). (d) Highlight of the particular case where data are fitted with $\alpha = 33°$; this emphasizes the strong effect of the colluvial wedge dip which, when taken equal to its highest value, leads to satisfactorily fit of concentrations in the buried part of the scarp.

Downloaded from https://academic.oup.com/gji/article-abstract/182/1/36/562733 by guest on 01 February 2019

4.0 (+0.8/–1.1) ka, 3.4 (+0.5/–0.9) and 1.5 (+0.5/–0.9) kyr (yellow, Fig. 22b).

We note that the fit is especially sensitive to the uncertainty on the α parameter (dip of the colluvium surface). When α is taken equal to its maximum possible value (33°), the buried samples are fitted adequately (Fig. 22d).

Finally, while the displacements produced by the five identified major slip events are generally similar to those found by P04 (P04 found 2.00, 2.00, 2.50, 2.70 and 1.80 m, with no uncertainties given), the ages of those events are significantly younger (P04 found 12.0, 10.5, 7.4, 6.7 and 4.8 kyr).

6 DISCUSSION

Our results indicate that many factors impact the final ^{36}Cl concentrations and cannot be neglected. The factors most affecting the ^{36}Cl concentrations are the scarp-rock chemical composition, the geographic location of the site, the shielding resulting from the specific geometry of the fault scarp and its associated colluvial wedge, and the denudation amount sustained by the scarp surface. The effects of the rock composition and of the site location are well known and have been included in previous models, while the geometrical shielding and denudation have either not been, or have only partially been integrated (Mitchell *et al.* 2001; Benedetti *et al.* 2002, 2003; Palumbo *et al.* 2004). These factors can have an important effect on the ^{36}Cl production rate—a 5° change in the dip of either the scarp or colluvial wedge can modify the ^{36}Cl production rate by 25 per cent in some of the samples. If both scarp and colluvial wedge geometry are varied, a 55 per cent uncertainty on the final ^{36}Cl concentrations of some of the samples results. This demonstrates the need to accurately define and integrate the geometry of the investigated fault site in the modelling of the ^{36}Cl concentrations. The denudation of the scarp surface also greatly affects the ^{36}Cl concentrations, resulting in uncertainties sometimes >10–15 per cent on the modelled [^{36}Cl] of the oldest exhumed part of the scarp. At our reference site (Table 1), the integration of the time variability of the geomagnetic field changes [^{36}Cl] by less than 8 per cent compared to the constant magnetic field hypothesis used in all prior calculations (Stone 2000). Finally, the chemical composition of the colluvial wedge and the possible snow shielding have only a minor effect on the predicted ^{36}Cl concentrations.

Many of those scaling factors may be well defined at a given site, substantially reducing uncertainties in the inferred rupture history. However, we generally have only limited and often qualitative information on denudation experienced by a scarp surface (Stone *et al.* 1998).

It is important to note that the ^{36}Cl production mechanisms and the 'elementary production rates' which we use in our calculations, based on the available literature (e.g. Stone *et al.* 1996, 1998, 2000; Gosse & Phillips 2001; Heisinger *et al.* 2002; Schimmelpfennig *et al.* 2009 and references therein), are still under refinement, so that absolute earthquakes ages may systematically change as well.

Our results indicate that the ^{36}Cl modelling allows recovery of the major features of an earthquake history, namely the most likely number of large slip events, the approximate ages of these major events, and the approximate total displacements produced by them. The uncertainties in those parameters, though significant, are smaller than might be expected given the large number of model parameters. Though it is impossible to derive any general conclusion from our site specific modelling, our work suggests that, in common cases, the number of major slip events can be defined with a ±1–2 uncertainty, the associated displacements with an uncertainty on the order of ±0.25 m for a given earthquake, while the corresponding ages have maximum uncertainties on the order of ±0.5–1.0 kyr. On the other hand, the modelling may not discriminate between a single large event and multiple small events tightly clustered in time. Therefore, $M_w \sim 6$ earthquakes producing at most tens of cm of vertical displacement at surface cannot be identified with ^{36}Cl modelling unless they are separated by a long period of inactivity, occur in areas where production rate is especially high, or at sites where the colluvial wedge is especially thick or has a high density. Because this resolution is controlled by ^{36}Cl production rate and cosmic ray attenuation length, it is unlikely that the ^{36}Cl dating approach will be suitable to identify small or frequent events even as knowledge about the scaling factors improves.

Our refined modelling of the Magnola data set (Central Apennines, Italy) requires that at least three, and more likely five large slip events have contributed to the total scarp exhumation (e.g. Palumbo *et al.* 2004). The ages estimated for those five slip events are 7.2 (+0.5/–0.5), 4.9 (+0.7/–0.9), 4.0 (+0.8/–1.1) ka, 3.4 (+0.5/–0.9) and 1.5 (+0.5/–0.9) kyr, with along-fault displacements of 1.90 (+0.5/–0.65), 2.05 (+0.0/–0.45), 1.60 (+0.0/–0.2), 3.60 (+0.0/–0.1) and 2.00 (+0.3/–0.0) m, respectively. Though the displacements are roughly similar to those previously found by P04 (2.00, 2.00, 2.50, 2.70, 1.80 m; uncertainties were not reported), rupture ages are markedly younger and recurrence times are generally shorter (2.3, 0.9, 0.6, 1.9, >1.5 kyr, instead of 1.5, 3.1, 0.7, 1.9, >4.8 kyr, respectively). The major reason for such differences is that our new modelling leads to an increase in the overall production rate at the Magnola site. This arises from the introduction of the actual steep slope of the colluvial wedge (30 ± 3°), from its appropriate density that was overestimated, and from the proper integration of all shielding effects, some of which were not considered by P04.

Based on our analysis, we can draw several inferences about the seismo-tectonics of the Magnola fault. First, as previously demonstrated by P04, [^{36}Cl] reveal the sporadic earthquake exhumation events along the Magnola scarp. Second, we find that at least three major slip events have occurred in succession over a short time span of ∼3 kyr (events 2, 3, 4). Whether each of those major slip events includes one large or several smaller earthquakes, this finding demonstrates that a number of $M > 6$ earthquakes have occurred in a temporal cluster between 5.6–2.5 ka. This earthquake cluster produced a total vertical slip of about 7 m. The earthquake cluster may have been preceded by a more quiescent period, as no large event seems to have occurred over the preceding 1–2 kyr. It is possible that the last, most recent slip event identified in the data is part of the earthquake cluster. If that is the case, the Magnola fault would still be in a phase of sustained activity, making it the source of an elevated seismic risk. The age of the youngest major earthquake is not clearly established however: while it is 1.5 + 0.5/–0.9 kyr when uncertainties on elementary production rates are ignored, it becomes 1.5 + 0.9/–1.0 kyr when all uncertainties are included. In a broad sense, three large historical earthquakes are known to have occurred in the Magnola region, over the last 2 kyr (1915 AD: e.g. Odonne 1915; Galadini & Galli 1999; Galli *et al.* 2008; 1349 AD: e.g. Pantosti *et al.* 1996; 508 AD: Galadini & Galli 1999). The 1915 earthquake corresponds to the rupture of the Fucino-basin normal faults (SE of Magnola fault). The 508 AD earthquake is also attributed to the rupture of the Fucino fault system from trench investigations. The 1349 AD earthquake could actually be the one identified as the last slip event on the Magnola scarp. The along-dip displacements estimated for the 5 identified major slip events range between 1.6 and 3.6 m (±0.5 m at the very most).

Downloaded from https://academic.oup.com/gji/article-abstract/182/1/36/562733 by guest on 01 February 2019

Though we cannot determine whether each slip event includes a single large earthquake or several smaller size earthquakes, we note that the recovered pluri-metric slip values are compatible with the slip expected to be produced at surface by the rupturing of a ∼10 km long, young, immature fault as is Magnola (Manighetti *et al.* 2007). Stress drops and near-field ground motions resulting from the Magnola earthquakes are thus expected to be large (Radiguet *et al.* 2009).

7 CONCLUSIONS

We developed a Matlab® code to model the [^{36}Cl] profiles measured in seismically exhumed limestone normal faults scarps. This model can determine the number, ages and along-fault displacements of the past major earthquakes that have ruptured these scarps. The model integrates the most recent knowledge on the ^{36}Cl production mechanisms and rates (Schimmelpfennig *et al.* 2009), and all the scaling factors that contribute to the ^{36}Cl production. Through a series of synthetic profiles, we have examined the effects of each scaling factor on the resulting concentration profiles, and quantified the uncertainties related to the variability of these factors. We have also examined how prior exposure and exposure history of the fault scarp control the resulting [^{36}Cl] profiles. Doing so has allowed us to estimate the uncertainties affecting the earthquake histories inferred through ^{36}Cl cosmogenic dating.

Our work highlights several key limitations that affect the resolution of the inferred recent rupture history along these types of faults, as follows.

(1) *Analytical limitations:* the uncertainties on $[^{36}Cl]_{AMS}$ range between 1 and 3 per cent. Thus we can conservatively estimate the uncertainty from the analytics to be no more than 5 per cent.

(2) *Production rate limitations:* although research programs are refining the ^{36}Cl production mechanisms and rates, currently ages cannot be determined with uncertainties lower than 0.2 kyr.

(3) *Site location and geometry limitations:* the modelling results are extremely site-dependent. Because production rate of ^{36}Cl decreases markedly with the site elevation, the recovery of slip events is more difficult at low elevation sites, requiring large slip events separated by long time spans. The production rate also decreases markedly with the site latitude, and so the same limitation is expected at low latitude sites. The time variability of the geomagnetic field varies non-linearly with the site longitude; the effect of that variability is expected to depend on the site longitude. Finally, the geometrical and cover shielding effects are entirely site-dependent. The thickness of the colluvial wedge has a particularly strong effect on the final concentration profile. As an example, a thick colluvial wedge shields footwall rocks, leading to well-defined segments in a [^{36}Cl] profile when the scarp face has finally been exhumed. This may allow the detection of moderate-slip earthquakes that would not have otherwise been detected.

(4) *Non-uniqueness of earthquake history:* in the best case where all site characteristics are accurately defined and integrated in the modelling, a number of different rupture history scenarios may similarly well explain the [^{36}Cl] measurements. This is mainly because, in most natural conditions expected for these faults, the ^{36}Cl production rates are quite low. The resulting variations in the ^{36}Cl concentrations are thus often subtle, making detection of small earthquakes or temporally clustered events difficult.

(5) *Limits on event detection:* inferred earthquake displacements must be viewed as the maximum slip produced by one or more earthquakes due to the fact that small, temporally clustered earthquakes may be impossible to discern from a single large event. The number of recovered earthquakes is thus always a minimum value, while the recovered displacements are maximum bounds. Displacement values have an uncertainty of the order of ±20 cm.

(6) *Detectable age for an event:* the inferred earthquake ages that are recovered represent the approximate times around which one large or several clustered smaller size earthquakes have occurred. Those times are recovered with uncertainties on the order of ±0.5–1.0 kyr.

(7) *Significance of the recovered slips:* earthquake displacements recovered through ^{36}Cl dating represent offset at a particular site and may thus differ from the maximum coseismic slip produced at the surface by the fault rupture (e.g. Manighetti *et al.* 2005). As only a fraction of the coseismic slip produced at depth by an earthquake commonly reaches the surface (e.g. Manighetti *et al.* 2007), they also provide only a minimum estimate of the slip experienced along the entire fault plane. In addition, the measured displacements may include some post-seismic slip, which can be as large as coseismic slip in some cases.

Despite of the limitations listed above, the ^{36}Cl dating method has the potential to recover robust information on the past earthquakes, which is critical to understanding fault behaviour and assess seismic hazard. First, [^{36}Cl] profiles can reveal if the fault scarp under study has been exhumed through the sporadic occurrence of large slip events or steady creep. The number of large slip events that have contributed to the exhumation of the scarp is also revealed with a small uncertainty, on the order of 1–2. The [^{36}Cl] modelling can often infer the time at which events may have ruptured the surface within 0.5–1.0 kyr, a resolution similar to that provided by other methods. These uncertainties generally decrease with the age of the recovered slip event, so that the last slip episode is generally resolved within 0.5 kyr. This is an important result as it is primarily the age of the last large earthquake that is needed in the seismic hazard assessment calculations. Finally, maximum slip values produced by the largest earthquakes or earthquakes clusters on the fault can be deduced using this approach. These maximum slip estimates are those needed in seismic hazard assessment, where they may serve as a basis to calculate maximum magnitude and ground motions expected from forthcoming ruptures along the fault.

In conclusion, the ^{36}Cl dating method is subject to important limitations. Nevertheless, it has the potential to provide important information on the past major earthquakes that have occurred on a limestone-offsetting normal fault. By properly integrating all the scaling factors that determine ^{36}Cl production rates we provide a reappraised modelling protocol that can be used to improve estimates (and their uncertainties) of past earthquake timing, recurrence and surface slip.

ACKNOWLEDGMENTS

This work has been funded by the INSU-CNRS Dyeti program and by the French ANR (project QUAKonSCARPS, no.

Downloaded from https://academic.oup.com/gji/article-abstract/182/1/36/562733 by guest on 01 February 2019

ANR-06-CATT-008–01 and ANR-06-CATT-008–03). We thank J. Malavieille for fruitful discussions and help on the field, and C. Benazet, P. Brenu, E. Canet, R. Grandin, R. Guiguet, S. Hok, H. Lankester, M. and J.M. Maurice, J.M. Nicole, F. Renalier, C. Romano, and B. Scalabrino, for helping us in the sampling, at the Magnola site and many others in the Lazio-Abruzzo region. L. Sevin, J. Marin and all the staff at SARM-CRPG (France) are acknowledged for the chemical measurements. We are very thankful to T. Guilderson and T. Brown as well as all the staff of the CAMS-LLNL (California) for their precious assistance and support for the ^{36}Cl measurements. All the people of the Forme village and specially A. Ercole are greatly acknowledged for their help and support. We also are very thankful to the regione Abruzzo and Lazio as well as the Corpo Forestale. We thank the Editor M. Cocco, G. Hilley and an anonymous reviewer for their thorough and constructive reviews that greatly improved the manuscript.

REFERENCES

Akaike, H., 1974. A new look at statistical model identification, *IEEE Trans. Automatic Contl.* **19**(6), 716–723.

Armijo, R. & Lyon-Caen, H. & Papanastassiou, D., 1992. East-west extension and Holocene normal-fault scarps in the Hellenic arc, *Geology,* **20,** 491–494.

Balco, G. & Stone, J.O., 2003. Measuring the density of rock, sand, till, etc, UW Cosmogenic Nuclide Laboratory, methods and procedures, http://depts.washington.edu/cosmolab/chem.html.

Benedetti, L., Finkel, R., Papanastassiou, D., King, G., Armijo, R., Ryerson, F., Farber, D. & Flerit, F., 2002. Post-glacial slip history of the Sparta fault (Greece) determined by 36Cl cosmogenic dating: evidence for non-periodic earthquakes, *Geophys. Res. Lett.,* **29**(8), 87_1–87_4.

Benedetti, L. *et al*., 2003. Motion of the Kaparelli fault (Greece) prior to the 1981 earthquake sequence determined from 36Cl cosmogenic dating, *Terra Nova,* **15**(2), 118–124.

Benson, L., Madole, R., Phillips, W., Landis, G., Thomas, T. & Kubik, P., 2004. The probable importance of snow and sediment shielding on cosmogenic ages of north-central Colorado Pinedale and pre-Pinedale moraines, *Quater. Sci. Rev.,* **23,** 193–206.

Burnham, K.P. & Anderson, D.R., 2002. *Model Selection and Multi-Model Inference: A practical Information-Theoretical Approach*. Springer Verlag, New-York.

Carcaillet, J., Manighetti, I., Chauvel, C., Schlagenhauf, A. & Nicole, J.-M., 2008. Identifying past earthquakes on an active normal fault (Magnola, Italy) from the chemical analysis of its exhumed carbonate fault plane, *Earth planet. Sci. Lett.,* **271**(1–4), 145–158.

Carignan, J., Hild, P., Mevelle, G., Morel, J. & Yeghicheyan, D., 2001. Routine Analyses of Trace Elements in Geological Samples using Flow Injection and Low Pressure On-Line Liquid Chromatography Coupled to ICP-MS: A Study of Geochemical Reference Materials BR, DR-N, UB-N, AN-G and GH, *Geostand. Geoanal. Res.,* **25**(2–3), 185–478.

Champion, D.E., 1980. Holocene geomagnetic secular variation in the western United States: implication for global geomagnetic field. Open-File Rep, *U.S. Geol. Surv.,* **314,** 80–824.

Cucchi, F., Forti, F. & Marinetti, E., 1995. Surface degradation of carbonate rocks in the Karst of Trieste (Classical Karst, Italy), in *Karren Landforms,* pp. 41–51, eds Formos, J.J. & Ginés, A., Palma.

Culler, T., Becker, T.A., Muller, R.A. & Rene, P.R., 2000. Lunar impact history from 40Ar/39Ar dating of glasse spherules, *Science,* **287,** 1785–1788.

Daëron, M., Klinger, Y., Tapponnier, P., Elias, A., Jacques, E. & Sursock, A., 2007. 12,000-Year_long record of 10 to 13 paleoearthquakes on the Yammoûneh fault, Levant fault system, Lebanon, *BSSA* **97**(3), 749–771.

Desilets, D. & Zreda, M., 2003. Spatial and temporal distribution of secondary cosmic-ray nucleon intensities and applications to in situ cosmogenic dating, *Earth planet. Sci. Lett.,* **206,** 21–42.

Desilets, D., Zreda, M., Almasi, P.F. & Elmore, D., 2006a. Determination of cosmogenic 36Cl in rocks by isotope dilution: innovations, validation and error propagation, *Chem. Geol.,* **233,** 185–195.

Desilets, D., Zreda, M. & Prabu, T., 2006b. Extended scaling factors for in situ cosmogenic nuclides: new measurements at low latitude, *Earth planet. Sci. Lett.,* **246,** 265–276.

Dunai, T.J., 2001. Influence of secular variation of the geomagnetic field on production rates of in situ produced cosmogenic isotopes, *Earth planet. Sci. Lett.,* **193,** 197–212.

Dunne, J., Elmore, D. & Muzikar, P., 1999. Scaling factors for the rates of production of cosmogenic nuclides for geometric shielding and attenuation at depth on sloped surfaces, *Geomorphology,* **27,** 3–11.

Elmore, D., Ma, X., Miller, T., Mueller, K., Perry, M., Rickey, F., Sharma, P. & Simms, P., 1997. Status and plans for the PRIME Lab AMS facility, *Nucl. Instruments Methods Phys. Res., Section B, Beam Interact. Mater. Atoms,* **123,** 69–72.

Elsasser, W., Ney, E.P. & Winckler, J.R., 1956. Cosmic-ray intensity and geomagnetism, *Nature,* **178,** 1226–1227.

Farber, D., Meriaux, A.-S. & Finkel, R., 2008. Attenuation length for fast nucleon production of ^{10}Be derived from near-surface production profiles, *Earth planet. Sci. Lett.,* **274,** 295–300.

Finkel, R.C. & Suter, M., 1993. AMS in the Earth Sciences: techniques and applications, *Adv. Anal. Geochem.,* **1,** 1–114.

Furlany, S., Cucchi, F., Forti, F. & Rossi, A., 2009. Comparison between coastal and inland Karst limestone lowering rates in the northeastern Adriatic Region (Italy and Croatia), *Geomorphology,* **104,** 73–81.

Galadini, F. & Galli, P., 1999. The Holocene paleoearthquakes on the 1915 Avezzano earthquake faults (central Italy): implications for active tectonics in the central Apennines, *Tectonophysics,* **308,** 143–170.

Galli, P., Galadini, F. & Pantosti, D., 2008. Twenty years of paleoseismology in Italy, *Earth-Sci. Rev.,* **88,** 89–117.

Gosse, J.C. & Phillips, F.M, 2001. Terrestrial in situ cosmogenic nuclides: theory and application, *Quater. Sci. Rev.,* **20,** 1475–1560.

Govindaraju, K., 1994. Compilation of working values and sample description for 383 geostandards, *Geostandards Newslett.,* **18,** 1–158.

Guyodo, Y. & Valet, J.P., 1999. Global changes in intensity of the Earth's magnetic field during the past 800 kyr, *Nature,* **399,** 249–252.

Heisinger, B., Lal, D., Jull, A.J.T., Kubik, P., Ivy-Ochs, S., Knie, K. & Nolte, E., 2002. Production of selected cosmogenic radionuclides by muons: 2. Capture of negative muons, *EPSL,* **200,** 357–369.

Hilley, G.E. & Young, J.J, 2008a. Deducing paleoearthquake timing and recurrence from paleoseismic data, Part I: Evaluation of new Bayesian Markov-Chain Monte Carlo simulation methods applied to excavations with continuous peat growth, *Bull. seism. Soc. Am.,* **98**(1), 383–406.

Hilley, G.E. & Young, J.J, 2008b. Deducing paleoearthquakes timing and recurrence from paleoseismic data. Part II: analysis of paleoseismic excavation data and earthquakes behavior along the Central and Southern San Andreas Fault, *Bull. seism. Soc. Am.,* **98**(1), 407–439.

Korte, M. & Constable, C.G., 2005a. Continuous geomagnetic field models for the past 7 millennia: 2. CALS7K, *Geochchem., Geophys., Geosyst.,* **6,** doi:10.1029/2004GC000801.

Korte, M. & Constable, C.G., 2005b. The geomagnetic dipole moment over the last 7000 years—new results form a global model, *Earth planet. Sci. Lett.,* **236,** 348–358.

Lifton, N.A., Bieber, J.W., Clem, J.M., Duldig, M.L., Evenson, P., Humble, J.E. & Pyle, R., 2005. Addressing solar modulation and long-term uncertainties in scaling secondary cosmic rays for in situ cosmogenic nuclide applications, *Earth planet. Sci. Lett.,* **239,** 140–161.

Lifton, N.A., Smart, D.F. & Shea, M.A., 2008. Scaling time-integrated in situ cosmogenic nuclide production rates using a continuous geomagnetic model, *Earth planet. Sci. Lett.,* **268,** 190–201.

Liu-Zheng, J., Klinger, Y., Xu, X., Lasserre, C., Chen, G., Chen, W., Tapponnier, P. & Zhang, B., 2007. Millennial recurrence of large earthquakes on the Haiyuan fault near Songshan, Gansu province, China, *BSSA,* **97**(1B), 14–34.

Lowell, T.V., 1995. The application of radiocarbon age estimates to the dating of glacial sequences: an example from the Miami sublobe, Ohio, USA, *Quater. Sci. Rev.,* **14,** 85–99.

Downloaded from https://academic.oup.com/gji/article-abstract/182/1/36/562733 by guest on 01 February 2019

Manighetti, I., Campillo, M., Sammis, C., Mai, P.M. & King, G., 2005. Evidence for self-similar, triangular slip distributions on earthquakes: Implications for earthquake and fault mechanics, *J. geophys. Res.,* **110,** B05302, doi:10.1029/2004JB003174.

Manighetti, I., Campillo, M., Bouley, S. & Cotton, F., 2007. Earthquake scaling, fault segmentation, and structural maturity, *Earth planet. Sci. Lett.,* **253,** 429–438.

McElhinny, M.W. & McFadden, P.L., 1997. Paleosecular variation over the past 5 Myr based on a new generalized database, *Geophys. J. Int.,* **131,** 240–252.

Merrill, R.T. & McElhinny, M.W., 1983. *The Earth's Magnetic Field: Its History, Origin and Planetary Perspective*. Academic Press, London, pp. 401.

Mitchell, S.G., Matmon, A., Bierman, P.R., Enzel, Y., Caffee, M. & Rizzo, D., 2001. Displacement history of a limtesone normal fault scarp, northern Israel, from cosmogenic 36Cl, *J. geophys. Res.,* **106**(B3), 4247–4264.

Odonne, E., 1915. Gli elementi fisici del grande terremoto marsicano-fucense del 13 gennaio 1915, *Boll. Soc. Sismol Ital.,* **19,** 71–216.

Ohno, M. & Hamano, Y., 1993. Global analysis of the geomagnetic field: time variation of the dipole moment and the geomagnetic pole in the Holocene, *J. Geomag. Geoelectr.,* **45,** 1455–1466.

Palumbo, L., Benedetti, L., Bourles, D., Cinque, A., Finkel, R., 2004. Slip history of the Magnola fault (Apennines, Central Italy) from 36Cl surface exposure dating: evidence for strong earthquake over the Holocene, *Earth planet. Sci. Lett.,* **225,** 163–176.

Pantosti, D., D'Adezzio, G. & Cinti, F.R., 1996. Paleoseismicity of the Ovindo-Pezza fault, central Apennines, Italy: a history including a large, previously unrecorded earthquake in the Middle Ages (860–1300 A.D.). *J. geophys. Res.,* **101**(B3), 5937–5959.

Piccardi, L., Gaudemer, Y., Tapponnier, P. & Boccaletti, M., 1999. Active oblique extension in the central Apennines (Italy): evidence from the Fucino region, *Geophys. J. Int.,* **139,** 499–530.

Pigati, S. & Lifton, N.A., 2004. Geomagnetic effects on time-integrated cosmogenic nuclide production with emphasis on in situ 14C and 10Be, *Earth planet. Sci. Lett.,* **226,** 193–205.

Radiguet, M., Cotton, F., Manighetti, I., Campillo, M. & Douglas, J., 2009. Dependency of near-field ground motions on the structural maturity of the ruptured faults, *Bull. seism. Soc. Am.,* **99**(4), doi: 10.1785/0120080340.

Schildgen, T.F., Phillips, W.M. & Purves, R.S., 2005. Simulation of snow shielding corrections for cosmogenic nuvlide surface exposure studies, *Geomorphology,* **64,** 67–85.

Schimmelpfennig, I., Benedetti, L., Finkel, R., Pik, R., Blard, P.-H., Bourlès, D., Burnard, P. & Williams, A., 2009. Sources of in-situ 36Cl in basaltic rocks, *implications for calibration of production rates, Quarter. Geochronol.*, submitted.

Sieh, K., Stuiver M. & Brillinger D., 1989. A more precise chronology of earthquakes produced by the San Andreas Fault in southern California, *J. geophys. Res.,* **94,** 603–623.

Sieh, K., Stuiver M. & Brillinger D., 1992. Implications of the precise chronology of earthquakes produced by the San Andreas Fault at Pallett Creek, Engineering Geology Practice in Southern California: Assoc. *Eng. Geol. Special Publ.,* **4,** 195–198.

Smith, D.I., Greenaway, M.A., Moses, C. & Spate, A.P., 1995. Limestone weathering in eastern Australia, Part 1: Erosion rates. *Earth Surf. Proc. Landforms,* **20,** 451–463.

Solanki, S.K., Usoskin, I.G., Kromer, B., Schussler, M. & Beer, J., 2004. Unusual activity of the Sun during recent decades compared to the previous 11,000 years, *Nature,* **431,** 1084–1087.

Stone, J.O., 2000. Air pressure and cosmogenic isotope production, *J. geophys. Res.,* **105**(B10), 23 753–23 759.

Stone, J.O., Allan, G.L., Fifield, L.K. & Cresswell, R.G., 1996. Cosmogenic chlorine-36 from calcium spallation, *Geochim. Cosmochim. Acta* **60**(4), 679–692.

Stone, J.O., Evans, J.M., Fifield, L.K., Allan, G.L. & Cresswell, R.G., 1998. Cosmogenic chlorine-36 production in calcite by muons, *Geochim. Cosmochim. Acta,* **62**(3), 433–454.

Weldon, R., Fumal, T. & Biasi, G., 2004. Wrightwood and the earthquake cycle: what a long recurrence record tells us about how faults work, *GSA Today,* **14**(9), 4–10.

Yang, S., Odah, H. & Shaw, J., 2000. Variations in the geomagnetic dipole moment over the last 12 000 years. *Geophys. J. Int.,* **140,** 158–162.

Zreda, M. & Noller, J.S., 1998. Ages of prehistoric earthquakes revealed by cosmogenic Chlorine-36 in a Bedrock fault scarp at Hebgen Lake, *Science,* **282,** 1097–1099.

APPENDIX A: TOPOGRAPHIC SHIELDING OF NORMAL FAULT SITES

Equations below are only valid for calculation of the fast neutron flux which is not energy dependent.

The cosmic ray flux intensity arriving from the sky in the direction given by the inclination θ (positive upwards) and the azimuth ϕ is generally given by

$$I(\theta, \phi) = I_0 \sin^m \theta \tag{A1}$$

for $\theta > 0$ and $I(\theta, \phi) = 0$ for $\theta < 0$. I_0 is the maximum intensity and m is an empirical constant, generally taken to be equal to 2.3 (e.g. Lal 1958; Nishiizumi *et al*. 1989). If the sample exposed is not shielded, it will receive the maximum possible flux given by

$$\Phi_{\max} = \int_0^{2\pi} \int_0^{\pi/2} I_0 \sin^m \theta \cos\theta \, \mathrm{d}\theta \, \mathrm{d}\phi = \frac{2\pi I_0}{m+1}. \tag{A2}$$

In the presence of a shielding topography, the cosmic ray flux $\mathbf{\Phi}$ will be reduced by a shielding factor $S = \mathbf{\Phi}/\mathbf{\Phi}_{\max}$. If the topography is described by a relationship between its vertical angle $\boldsymbol{\theta}_{\text{topo}}$ (as seen from the sampling site) and the azimuth ϕ, the remaining flux will be

$$\Phi = \int_0^{2\pi} \int_{\theta_{\text{topo}}}^{\pi/2} I_0 \sin^m \theta \cos\theta \, \mathrm{d}\theta \, \mathrm{d}\phi \tag{A3}$$

and the shielding factor S is given by

$$S = \frac{m+1}{2\pi} \int_0^{2\pi} \int_{\theta_{\text{topo}}(\phi)}^{\pi/2} \sin^m \theta \cos\theta \, \mathrm{d}\theta \, \mathrm{d}\phi. \tag{A4}$$

Eq. (A4) can lead to a closed form in the rare cases where the $\theta_{\text{topo}}(\phi)$ relationship is simple. Otherwise, is has to be numerically integrated.

A1 A simple dipping fault plane

Generally, the fault scarp can be modelled in a first approximation as a semi-infinite plane of dip β. If the azimuth ϕ is taken to be 0 (or π) in the fault direction and $\pi/2$ in the direction of maximum scarp slope, the relationship between θ_{topo} and ϕ is given by

$$\theta_{\text{topo}}(\phi) = \operatorname{atan}(\tan\beta \sin\phi), \quad 0 \le \phi \le \pi \tag{A5a}$$

$$\theta_{\text{topo}}(\phi) = 0, \quad \pi \le \phi \le 2\pi. \tag{A5b}$$

Eq. (A5a) is simply the expression of the apparent slope of the scarp in the azimuth ϕ. The resulting shielding factor $S(\beta)$ is given by

$$S(\beta) = \frac{1}{2} + \frac{m+1}{2\pi} \int_0^{\pi} \int_{\operatorname{atan}(\tan\beta \sin\phi)}^{\pi/2} \sin^m \theta \cos\theta \, \mathrm{d}\theta \, \mathrm{d}\phi. \tag{A6}$$

If there is a significant topography across the valley, its shielding effect must be included here, in the $\pi \le \phi \le 2\pi$ domain, by replacing the 1/2 term by an expression similar to eq. (A4) but for $\pi \le \phi \le 2\pi$.

Downloaded from https://academic.oup.com/gji/article-abstract/182/1/36/562733 by guest on 01 February 2019

A2 Colluvial wedge

As the samples have been buried beneath a colluvial wedge before being exhumed by an earthquake, it is necessary to take into account the partial shielding created by this wedge. As for the fault scarp, we assume that it can be modelled by a semi-infinite plane of dip α. At any point beneath the colluvial wedge, the cosmic ray flux intensity coming from the direction (θ, ϕ) will be attenuated from its surface value by a factor $\exp(-d/\lambda)$ where d is the distance travelled throuth the colluvium by the incoming particle and A the true attenuation length of the corresponding particle flux. In the case of fast neutrons, $l \approx 208$ g cm^{-1} (e.g. Gosse & Phillips 2001).

If the target is at a distance Z (positive downwards) beneath the colluvium-fault intersection (Fig. 4 in the main text), the distance d travelled through the colluvium by a particle coming from the direction (θ, ϕ) is given by

$$d_- = \frac{Z \sin(\beta - \alpha)}{\sin\theta \cos\alpha - \cos\theta \sin\alpha \sin\phi} \quad \text{if } 0 \le \phi \le \pi \tag{A7a}$$

$$d_+ = \frac{Z \sin(\beta - \alpha)}{\sin\theta \cos\alpha + \cos\theta \sin\alpha \sin\phi} \quad \text{if } 0 \le \phi \le 2\pi. \tag{A7b}$$

Our expression of d differs from that given by Dunne *et al*. (1999, eq. 12) as we use a different depth Z. Combining the shielding provided by the fault scarp of slope β and the attenuation due to the colluvial wedge of slope α, the resulting flux at Z is

$$\Phi(Z, \alpha, \beta) = \int_0^{\pi} \int_{\text{atan}(\tan\beta \sin\phi)}^{\pi/2} I_0 \mathrm{e}^{-d_-/\lambda} \sin^m\theta \cos\theta \, \mathrm{d}\theta \, \mathrm{d}\phi + \int_0^{\pi} \int_{\text{atan}(\tan\beta \sin\phi)}^{\pi/2} I_0 \mathrm{e}^{-d_+/\lambda} \sin^m\theta \cos\theta \, \mathrm{d}\theta \, \mathrm{d}\phi. \tag{A8}$$

In the actual calculation, the distances d_-, d_+, and the attenuation length λ have to be expressed in the same units, for example, cm or g cm^{-2}. The ratio between Φ and $\Phi_{\max}$ can then be used as a scaling factor $S_d(Z, \alpha, \beta)$ for the production rate (Dunne *et al*. 1999) beneath the colluvial wedge. The Matlab® program (see Supplement 1) *scdepth.m* computes $S_d(Z, \alpha, \beta)$.

Plotting S as a function of Z for given values of α and β shows (Figs A2.a, b and c) that it is reasonable to approximate the scaling factor by an exponential decay of the form

$$S_d(Z, \alpha, \beta) \approx S_Z \exp(-Z/\Lambda_Z), \tag{A9}$$

where A_Z is an apparent attenuation length. In order to facilitate the comparison with the work of Dunne *et al*. (1999), we calculate the scaling factor as a function of z, the distance measured perpendicularly to the colluvial upper surface, which is related to Z by $z = Z \sin(\beta - \alpha)$. The scaling factor can also be approximated by an exponential decay in z of the form $S_d(z) = S_z \exp(-z/\Lambda_z)$ where Λ_z is the apparent attenuation length relevant to the z direction, perpendicular to the colluvial outer surface. In the case of a flat colluvium and no scarp, $\alpha = \beta = 0$, we find that setting the true attenuation length $\lambda = 208$ g cm^{-2} gives $\Lambda_z \approx 157$ g cm^{-2}, which is close to the classical value of 160 g cm^{-2} used in vertical profiles (e.g. Gosse & Phillips 2001). Other calculated values of $s_{o,f}$ and Λ_f are given in Figs A2(c) and (d) for given α and β related to Figs 5(a) and (b) of the main text.

A3 Change in dip of the fault escarpment

It has been observed that, above the steep scarplet, the mountain front has a gentler slope. Samples located near the top of the scarplet will receive not only particles from the atmosphere directly above them but also particles who will have travelled through the upper surface (Fig. A1). Again, if we take the scarp and the mountain front above as planar surfaces of slopes β and γ, respectively, the particle flux arriving at the sample from the direction (θ, ϕ) will be attenuated by a factor $\exp(-d/\lambda)$ where d is the distance travelled through the footwall rock from the entry point to the sample and λ is the true attenuation length. If the scarp height is H and the position of the sample on the scarp surface is measured by Z (positive upwards), then d is given by

$$d = \frac{(H - Z)\sin(\beta - \gamma)}{\sin\theta \cos\gamma - \cos\theta \sin\gamma \sin\phi}, \tag{A10}$$

The net contribution of these particles to the flux reaching the sample will then be

$$\Phi = \int_0^{\pi} \int_0^{\text{atan}(\tan\beta \sin\phi)} I_0 \mathrm{e}^{-d/\lambda} \sin^m\theta \cos\theta \, \mathrm{d}\theta \, \mathrm{d}\phi. \tag{A11}$$

In fact, the lower limit of the inner integral may not be 0 but $\text{atan}(\tan\gamma \sin\phi)$, the apparent slope of the upper surface in the direction ϕ, as the distance d becomes infinite for $\theta \le \text{atan}(\tan\gamma \sin\phi)$ and attenuation is complete.

The total flux received by the sample can then be calculated and leads to the following scaling factor $S_s(Z, H, \beta, \gamma)$

$$S_s(Z, H, \beta, \gamma) = \frac{1}{2} + \frac{m+1}{2\pi} \int_0^{\pi} \int_{\text{atan}(\tan\beta \sin\phi)}^{\pi/2} \sin^m\theta \cos\theta \, \mathrm{d}\theta \, \mathrm{d}\phi + \frac{m+1}{2\pi} \int_0^{\pi} \int_{\text{atan}(\tan\gamma \sin\phi)}^{\text{atan}(\tan\beta \sin\phi)} \mathrm{e}^{-d/\lambda} \sin^m\theta \cos\theta \, \mathrm{d}\theta \, \mathrm{d}\phi. \tag{A12}$$

The Matlab® program (see Supplement 1) *scsurf.m* computes $S_s(Z, H, \beta, \gamma)$. This time, the scaling factor $S_s(Z, H, \beta, \gamma)$ should be modelled, for given values of H, β and γ, as the sum of a constant term and of an exponential, reflecting the contributions of particles reaching directly the sample and particles having travelled through the upper surface of the fault scarp, respectively.

If the scarplet height H is small enough, it may become necessary to combine the effects of the colluvial wedge and of the upper surface to calculate the scaling factor for samples located at relatively shallow depths beneath the colluvial wedge (in fact, the Matlab® program *scdepth.m* mentioned above includes the presence of an upper slope).

A4 In the presence of erosion

In the presence of erosion, a sample now at the surface will have been partially shielded from the surface flux by a layer of rock of decreasing thickness. It is therefore necessary to calculate the flux reaching a sample beneath the scarp surface. Assuming for the moment that the scarp surface is an infinite plane of slope β, if e is the rock thickness between the (future) sample and the scarp surface (Fig. A3a), the distance travelled by a particle coming from the direction (θ, ϕ) is

$$d_- = \frac{e}{\sin\theta \cos\beta - \cos\theta \sin\beta \sin\phi} \quad \text{if } 0 \le \phi \le \pi \tag{A13a}$$

$$d_+ = \frac{e}{\sin\theta \cos\beta + \cos\theta \sin\beta \sin\phi} \quad \text{if } 0 \le \phi \le 2\pi. \tag{A13b}$$

Downloaded from https://academic.oup.com/gji/article-abstract/182/1/36/562733 by guest on 01 February 2019

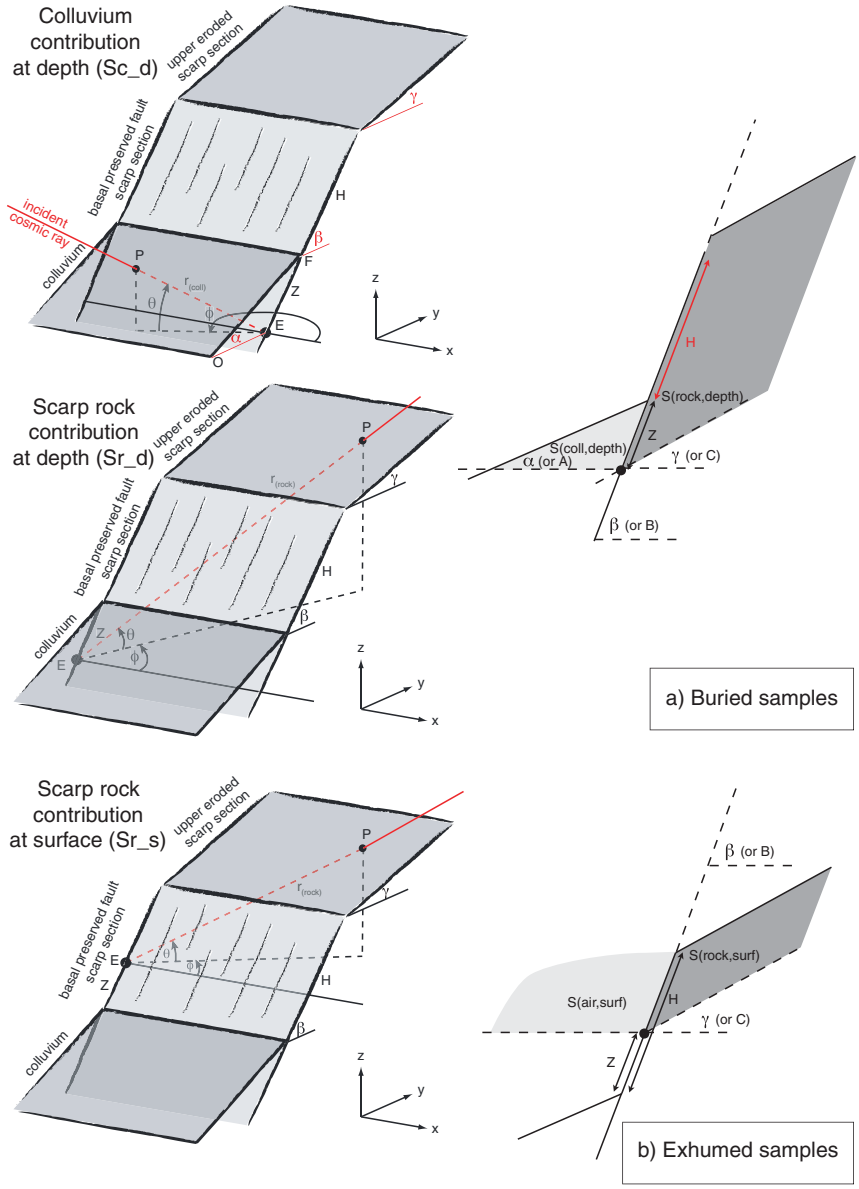

Figure A1. Schematic representation of the geometry of a normal fault scarp and associated colluvial wedge, and resulting shielding. α is colluvial wedge dip, β the basal scarplet dip, and γ the dip of the upper part of the fault escarpment. H is the actual height of the basal scarplet. When γ and β are different, (a) buried samples receive cosmic rays passing through the colluvium ('colluvium contribution' of the flux), and cosmic rays passing through the scarp rock ('rock contribution' of the flux), (b) the exhumed samples receive cosmic rays travelling through the air, plus cosmic rays passing through the rock.

The corresponding scaling factor is

$$S_r(e,\beta) = \frac{m+1}{2\pi}\int_0^{\pi}\int_{\mathrm{atan}(\tan\beta\sin\phi)}^{\pi/2} \mathrm{e}^{-d_-/\lambda}\sin^m\theta\cos\theta\,\mathrm{d}\theta\,\mathrm{d}\phi + \frac{m+1}{2\pi}\int_0^{2\pi}\int_0^{\pi/2}\mathrm{e}^{-d_+/\lambda}\sin^m\theta\cos\theta\,\mathrm{d}\theta\,\mathrm{d}\phi. \quad \text{(A14)}$$

The Matlab® program (see Supplement 1) *scrock.m* computes $S_r(e,\beta)$. For a given scarp slope β, the scaling factor $S_r(e)$ is also well approximated by an exponential decay of the form

$$S_r(e,\beta) \approx S_e\exp(-e/\Lambda_e). \quad \text{(A15)}$$

A5 Colluvium + upper surface + erosion

If we wish to model the erosion of a scarp of slope β and height H, above a colluvial wedge of slope a and below an upper surface of slope γ, the same methodology as in the above cases should be used: (1) calculating first the distance d between the entry point at the Earth's surface and the target at depth as a function of the incoming direction (θ,ϕ) and (2) integrating the attenuated flux intensity over the ($0 \le \phi \le 2\pi$, $0 \le \theta \le \pi/2$) domain, skipping regions from which no flux is coming by adjusting the integration limits for θ as we did above.

It is easy to see that the expression of d as a function of the target position given by Z and e (Fig. A3a) becomes very

Downloaded from https://academic.oup.com/gji/article-abstract/182/1/36/562733 by guest on 01 February 2019

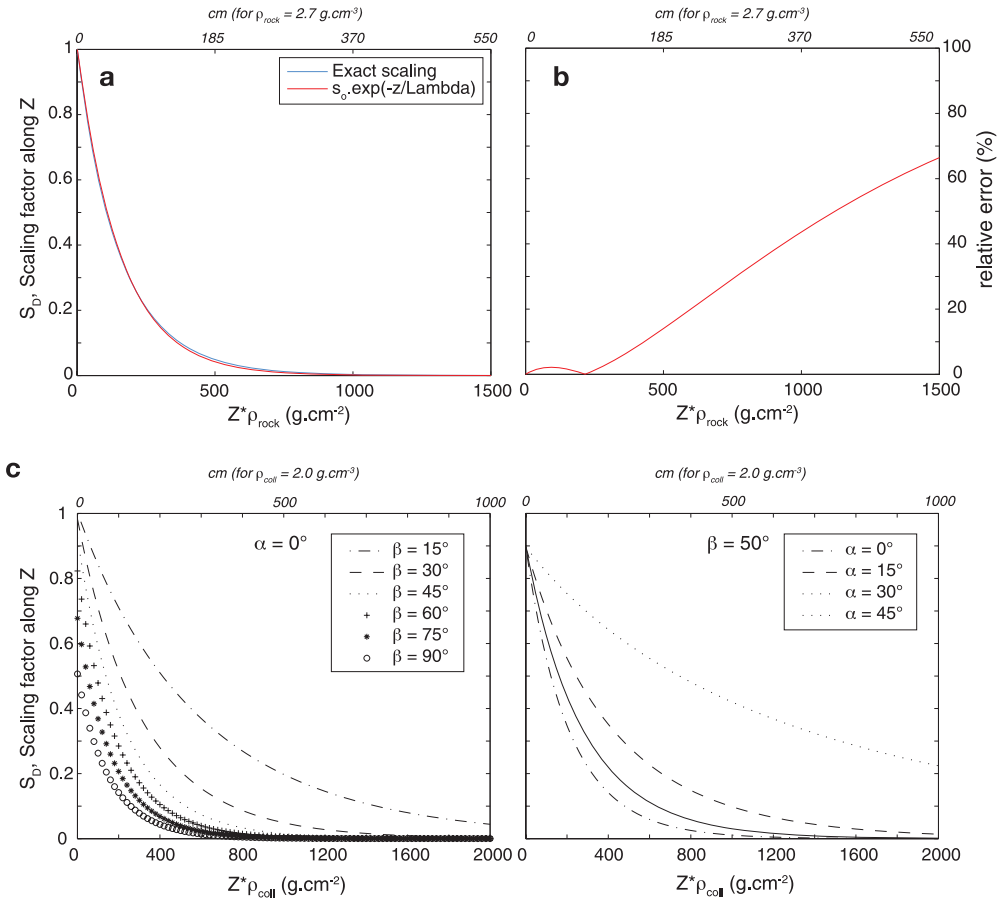

d

1) variations of β (α = 0°):

β	15°	30°	45°	60°	75°	90°
so_*f*_depth	0.9876	0.9679	0.9120	0.8114	0.6680	0.5015
Λ_*f*_depth	157.35	159.70	162.80	164.80	163.65	157.65

2) variations of α (β = 50°):

α	0°	15°	30°	45°
so_*f*_depth	0.8836	0.8836	0.8836	0.8836
Λ_*f*_depth	163.70	162.70	149.25	116.70

for ρ_rock = 2.7 and ρ_coll = 2.0 (g.cm-3)

Figure A2. Fast neutron attenuation at depth. (a) Comparison of exact scaling and its fit by an exponential with the *fitexp.m* Matlab® code ($S = s_0 \cdot \exp(-Z/\Lambda_f)$). Corresponding values of z in cm at the top are given for $\rho_{\text{rock}} = 2.7$. (b) Relative error between the two previous curves. (c) Scaling with depth for different values of β and α and (d) corresponding values of s_0 and Λ_f.

complex as several regions have to be considered and that the integration of the flux intensity becomes cumbersome, if not painful. It will be very difficult to easily express the corresponding scaling factor $S_t(Z, e)$ as a function of Z and e. As, however, this scaling factor should vary smoothly with Z and e, we believe that it is reasonable to assume that S_t can be expressed as the product of two scaling factors, one accounting for the shape of the scarp itself and being a function of Z, and one accounting for the thickness e of footwall rock separating the target form the scarp surface

$$S_t(Z, e) = f(Z)g(e). \tag{A16}$$

At the surface of the scarp ($e = 0$), $S_t(Z, 0)$ should be equal to the scaling factors S_d or S_s we have calculated above in eqs (A9) and (A12). Above the colluvial wedge and far enough from the top of the scarp surface, $S_t(Z, e)$ should be equal to $S_r(e)$. The solution is to take

$$S(Z, e) = S_r(e)\bar{S}(Z), \tag{A17}$$

where $S(Z)$ is either $S_d(Z)$ or $S_S(Z)$, depending on the location of the target, normalized to the (identical) value they take at the colluvium-fault scarp limit (Fig. A3a). This ensures that the effect of the scarp slope β is not taken into account twice. With this normalization, $S(Z)$ decrease exponentially from 1 towards 0 for increasing depths

Downloaded from https://academic.oup.com/gji/article-abstract/182/1/36/562733 by guest on 01 February 2019

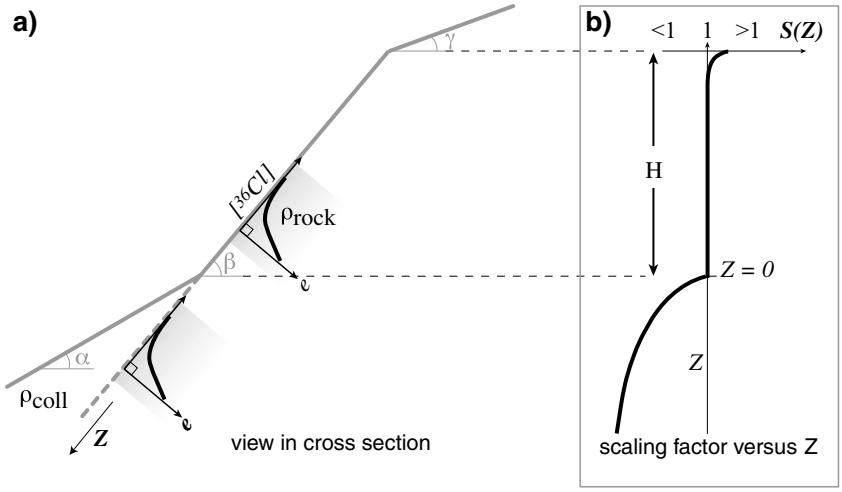

Figure A3. The attenuations along '*e*' and '*Z*' directions are separated: (a) the [Cl] profile due to rock attenuation is calculated for a surface of dip β in the direction e perpendicular, (b) a scaling factor $S(Z)$, which is only applied to the cosmogenic part of the production, is introduced. It accounts for both attenuation at depth ($S(Z) < 1$) and increased flux at the vicinity of γ ($S(Z)$). It is calculated by scaling the cosmogenic production at surface far from γ (at $Z = 0$, for β infinite).

beneath the colluvium, while it increases slightly towards the top of the scarp, reflecting the increasing contribution of particles entering through the upper surface (Fig. A3b).

APPENDIX B: Matlab® CODE DESCRIPTION

B1 The production rate *P*

Production rates are calculated using the full description of the production sources from Schimmelpfennig *et al*. (2009; after Gosse & Phillips, 2001). Both *clrock.m* and *clcoll.m* have equivalent equations. They differ only by the fact that *clcoll.m* also takes into account the colluvial wedge mean chemical composition: it calculates the production rate in the sample (scarp rock composition) buried under a thickness z of colluvium having its proper chemical composition.

Thickness factors (Q_x; with x standing for each production source) from Gosse & Phillips (2001) are only valid for samples at the surface vicinity. We recalculated the thickness factors to express them as a function of depth. The new thickness factors are defined at the sample centre, or thickness half, named th_2 (in 'e' direction) and are the following (using Schimmelpfennig *et al*. 2009, nomenclature):

For spallation:

$$Q_{sp} = 1 + \frac{1}{6}\left(\frac{th_2}{\Lambda_{f,e}}\right)^2. \tag{B1}$$

For direct capture of slow negative muons:

$$Q_{\mu} = 1 + \frac{1}{6}\left(\frac{th_2}{\Lambda_{\mu}}\right)^2. \tag{B2}$$

For epithermal neutrons:

$$\begin{aligned} Q_{\mathrm{eth}} &= \frac{1}{P_{\mathrm{eth}}}\left[\phi^*_{\mathrm{eth}}\left(\frac{f_{\mathrm{eth}}}{\lambda_{\mathrm{eth}}}\right)(1-p(E_{th}))\exp\left(\frac{-e}{\Lambda_{f,e}}\right)\left(1+\frac{1}{6}\left(\frac{th^2}{\Lambda_{f,e}}\right)^2\right)\right. \\ &+(1+R_{\mu}R_{\mathrm{eth}})(F\Delta\phi)^*_{eth}\left(\frac{f_{\mathrm{eth}}}{\Lambda_{\mathrm{eth}}}\right)(1-p(E_{th}))\exp\left(\frac{-e}{L_{\mathrm{eth}}}\right) \\ &\times\left(1+\frac{1}{6}\left(\frac{th_2}{L_{\mathrm{eth}}}\right)^2\right) \\ &\left.+R_{\mu}\phi^*_{\mathrm{eth}}\left(\frac{f_{\mathrm{eth}}}{\Lambda_{\mathrm{eth}}}\right)(1-p(E_{th}))\exp\left(\frac{-e}{\Lambda_{\mu}}\right)\left(1+\frac{1}{6}\left(\frac{th_2}{\Lambda_{\mu}}\right)^2\right)\right]. \end{aligned} \tag{B3}$$

For thermal neutrons:

$$\begin{aligned} Q_{th} = \frac{1}{P_{th}}&\left[\phi^*_{th}\left(\frac{f_{th}}{\Lambda_{th}}\right)\exp\left(\frac{-e}{\Lambda_{f,e}}\right)\left(1+\frac{1}{6}\left(\frac{th_2}{\Lambda_{f,e}}\right)^2\right)\right. \\ &(1+R'_{\mu})(\Im\Delta\phi)^*_{th}\left(\frac{f_{th}}{\Lambda_{th}}\right)\exp\left(\frac{-e}{L_{eth}}\right)\left(1+\frac{1}{6}\left(\frac{th_2}{L_{\mathrm{eth}}}\right)^2\right) \\ &(1+R'_{\mu}R_{th})(\Im\Delta\phi)^*_{th}\left(\frac{f_{th}}{\Lambda_{th}}\right)\exp\left(\frac{-e}{L_{th}}\right)\left(1+\frac{1}{6}\left(\frac{th_2}{L_{th}}\right)^2\right) \\ &\left.R'_{\mu}\phi^*_{th}\left(\frac{f_{th}}{\Lambda_{th}}\right)\exp\left(\frac{-e}{\Lambda_{\mu}}\right)\left(1+\frac{1}{6}\left(\frac{th_2}{\Lambda_{\mu}}\right)^2\right)\right]. \end{aligned} \tag{B4}$$

Apparent attenuation length for fast neutrons is calculated as explained above in part 1 of the Appendix using either *scdepth.m, scsurf.m,* or *scrock.m* depending of sample position in Z direction (Fig. 5 of the main text). As slow muons flux is energy dependent (e.g. Gosse & Phillips 2001) the same calculation of the apparent attenuation length of slow muons cannot be achieved as for fast neutron. We use the 1500 g cm^{-2} defined for a flat surface (e.g. Gosse & Phillips 2001, p. 1504).

Downloaded from https://academic.oup.com/gji/article-abstract/182/1/36/562733 by guest on 01 February 2019

B2 The number of atoms N

The equation governing the evolution of the number N of ^{36}Cl atoms is

$$\frac{dN}{dt} = -\lambda_{36}N + P, \tag{B5}$$

where λ_{36} is the decay constant of ^{36}Cl and P is the production rate. In certain conditions, eq. (B5) can be solved analytically. Here we want to model the evolution of a fault scarp whose geometry changes repeatedly with time, we wish also to study the influence of a variable magnetic field on the production rate, and to account for possible erosion of the scarp surface. This has lead us to solve eq. (B5) numerically by dividing the time span of the scarp evolution into small increments of time and writing

$$N(t + \Delta t) = N(t) + [P(t) - \lambda_{36}N(t)] \times \Delta t. \tag{B6}$$

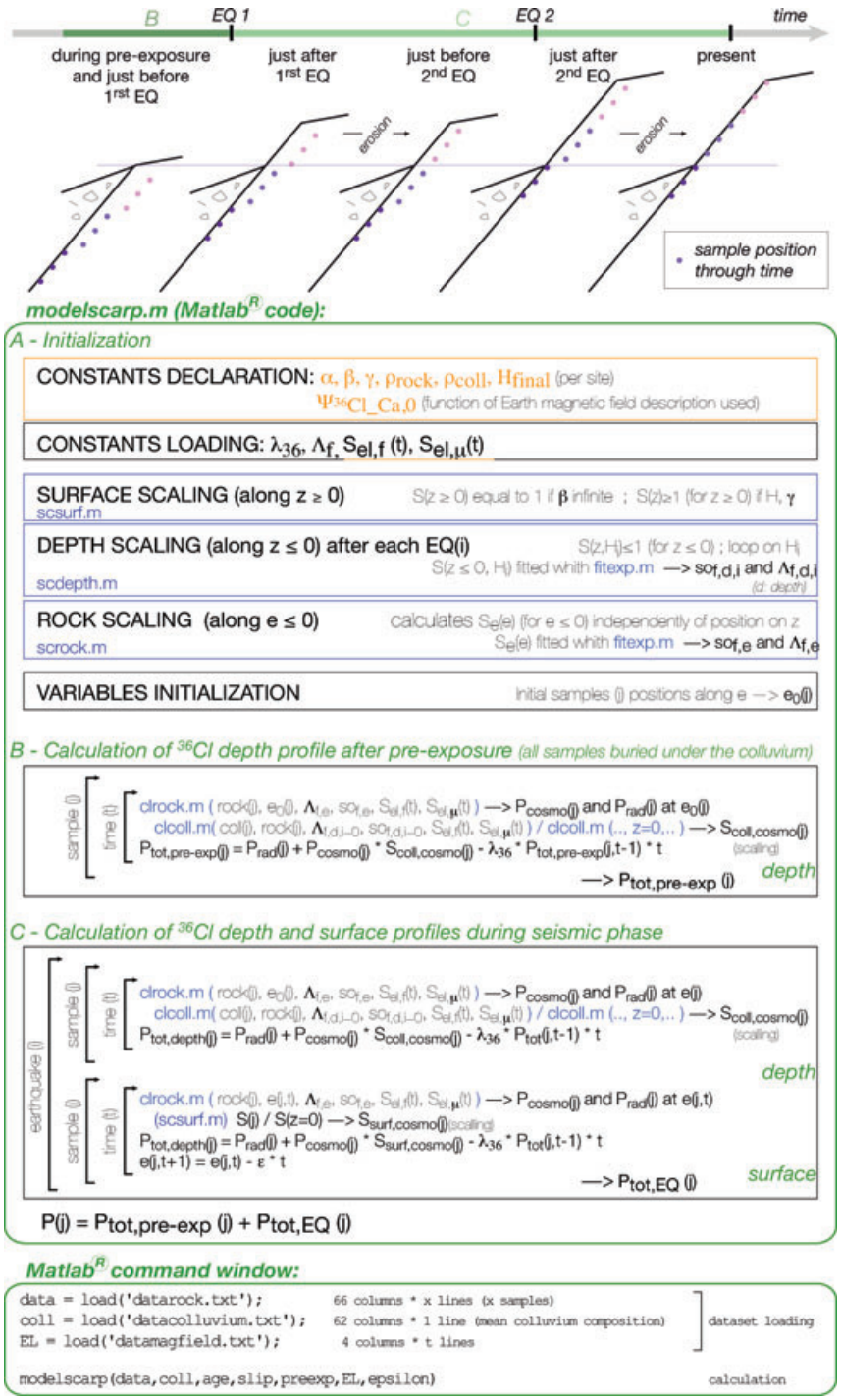

Figure B1. Schematic representation of the Matlab® *modelscarp.m* program given in Supplement 1. In orange, parameters that need to be modified for each site by the users. *EQ* stands for Earthquake; *f* for neutrons; μ, for muons; *j* for the sample; *i* for the earthquake number; *t* for the time step; *rock* for the sample chemical composition; *coll* for the mean colluvial wedge composition; P_{cosmo} for the cosmogenic production; P_{rad} for the radiogenic production; *epsilon* for the erosion rate (in mm yr^{-1}).

© 2010 The Authors, *GJI*, **182,** 36–72
Journal compilation © 2010 RAS

Downloaded from https://academic.oup.com/gji/article-abstract/182/1/36/562733 by guest on 01 February 2019

These time increments are small enough, typically 100 yr, to ensure that the magnetic field and hence its effects on the production rate through the elevation-latitude correcting factors $S_{el,f}$ for fast neutrons and $S_{el,\mu}$ for muons, can be considered constant. In that, we follow the method used for instance by Dunai (2001), Pigati & Lifton (2004), Lifton *et al*. (2005) and Lifton *et al*. (2008). The changes in geometry, either by earthquake slip or erosion are accounted for by calculating the scaling factor $S(Z(t), e(t))$. For instance, if the erosion rate is ε, the thickness e of rock between the sample and the scarp surface varies as

$$e(t + \Delta t) = e(t) - \varepsilon \times \Delta t. \quad \text{(B7)}$$

Changes in Z occur every time there is an earthquake, so that $Z(t)$ values are updated much less frequently than e(t) values. Finally, each segment of the fault scarp has its own exhumation history. This has lead us to write a Matlab® program, named *modelscarp.m* (see Supplement 1 and Fig. B1), whose main structure is based on the nesting of three loops: one for each of the segments, one for the number of earthquakes prior to the exhumation of the current segment (once it is exhumed, the actual Z values of a segment have no influence the production rate), and one for the small time increments Δt. Before these loops, the program calculates the number of ^{36}Cl atoms at the end of the pre-exposition time.

SUPPORTING INFORMATION

Additional Supporting Information may be found in the online version of this article:

Supplement S1. *modelscarp* folder (Matlab® code) for earthquake recovering using *in situ* ^{36}Cl on limestone active normal fault scarp.
Supplement S2. Sample chemical preparation for Cl extraction in limestone rocks (modified after Stone *et al.* 1996).
Supplement S3. Equations for [Cl] and [^{36}Cl] concentrations calculations, from AMS ratios.
Supplement S4. Scaling factors for fast neutrons ($S_{el,s}$) and slow muons($S_{el,\mu}$) according to different Earth palaeomagnetic models
Supplement S5. Replicates values from Magnola MA3c data set (samples below the colluvium).
Supplement S6. Chemical composition of five samples from the colluvial wedge at MA3 site (Magnola Fault) and corresponding mean compositions.
Supplement S7. MA3 data set (Magnola fault) modelled by one event or creep.
Supplement S8. Best fit of the Magnola data set from MA3 site by 3, 4 and 6 large slip exhumations.

Please note: Wiley-Blackwell are not responsible for the content or functionality of any supporting materials supplied by the authors. Any queries (other than missing material) should be directed to the corresponding author for the article.

Downloaded from https://academic.oup.com/gji/article-abstract/182/1/36/562733 by guest on 01 February 2019